

# **Reliability Evaluation of a 1.85 mm Blind Mating Coaxial Interconnect for mmWave ATE Applications**

**António José Rodrigues Mendes**

Thesis to obtain the Master of Science Degree in

## **Materials Engineering**

Supervisors: Prof. Augusto Manuel Moura Moita de Deus  
Eng. José António Alves Moreira

### **Examination Committee**

Chairperson: Prof. Maria Emília da Encarnação Rosa  
Supervisor: Prof. Augusto Manuel Moura Moita de Deus  
Member of the Committee: Prof. Paulo Jorge Matos Fernandes Martins Ferreira

**January 2020**



Dedicated to my family

*"...winning is one thing. But out of losing, I always learned more for the future. I got stronger from losing."*

Niki Lauda



## Acknowledgments

First of all, I want to thank my supervisors José Moreira and Augusto Moita de Deus who guided me for the last months. Their time and effort was fundamental to overcome the difficulties faced during this project and they also contributed for my development as a person and professional.

To Instituto Superior Técnico, which was my "home job" during the last 5 years, I am grateful for all the knowledge transmitted. In this university I understood the true meaning of excellency and sacrifice.

To Advantest Europe, for providing me the opportunity of doing an internship, I want to extend my gratitude to the research and development team who were always willing to help and share their knowledge. Special thanks to Marc Mössinger, who manages the team where I developed this thesis work and was always willing to help me with the faced difficulties, and for providing me suggestions along this project.

To Signal Microwave, a critical partner to this process, I am especially grateful to Bill Rosas and Eric Gebhard for all the help and expertise shared along the latest months which were extremely important to develop a more extended plan.

To University of Stuttgart, I am thankful to Professor Simon Sven and Peter Gaenz for providing me the Computed Tomography equipment, which was an important tool to turn this project more complete.

In terms of software, I am grateful to Comsol for their support that helped me in the simulations chapter and to Mathworks for their support in some difficulties I had with my Matlab code development.

To my materials engineering colleagues, I am pleasant for the journey we shared during the last 5 years. Especially to Gabriel Gira and Francisco Antão, I am grateful for all the companionship we created that was fundamental to overcome all the difficulties during projects, tests and exams.

To all my friends who supported me emotionally a big thank you.

Thanks to Cláudia Narciso for providing me such an amazing experience in Germany, which turned me into a totally different person.

Last but not least, I am grateful to my family (Joaquim, Fernanda and Ana) who for the last years were always with me in the choices I had made. Thanks for supporting me in the good and bad moments and for always believing in me. Without their support I could not have gone so far.



## Resumo

Nos últimos anos, a transmissão de grandes quantidades de dados usando Circuitos Integrados (CI) é um desafio das áreas de telecomunicação e redes. O surgimento da tecnologia 5G e dos dispositivos Wireless Gigabit (WiGig) requerem uma banda de frequência entre 24 e 70 GHz, com possíveis aumentos no futuro. O teste do CI é realizado por Equipamento de Teste Automático (ETA). A conexão num ETA, entre o Dispositivo Sobre Test (DST) e a Placa de Circuito Impresso (PCI), é estabelecida por um conector coaxial de 1.85 mm. Consequentemente, este projeto concentra-se na fiabilidade desse conector.

A avaliação de cada conector foi baseada em medidas elétricas, mecânicas e dimensionais ao longo de um teste cíclico (60,000 ciclos) realizado num sistema ETA. Para além disso, baseado numa Análise de Modo e Efeito de Falha (AMEF), técnicas como o Microscópio Eletrónico de Varrimento (MEV) e a Tomografia Computadorizada (TC) foram utilizadas. Uma simulação mecânica entre o contato do pin e do socket foi realizada segundo o Método dos Elementos Finitos (MEF).

De um total de 14 conectores testados, 10 para medir os S-parameters, 2 para medir a resistência de contato e 2 para medir os S-parameters após um teste acelerado (ACT), 11 falharam. A falha ocorreu no conector fêmea, especificamente na reentrância (keyhole) do socket. A fadiga é o mecanismo de falha responsável pela fissuração. No geral, o conector apresentou elevada fiabilidade (cerca de 40,000 ciclos) em aplicações usando ETA.

**Palavras-chave:** 5G, teste de CI, ETA, conector coaxial 1.85 mm, fiabilidade, MEF, ACT





## Abstract

Over the past years, the transmission of extensive volumes of data in Integrated Circuits (ICs) have been a challenge of telecommunication and networking areas. The emergence of 5G and the wireless gigabit (WiGig) technology, require an operating frequency range between 24 and 70GHz with further increase in the future. IC testing is performed by Automatic Test Equipment (ATE) integrated in a semiconductor test cell. The interconnection in an ATE, between the Device Under Test (DUT) and the Printed Circuit Board (PCB) test fixture, is established by a custom designed 1.85 mm blind mating coaxial connector. Therefore, this work focus on the reliability evaluation of this connector.

The connectors evaluation was based in several electrical, mechanical and dimensional measurements along a cyclic testing (60,000 cycles) performed in an ATE system. Moreover, a failure mode and effects analysis (FMEA) was achieved by using techniques such as the Scanning Electron Microscope (SEM) and Computed Tomography (CT). Furthermore, a mechanical simulation between of pin and socket contact during docking, was conducted based on the Finite Element Method (FEM).

From a total of 14 tested connectors: 10 to measure S-parameters, 2 to measure contact resistance and other 2 to measure S-parameters after an accelerated test (ACT), 11 have failed. The failure occurred at the female pair, specifically at the socket keyhole. Fatigue is the failure mechanism responsible for the cracking. Overall, the 1.85 mm blind mating coaxial connector presented a high reliability (over 40,000 cycles) for ATE applications.

**Keywords:** 5G, IC testing, ATE, 1.85 blind mating coaxial connector, reliability evaluation, FEM, ACT



# Contents

- Acknowledgments . . . . . v
- Resumo . . . . . vii
- Abstract . . . . . ix
- List of Tables . . . . . xiii
- List of Figures . . . . . xv
- Nomenclature . . . . . xix
- Glossary . . . . . xxi
  
- 1 Introduction . . . . . 1**
- 1.1 Motivation . . . . . 1
- 1.2 Automatic Test Equipment (ATE) . . . . . 3
- 1.3 Objectives . . . . . 5
- 1.4 Thesis Outline . . . . . 6
  
- 2 Background . . . . . 7**
- 2.1 Standards . . . . . 7
  - 2.1.1 IEEE 287 Standard . . . . . 7
  - 2.1.2 IPC-9592 Standard . . . . . 8
  - 2.1.3 MIL Standards . . . . . 8
- 2.2 Coaxial Connectors . . . . . 9
  - 2.2.1 Materials . . . . . 10
  - 2.2.2 Specifications and Parameters . . . . . 10
  - 2.2.3 Testing and Evaluation . . . . . 11
  - 2.2.4 Types of Coaxial Connectors . . . . . 12
  - 2.2.5 Blind Mating 1.85 mm Coaxial Connector . . . . . 13
- 2.3 Reliability Engineering . . . . . 16
  - 2.3.1 Statistical Mathematical Methods . . . . . 17
  - 2.3.2 Physics of Failure . . . . . 21
  - 2.3.3 Reliability of Coaxial Connectors . . . . . 23
  
- 3 Testing setup . . . . . 25**
- 3.1 Testing Conditions . . . . . 25

3.2	Setup Implementation . . . . .	31
<b>4</b>	<b>Testing Results</b>	<b>35</b>
4.1	Electrical Measurements . . . . .	35
4.1.1	Scattering Parameters (S-parameters) . . . . .	35
4.1.2	Contact Resistance . . . . .	40
4.2	Mechanical and Dimensional Measurements . . . . .	42
4.2.1	Withdrawal and Insertion Forces . . . . .	42
4.2.2	Concentricity . . . . .	45
4.2.3	Pin Depth . . . . .	47
4.3	Application of Reliability Models . . . . .	48
<b>5</b>	<b>Characterization</b>	<b>53</b>
5.1	Computed Tomography . . . . .	53
5.2	Scanning Electron Microscope . . . . .	58
<b>6</b>	<b>Modelling</b>	<b>63</b>
6.1	Geometry and Global Definitions . . . . .	63
6.2	Simulation Results . . . . .	66
6.3	Simulation and measurements correlation . . . . .	70
<b>7</b>	<b>Conclusions</b>	<b>73</b>
7.1	Achievements . . . . .	74
7.2	Future Work . . . . .	74
	<b>Bibliography</b>	<b>77</b>
<b>A</b>	<b>IEEE 287 Standard 1.85 mm Connector Drawings</b>	<b>83</b>
<b>B</b>	<b>Connector Photos</b>	<b>84</b>
<b>C</b>	<b>Mechanical and Dimensional Measurements</b>	<b>88</b>
<b>D</b>	<b>Measured S-Parameters</b>	<b>91</b>
<b>E</b>	<b>Simulation Results</b>	<b>99</b>
<b>F</b>	<b>Characterization - Scanning Electron Microscope</b>	<b>100</b>

# List of Tables

2.1	Electrical, mechanical and environmental specifications for a 1.85 mm coaxial connector.	8
2.2	Examples of different connectors used from low RF to mmwave frequencies. . . . .	12
2.3	Target specifications and materials for the Blind Mating 1.85 mm Connector. . . . .	14
2.4	Expressions that characterize the Weibull distribution. . . . .	18
2.5	Expressions that characterize the lognormal distribution. . . . .	20
2.6	Expressions that characterize the exponential distribution. . . . .	20
4.1	Cycles to failure for the different connectors tested along the reliability stress testing. . . .	48
4.2	Connectors considered for the reliability models and the correspondent expressions used for the different distributions. . . . .	49
4.3	Comparison of different reliability percentage, failure rates and MTTF for the different distributions. . . . .	52
5.1	Measurements of gold and nickel thickness for pin and inner surface of the socket. . . . .	59
6.1	Comparison between simulation and experimental results. . . . .	71
D.1	Summary of Connector Reliability testing results. . . . .	98



# List of Figures

1.1	Example of an ATE test cell for DDR testing composed of an ATE system and a robotic handler that inserts the packaged integrated circuits into the ATE system (256 units in parallel).	2
1.2	Advantest V93000 ATE system with a DUT test fixture IC socket based testing application.	3
1.3	Picture of the interconnect interface of an Advantest V93000 ATE system.	4
1.4	Top and bottom part of a DUT wafer probing test fixture.	4
1.5	Top and bottom part of a DUT package testing test fixture.	5
2.1	S-parameters explanation and respective equations.	12
2.2	Different Types of Coaxial Connectors.	13
2.3	3D models of the custom blind mating 1.85 mm coaxial connector designed for the Advantest V93000 ATE system.	15
2.4	Manufactured Blind Mating 1.85 mm coaxial connector with its components.	15
2.5	Bathtub failure rate curve with different reliability regimes.	17
2.6	Generic S-N curve showing the different stages for a logarithmic scale.	22
3.1	Hysteresis curve of spring compression test (top curve represents the compression and bottom curve the uncompression).	25
3.2	Differences of wear in the interior of female connector for different waiting times.	26
3.3	Diagram of temperature and humidity obtained from the ClimeEvent.	27
3.4	Diagram showing the integration of the 1.85mm blind mating interconnect into the brackets that are assembled in the DUT test fixture stiffener and ATE system.	27
3.5	Resultant plots of forces obtained by a Chatillon Force Gauge for a new connector.	28
3.6	Demonstration on how concentricity is calculated.	28
3.7	Pin depth distance according to the IEEE P287 standard.	29
3.8	High-level block diagram of the reliability test plan for the 14 connectors.	30
3.9	Automatized setup used to test the blind mating 1.85 mm connectors.	32
3.10	Force measurement setup to obtain the withdrawal and insertion forces.	32
3.11	Insertion and withdrawal pins pictures and drawings.	33
3.12	Summary of the used equipment.	34
4.1	S12 measured for connector 5 in intervals of 300 cycles until 60,000 cycles	36

4.2	Variation of S12 for connector 5 measured every 300 cycles until 60,000 cycles. . . . .	36
4.3	Different perspectives of the crack in connector pair 13. . . . .	37
4.4	Variation of S12 for connector 12 measured every 300 cycles until 60,000 cycles. . . . .	37
4.5	3D plot that demonstrate the variation of S12 for the different number of cycles. . . . .	38
4.6	Measured S12 performance of connector 8. . . . .	39
4.7	Measured S12 performance of connector 11. . . . .	40
4.8	Contact resistance versus number of cycles for connector 13. . . . .	41
4.9	Contact resistance versus number of cycles for connector 14. . . . .	41
4.10	Withdrawal forces of connectors 5, 12 and 13, at different number of cycles. . . . .	43
4.11	Insertion forces of connector 5, 12 and 13 at different number of cycles. . . . .	43
4.12	Insertion force plot of connector 12 before the first docking cycle. . . . .	44
4.13	Insertion force plot of connector 12 after 24,000 cycles. . . . .	45
4.14	Interior picture of the connector pairs at different number of cycles. . . . .	46
4.15	Concentricity of the pin as a function of the number of cycles for connector 5, 12 and 13. . . . .	46
4.16	Concentricity of the socket as a function of the number of cycles for connector 5, 12 and 13. . . . .	47
4.17	Pin depth for connector 5, 12 and 13. . . . .	47
4.18	Resultant plot obtained from the linearization using the Weibull distribution. . . . .	49
4.19	Reliability as a function of the number of cycles for a blind mating coaxial connector using the Weibull distribution. . . . .	50
4.20	Resultant plot obtained from the linearization using the lognormal distribution. . . . .	50
4.21	Reliability as a function of the number of cycles for a blind mating coaxial connector using the lognormal distribution. . . . .	50
4.22	Resultant plot obtained from the linearization using the exponential distribution. . . . .	51
4.23	Reliability as a function of the number of cycles (until cycle 100,000) for a blind mating coaxial connector using the exponential distribution. . . . .	51
5.1	CT industrial measurement setup. . . . .	53
5.2	CT scans performed for the connector pairs 12. . . . .	54
5.3	CT scan of the socket and pin of connector 12 after 30,000 cycles. . . . .	55
5.4	Centre contact retention deviation and temperature impact on the connector bead (pro- vided by connector designer). . . . .	55
5.5	CT scans at different cycles of the female connector 13. . . . .	56
5.6	CT scan of the socket and pin for connector 13 after 60,000 cycles. . . . .	56
5.7	Explanation of the measurement angle $\alpha$ and the resultant angles for the different number of cycles. . . . .	57
5.8	CT measurement of the crack of the female part of connector 13. . . . .	57
5.9	Sample preparation before SEM. . . . .	59
5.10	Measurement of inner and outside layers of the plating applied to the pin and socket. . . . .	59
5.11	EDS analysis of the inner surface of the socket and correspondent spectrum. . . . .	60



5.12	Pictures of contact surfaces of connector 12 and 13 after the reliability stress testing. . . .	61
5.13	Localized EDS 1 and EDS 2 analysis of connector 12. . . . .	61
5.14	EDS analysis performed at the tip of the pin (connector 12). . . . .	61
5.15	Analysis of fractured surface of connector 13. . . . .	62
6.1	Socket and pin full model and table with the properties of a C17300 alloys under condition TH04. . . . .	64
6.2	Final geometry used to simulate the contact between socket and pin. . . . .	64
6.3	Representation of the contact at different steps. . . . .	65
6.4	Study of the convergence of the mesh. . . . .	66
6.5	von Mises stresses at different displacements assuming only the elasticity regime. . . . .	67
6.6	Principal strain components. . . . .	67
6.7	Stress-strain plot considered for the simulations. . . . .	68
6.8	von Mises stresses at different displacements assuming the plasticity regime. . . . .	68
6.9	Effective plastic strain for a displacement of 1.3 mm. . . . .	69
6.10	S-N curve of C17200 TH04 rod and table showing the correspondent values inserted in COMSOL Multiphysics. . . . .	70
6.11	Cycles to failure obtained using the fatigue module available by COMSOL Multiphysics software. . . . .	70
6.12	Comparison of the critical zone between the FEM simulation and the results from the physical characterization methods. . . . .	71
A.1	1.85 mm pin LPC connector drawings according IEEE P287 standard. . . . .	83
B.1	Connector 12 housing appearance after an accelerated testing. . . . .	84
B.2	Pictures of connector 12 appearance for different number of cycles. . . . .	85
B.3	Pictures of connector 13 appearance from 6,000 to 30,000 cycles. . . . .	86
B.4	Pictures of connector 13 appearance from 30,000 to 60,000 cycles. . . . .	87
C.1	Pin depth versus number of cycles for the 14 tested connectors. . . . .	88
C.2	Insertion and withdrawal forces versus number of cycles for the 14 tested connectors. . .	89
C.3	Concentricity of the centre contacts versus number of cycles for the 14 tested connectors.	90
D.1	Measured S12 of connector 1 on the left and measured S12 of connector 2 on the right. .	91
D.2	Measured S12 of connector 3 on the left and measured S12 of connector 4 on the right. .	91
D.3	Measured S12 of connector 5 on the left and measured S12 of connector 6 on the right. .	92
D.4	Measured S12 of connector 7 on the left and measured S12 of connector 8 on the right. .	92
D.5	Measured S12 of connector 9 on the left and measured S12 of connector 10 on the right.	92
D.6	Measured S12 of connector 11 on the left and measured S12 of connector 12 on the right.	93
D.7	Measured S11 (left) and S12 (right) after 60,000 cycles for connector 1. . . . .	93
D.8	Measured S11 (left) and S12 (right) after 60,000 cycles for connector 2. . . . .	93

D.9	Measured S11 (left) and S12 (right) after 60,000 cycles for connector 3. . . . .	94
D.10	Measured S11 (left) and S12 (right) after 60,000 cycles for connector 4. . . . .	94
D.11	Measured S11 (left) and S12 (right) after 60,000 cycles for connector 5. . . . .	94
D.12	Measured S11 (left) and S12 (right) after 60,000 cycles for connector 6. . . . .	95
D.13	Measured S11 (left) and S12 (right) after 60,000 cycles for connector 7. . . . .	95
D.14	Measured S11 (left) and S12 (right) after 60,000 cycles for connector 8. . . . .	95
D.15	Measured S11 (left) and S12 (right) after 60,000 cycles for connector 9. . . . .	96
D.16	Measured S11 (left) and S12 (right) after 60,000 cycles for connector 10. . . . .	96
D.17	Measured S11 (left) and S12 (right) after 30,000 cycles for connector 11. . . . .	96
D.18	Measured S11 (left) and S12 (right) after 30,000 cycles for connector 12. . . . .	97
D.19	Measured S11 (left) and S12 (right) after 60,000 cycles for connector 13. . . . .	97
D.20	Measured S11 (left) and S12 (right) after 60,000 cycles for connector 14. . . . .	97
E.1	Components of stress tensor obtained for a plastic simulation. . . . .	99
E.2	Components of strain tensor obtained for a plastic simulation. . . . .	99
F.1	Surface mapping analysis performed from a top view of connector 12. . . . .	100
F.2	Pictures of different areas of the socket fractured surface. . . . .	100

# Nomenclature

## Greek symbols

$\alpha$	Angle of socket aperture
$\beta$	Shape parameter
$\eta$	Scale parameter
$\Gamma$	Gamma function
$\lambda$	Failure rate
$\mu$	Median time
$\nu$	Poisson ratio
$\Phi$	Standard Normal Cumulative Distribution Function
$\rho$	Density
$\sigma$	Stress
$\sigma_{ult}$	Ultimate stress
$\sigma_y$	Yield stress
$\sigma_v$	von Mises Stress
$\varepsilon$	Strain
$\varepsilon^{pl}$	Effective Plastic Strain

## Roman symbols

$E$	Elastic modulus
-----	-----------------

## Subscripts

$\infty$	Free-stream condition
$x, y, z$	Cartesian components



# Glossary

<b>ACT</b>	Accelerated Test
<b>AGREE</b>	Advisory Group on Reliability of Electronic Systems
<b>ANRFCCC</b>	Army-Navy RF Cable Coordinating Committee
<b>ASESA</b>	Armed Services Electro-Standards Agency
<b>ATE</b>	Automatic Test Equipment
<b>CDF</b>	Cumulative Distribution Function
<b>CT</b>	Computerized Tomography
<b>DC</b>	Direct Current
<b>DoD</b>	Department of Defense
<b>DUT</b>	Device Under Test
<b>FEM</b>	Finite Element Method
<b>FMA</b>	Failure Mode Analysis
<b>HCF</b>	High Cycle to Failure
<b>HD</b>	High Definition
<b>IC</b>	Integrated Circuits
<b>IEEE</b>	Institute of Electrical and Electronics Engineers
<b>IoT</b>	Internet of Things
<b>LCF</b>	Low Cycle to Failure
<b>MTTF</b>	Mean Time to Failure
<b>NR</b>	New Radio
<b>PCB</b>	Printed Circuit Board
<b>PDF</b>	Probability Distribution Function
<b>PoF</b>	Physics of Failure
<b>RF</b>	Radio Frequency
<b>SEM</b>	Scanning Electron Microscope
<b>S-Parameters</b>	Scattering Parameters
<b>VNA</b>	Vector Network Analyser
<b>WiGig</b>	Wireless Gigabit



# Chapter 1

## Introduction

### 1.1 Motivation

In the last decades, there has been a considerable transformation on the telecommunication and networking fields due to the demand for the transmission of large amounts of data. Furthermore, the evolution of wireless communication technologies is further accelerating this transformation. 5G is the new upcoming wireless revolution because it will allow the delivery of ultra-broadband services, including High Definition (HD) and ultra-HD video streaming, thus enabling a starting point in the world of machines (like autonomous vehicles) as well as a connection of millions of industrial sensors and a magnitude of wearable consumer devices, also mentioned as the Internet of Things (IoT) [1, 2].

The constant developments in the semiconductor industry made this possible. It is an incredible feat of technology that the manufacture of integrated circuits (IC) with billions of individual transistors, each with feature sizes as small as 7 nanometers is possible today. It was the development of very small transistor sizes that allows ICs for wireless applications to work at millimeter wave (mmwave) frequencies (e.g. 24 to 70 GHz). An equal important requirement is the need to make sure that the manufactured IC works as expected during its expected lifetime (several years or even decades depending on the application) [3].

The semiconductor manufacturing is roughly divided into two stages. The first stage named front-end, deals with the manufacturing of the IC in silicon wafers and is composed by a variety of lithographic, chemical and polishing processes. The second stage, designated as back-end, deals with the packaging of the IC and its testing to make sure it works as expected when shipped to the end-customer [3].

It is in this back-end stage that Automatic Test Equipment (ATE) is used to test the IC before packaging (wafer testing) and after packaging (package testing). Several advanced techniques are used to test a modern IC to guarantee that all of the billion transistors are working properly. Figure 1.1 shows an example of an ATE test cell for package testing.



Figure 1.1: Example of an ATE test cell for DDR testing composed of an ATE system and a robotic handler that inserts the packaged integrated circuits into the ATE system (256 units in parallel).

For these new mmwave wireless applications, ATE companies must develop new test solutions to face these new challenges. One key challenge lies in the frequencies for 5G-NR (New Radio), including 24 GHz, 28 GHz, and 39 GHz and even higher, as well as 56 GHz to 72 GHz frequencies for wireless gigabit (WiGig) devices. Note that not only is important to be able to test the IC at these frequencies, but also to do it with a low cost, because the target market is the consumer market. The military industry has been working at these frequencies already for a long time, but using more complex technologies and also more expensive test solutions which cannot be leveraged for 5G applications [4–8].

The test of an IC in an ATE system requires a reliable connection between the ATE and the printed circuit board (PCB) test fixture where the device under test (DUT) is located. One of the ways to ensure a proper connectivity for high-frequency applications is to use a blind mating coaxial connector. For 5G mmwave applications, one interesting class of mmwave connectors is the 1.85 mm. Apart from the electrical performance of the connector itself, its reliability with multiple dock and undocking cycles is also critical [9].

The goal of this thesis is to test the reliability of a 1.85 mm blind mating interconnect composed of two individual connectors (male and female connector), that were custom designed by Signal Microwave for Advantest. This blind mating interconnect is used on the Advantest V93000 wavescale millimeter card-cage ATE system. To define and execute a proper reliability test plan to test this connector, it required the collaboration of several companies and engineers.

The present thesis was developed to obtain the degree of Masters of Science in Materials Engineering. Although the main topic is about electrical engineering, this project is also very interesting from the viewpoint of fields such as materials engineering, as well as mechanical engineering. Thus, in the present thesis, this broader, multidisciplinary approach was taken.



## 1.2 Automatic Test Equipment (ATE)

ATE systems usually consist of three elements: a test head, a mainframe and a manipulator. There is also a workstation that controls the ATE system. In the context of this thesis, the critical part is how the ATE system connects to the IC under test. The DUT resides in a PCB test fixture that is responsible for connecting the DUT to the ATE measurement instruments. The DUT PCB test fixture forms the electrical interface between the ATE tester and the DUT, assuring that a temporary electrical connection is made between the DUT and the measurement instruments in the ATE system [10, 11]. Figure 1.2 shows a picture of a commercial ATE system with a DUT PCB test fixture docked used for package testing and wafer probing.

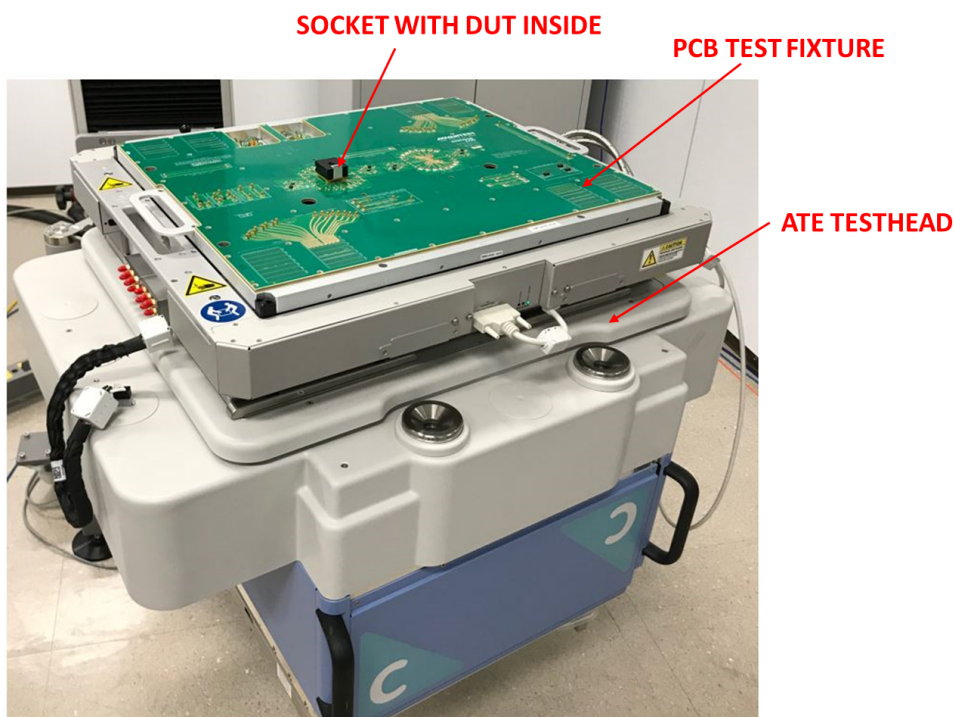


Figure 1.2: Advantest V93000 ATE system with a DUT test fixture IC socket based testing application.

A 5G integrated circuit has multiple types of interconnects (power supply, digital, RF and mmwave). The ATE system also needs to provide those interconnects so that electrical signals can be sent to and measured in the DUT. Figure 1.3 shows an example of the different electrical interconnects of a commercial ATE system for 5G applications. Each interconnect is made using a different type of connector. This is not only to minimize the cost, but also because depending on the type of electrical performance and density required, a specific interconnect technology is chosen.

Depending if the ATE system is testing a silicon wafer or an individual packaged device, the DUT PCB test fixture is different. Figure 1.4 shows an example of a PCB DUT test fixture for 5G wafer probing. During wafer probing, a robotic machine manipulates silicon wafers where individual dies are tested by the ATE system. Note that the PCB DUT test fixture shown in Figure 1.4 and 1.5 contain in its right side the 1.85 mm blind mating connectors in charge of the mating connection performed by the

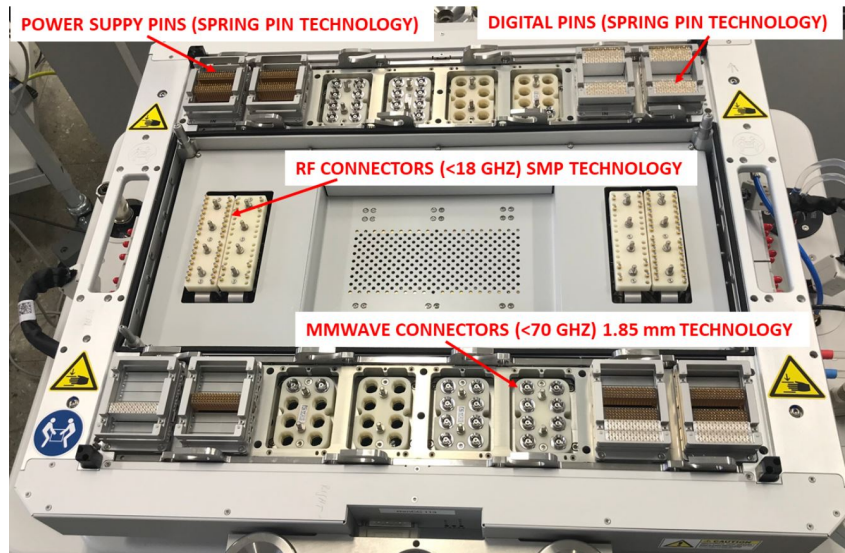


Figure 1.3: Picture of the interconnect interface of an Advantest V93000 ATE system.

ATE interconnect interface.

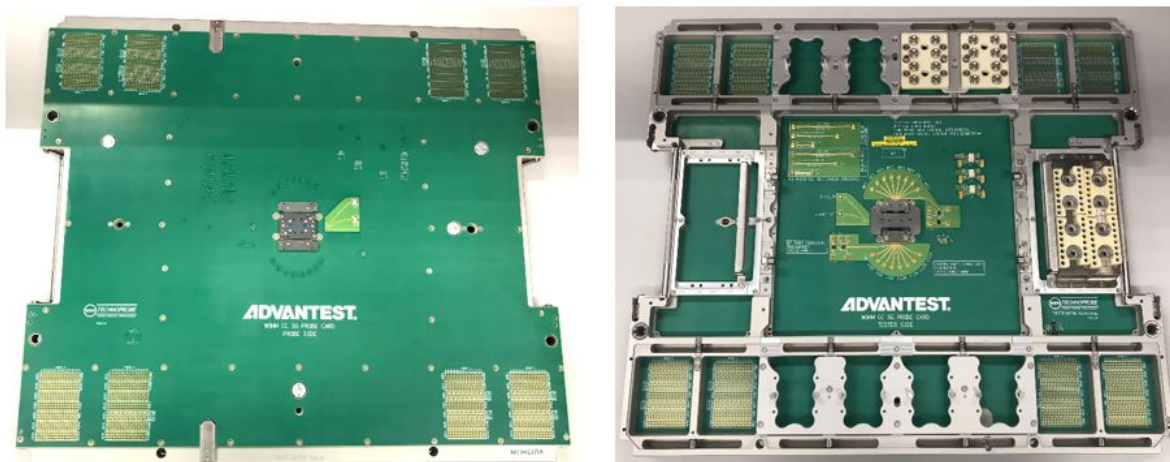


Figure 1.4: Top and bottom part of a DUT wafer probing test fixture.

In the same way probers manipulate wafers, in package testing, handlers are used to manipulate packaged devices. Figure 1.5 shows an example of a DUT PCB test fixture for package testing of a 5G application.

The critical point of integrated circuit testing for both wafer probing or package testing, is to assure that during the test, a reliable connection is established between the ATE system and the DUT printed circuit board test fixture which connects to the DUT, allied with the required electrical performance and reliability.

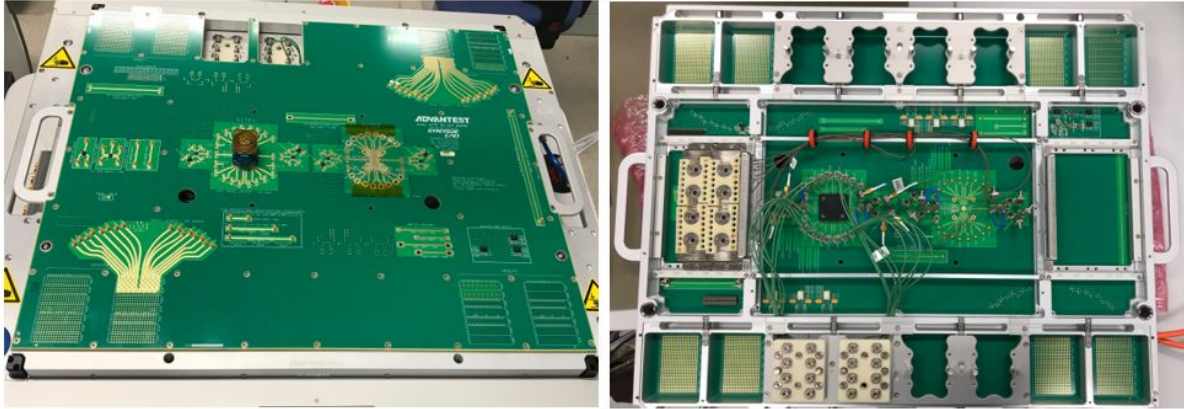


Figure 1.5: Top and bottom part of a DUT package testing test test fixture.

### 1.3 Objectives

The object of this thesis is to study the maximum number of docking/undocking cycles that a blind mating coaxial interconnect can achieve before it no longer complies with the needed electrical requirements. The main goal of this thesis is, therefore, to present a reliability evaluation of the 1.85 mm blind mating coaxial connector used on a commercial ATE system (Advantest V93000 ATE system). The following steps were taken and are described in the present work:

- To implement the defined reliability measurement plan, an experimental measurement setup composed of an ATE system and multiple measurement instruments must be implemented together with a computer code, in this case a matlab script, that controls the instruments and collects the measured data;
- Define the correlation of the electrical, mechanical and dimensional measurements and how they relate to the failure of the blind mating interconnect;
- Based on the connectors tested, a reliability model has to be developed using statistical distributions that allows to infer, under the same conditions, the expected number of cycles before failure for an ATE system with multiple connectors;
- In the case that a connectors fails, perform a failure analysis on the connector using the Scanning Electron Microscope and the Computed Tomography Scan. The usage of these techniques allow to better understand why the components have failed;
- Finally, based on the Finite Element Method, a mechanical simulation is performed to evaluate the mechanical stresses and strains that occur inside the connector, so that a correlation can be done with the failure mechanisms identified by the experimental results.

## 1.4 Thesis Outline

Chapter 1 presents an overview of the blind mating coaxial connectors used for ATE applications, as well as a very basic introduction to commercial ATE systems. It also explains the main objectives of this thesis.

In the second chapter, an insight of the state of the art is provided, by means of a literature review. It begins with the standards, materials and specifications used for the manufacture and testing of coaxial connectors. After that, the 1.85 mm blind mating coaxial connector used along this thesis is presented. Finally, an outline on the reliability engineering topic is described, as well as some examples of reliability models used in coaxial connectors.

Chapter 3 presents the methodology developed to test the connectors. It describes how the measurement setup was implemented, as well as the testing conditions, equipment and performed measurements.

In Chapter 4 the measurement results are presented and discussed. The results are separated in measurements done during the cyclic testing and a development of a reliability model.

Chapter 5 presents two techniques (SEM and CT scan) used to perform a physical analysis characterization of the connector.

Chapter 6 features the results obtained for mechanical simulations using the Finite Element Method. The results obtained in this chapter are discussed and compared with to the ones on chapters 4 and 5.

The last chapter summarizes the main achievements acquired along this thesis together with some suggestions for future work regarding the testing of blind mating coaxial connectors.

# Chapter 2

## Background

In order to develop a plan on how to test the reliability of a 1.85 mm blind mating connector, a literature review on this subject is critical. First of all, the relevant standards used in this field are analysed. Secondly, an overview on the materials, specifications and parameters of the coaxial connectors for the different types of coaxial connectors is discussed. Finally, a reliability revision is addressed, where there are some examples of reliability models applied to coaxial connectors.

### 2.1 Standards

Coaxial Connectors have been of critical importance for electrical measurements. After the Second World War, the hunt of higher frequencies for RF cables, rigid transmission lines and connectors for radio and radar equipment forced the joint US Army-Navy RF Cable Coordinating Committee (ANRFCCC) to establish standards in terms of electrical and mechanical specifications. Later on, this committee was incorporated into the Armed Services Electro-Standards Agency (ASESA) which continued the standardization of connectors in US military. In the early sixties, the subcommittee on RF connectors under the American Standards Association (ASA) helped on the military improvement of coaxial connectors which led to the creation of MIL-C-39012 standard. Furthermore, the IEEE 287 subcommittee on precision coaxial connectors was created in 1962 under the IEEE Instrumentation and Measurement Society (in 1968, 14 mm and 7 mm coaxial connectors were standardized by the IEEE 287 standard). In 1970, frequencies of 40 GHz were already part of this standard and after 10 years there was the step over up to 60 GHz. So, in the last decades, frequency limits have been constantly increased. Nowadays the 1 mm coaxial connector which has a maximum frequency of 110 GHz, is already a reality of industry future applications [12, 13].

#### 2.1.1 IEEE 287 Standard

The IEEE standard that specifies coaxial connectors for precision electrical measurements is the IEEE 287. The last update was released in 2007, where the subcommittee gathered to include the standardization of the 1.0 mm connector. The following regulation presents performance requirements for

eight different types of connectors, such as 3.5 mm, 2.92 mm, 1.85 mm and 1 mm connectors. It describes test methods and concepts around the connector technology. Furthermore, for each connector the detailed specifications in terms of electrical, mechanical and environmental are presented. In the appendix A, there are the respective drawings and tolerances for the 1.85 mm connector. From all the specifications described in this standard, electrically, the most relevant ones are the cut off frequency and the contact resistance together with its repeatability. In terms of mechanical specifications, the important ones are the maximum insertion and minimum withdrawal forces and connect/disconnect life. Finally, under environmental specifications the temperature and humidity are of most interest. Table 2.1 presents the relevant specifications for the 1.85 mm connector [14].

<b>Electrical Specifications</b>	
Cutoff Frequency	73.3 GHz
Contact Resistance	0.15 mΩ
<b>Mechanical Specifications</b>	
Connect/Disconnect Life	5,000 cycles
Maximum Insertion Force	0.9 N
Minimum Withdrawal Force	0.14 N
<b>Environmental Specifications</b>	
Temperature	13-33 °C
Humidity	20-80 % RH

Table 2.1: Electrical, mechanical and environmental specifications for a 1.85 mm coaxial connector [14].

Although this standard addresses coaxial connectors, it is necessary to mention that it is specified for connectors that are mated through a threaded nut. Therefore, for other designs such as twist, bayonet or blind mating, this standard is not applicable.

**2.1.2 IPC-9592 Standard**

The IPC-9592 standard exhibits a set of several specifications and methods that consider the quality, safety and reliability of power conversion devices that are part of the electronics industry. The IPC-9592 standard makes references to the JESD22 - A101 (developed by JEDEC commites for microelectronics industry), which defines a cyclic temperature humidity bias (THB) test. The main goal of the JESD22 - 101 is to evaluate the reliability of non-hermetic packaged solid-state devices in humid environments. The conditions for this test are 85 % humidity with a temperature of 85°C during 72 hours. This test is considered to be a high temperature/high humidity test of the Highly Accelerated Stress Test (HAST) standards. This reliability test is useful to determine the expected operating life of several devices [15–18].

**2.1.3 MIL Standards**

MIL standards were initially created for military use, but they have been also adopted for commercial applications in several cases. The standard MIL-PRF-39012E, differently to IEEE 287, classifies the

connectors according to class, category and PIN (Part Identifying Number). It originally dates back to 13 July of 1995, with the latest revision on 27 April 2005. It includes the performance specification for RF coaxial connectors where it involves general requirements and tests used with flexible RF cables and certain other types of coaxial transmission lines. Contrary to IEEE 287, specifications are centred on the production processes and materials of connectors to assure its performance. From all the points covered, the main focus are on the centre contacts, contact bodies, spring members and centre contact retention. For the centre contact parts (pin and socket) a minimum of gold thickness of  $1.27 \mu m$  ( $5 \times 10^{-5}$  inch) is required over a minimum thickness of nickel (silver under plate is not allowed). In the case of connector bodies, if it is a brass body, it shall be silver plated with a minimum thickness of 0.005 mm over a copper under plate or nickel plated. For a copper beryllium body, it shall be gold plated to a minimum thickness of  $1.27 \mu m$  ( $5 \times 10^{-5}$  inch) over a copper flash. Apart from that, it has some directives on some methods of inspection, durability and corrosion applied to the connectors [19]. Another examples of other MIL standards used, are the MIL-STD-348 and MIL-PRF-29012 which address the manufacturing of coaxial connectors. MIL 348 standard provides a dimension control of the standard interfaces creating a basis of a reliable design and construction of these components.

Other MIL standards are also important, not because of connector manufacturing (design, specifications and materials), but because of testing them. MIL 202G focus on uniform methods for testing electronic and electrical component parts, including basic environment tests to determine resistance to deleterious effects of natural elements and conditions surrounding military operations, physical and electrical tests [20]. MIL-HDBK-217 is a standard for reliability prediction of electronic equipment where there is information on how to predict failure rates of different electronic devices according to different factors, like temperature, voltage and environment. It is present a section in this standard for coaxial RF connectors, where the failure rate can be obtained according the following expression:

$$\lambda_p = \lambda_T \lambda_K \lambda_Q \lambda_E \quad \text{Failures}/10^6 \text{Hours} \quad (2.1)$$

Where  $\lambda_p$  represents the type of connector (RF coaxial, rectangular, hexagonal, triaxial. . .),  $\lambda_T$  is a temperature factor,  $\lambda_K$  is the number of mating/unmating cycles,  $\lambda_Q$  is the quality factor and  $\lambda_E$  is the environment factor. The development of this formula is not described in this standard. Several engineers that have compared the result of this expression with field experience, do not agree with the application of this MIL standard into reliability predictions [21].

## 2.2 Coaxial Connectors

Coaxial connectors are critical parts for test and measurement. Some characteristics like dimensions, machining tolerances, connector materials, plating and finish are critical for a high-level reliability. In these days, there are a considerable number of manufacturers of such types of connectors. Some examples are Signal Microwave, Anritsu, Rosenberger, Spinner and many others [13, 22].

## 2.2.1 Materials

The list of materials used on a coaxial connector is extensive, and the choice of them influences the connector mechanical, electrical and environmental specifications. The choice of each material, must take into consideration the electrical conductivity, machinability and hardness so that the wear and deterioration is minimal with the increasing number of cycles, resulting in high reliability and electrical performance.

Concerning the centre conductors (pin and socket), copper-zinc or copper-beryllium are the usual alloys. The copper-beryllium alloys are known to have a high-strength capability. The typical uses of these alloys, are for electrical contacts that open and close a large number of times, where a high strength, anelasticity and fatigue and creep resistance allied to a high electrical conductivity and corrosion resistance [23–25]. Afterwards, a coating of gold or silver is applied, which are excellent conductors and also resistant to corrosion. Despite the fact that silver is less expensive than gold, it is usually put aside because it starts to tarnish when exposed to contaminants like sulphur-based materials. Although to minimize the gold diffusion, nickel is used as an under plating metal under the gold finishing layer [26].

In the interior of both male and female pairs, coaxial connectors have a part that sustains the pin and socket which is named bead, and its manufactured using a dielectric material so that it does not short the pin/socket to the connector body which is grounded. The dielectric material of the bead must be as near to air as possible considering the frequency range proposed. In order to approximate even more the value of the dielectric material to air, it is common to make very small holes in the periphery of the bead. The bead material is usually polychlorotrifluoroethylene (PCFTE, well-known as Neoflon) or a thermoplastic with a similar dielectric capability. The bead has to offer mechanical stability to the pin and socket and minimize reflections through the connector with a low insertion loss, typically lower than 1 dB [26]. It also needs to support the working temperature range of the connector.

For the connector housing, brass or stainless-steel are the two usual options. Although stainless steel is higher in cost than brass, it provides higher durability and an outstanding corrosion resistance. The spring of the float mount (usually made of tool steel) that is included in the connector housing of a blind mating connector, is responsible to apply mechanical forces to keep the contact interfaces between the male and female connected. The remaining parts of a coaxial connector like the screws, although not as important as the others since they are not in direct contact, are usually made of the same material than the housing [13].

## 2.2.2 Specifications and Parameters

To increase the maximum usable frequency of a connector, the standard approach is to reduce the mechanical dimensions of a connector. But it also increases the probability of a connector failure due to



mechanical and electrical constraints. To ensure reliable mechanical mating, electrical repeatability and a moderate cost, some characteristics should be taken in account, such as concentricity, withdrawal and insertion forces and contact location.

The concentricity is a dimensional parameter and defines how centred are both the pin and socket relatively to the housing of the connector, so when the contact is established, the mechanical stresses during contact increase with higher concentricity values. Another important aspect is the contact location, which determines the excessive recession causing a high reflection and also it cannot be positive. This results in a degradation of the electrical performance. Finally, both withdrawal and insertion forces determine the physical contact between the pin and the socket. These are sliding forces with different directions, where the insertion force characterizes the insertion of the pin into the socket and the withdrawal force represents the opposite, i.e. the removal of the pin from the socket. Higher values in force mean higher sliding action, which may be due to lower socket apertures or a increased concentricity. When the values of these forces are close to zero, it means there is no contact between centre contacts which results in a connector failure [26].

The common failures are due to excessive wear, out of tolerance contacts, dirty mating surfaces, over torqueing, misalignment and rotation during mating cycle. The connector performance is measured by a Vector Network Analyser (VNA), which will characterize the connector both in terms of performance and repeatability [13].

### **2.2.3 Testing and Evaluation**

The electrical evaluation of coaxial connectors is done in accordance to a different number of parameters, namely the insertion loss (IL) and the maximum voltage standing wave ratio (VSWR) or return loss that are measured using a VNA. Extra parameters to be considered, could be the maximum operating voltage, insulation resistance, dielectric withstanding voltage, operating temperature range and operating lifetime expressed as maximum number of docking cycles. All of these parameters, depend on the application of the connector and its environment variables. For example, the cut-off frequency is not easily achieved, because the internal components of a connector create transitions/discontinuities between the air and the various materials which creates resonances that degrades the upper theoretical frequency [27, 28].

The Vector Network Analyser (VNA) generates a sinusoidal signal to test the DUT and the analyser measures the response of the DUT to that signal by measuring the difference between the 2 signals (amplitude and phase). Among all functionalities of a VNA, the main metric in this project are in the S-parameters, also commonly known as scattering parameters, used to describe how a device alters voltage waves that are applied to the ports. The reason for referring to S-parameters is that currents and voltages are not easy to measure at high frequencies, so the S-parameters are basically an ex-

tension of the transmission line theory in which are treated as incident and reflected travelling waves. S-parameters determine completely the electrical performance of a connector, i.e. whether there is loss or gain through the DUT. The ratios between reflected to incident and transmitted to incident power rectified to voltage allow to obtain the S-parameters or a scattering matrix. In a two-port device, S11 is named input reflection coefficient, S21 forward transmission coefficient, S22 output reflection coefficient and S12 reverse transmission coefficient. The S-parameters output come in decibels because a logarithmic scale is typically used. As an example, S11 indicates the power that is reflected or scattered out of a structure at port 1 divided by the power at the input applied in port 1 [27, 28]. Figure 2.1 shows a scheme on how S-parameters are obtained inside a 2-port VNA.

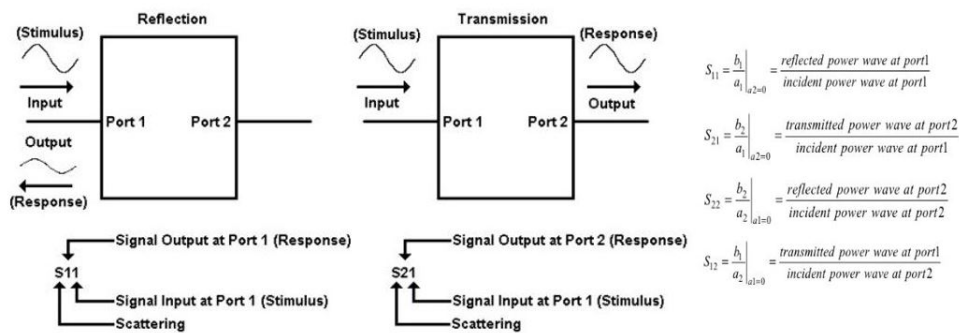


Figure 2.1: S-parameters explanation and respective equations [29, 30].

## 2.2.4 Types of Coaxial Connectors

The choice of a coaxial connector, depends on its application goal. Regarding the connector design, two distinct categories can be identified for coaxial connectors: sexless or sexed. A sexless connector is a connector that has both parts identical and a sexed connector, also known as pin and socket type, has a male (pin) and a female (socket) part, whose configuration together form a pair. For a pin-socket type coaxial connector, the mating or coupling can also be of different types, such as threaded, twist or bayonet connections (Figure 2.2). Note that for the same coaxial connector types, the price of it made by 2 different manufacturers can be totally different depending on the design (which influences in manufacturing) and materials [12]. Table 2.2 summarizes the list of some coaxial connectors available with its respective coupling type and frequency range:

Connector Type	Coupling	Typical Frequency Range	Connector Type	Coupling	Typical Frequency Range
UHF	Threaded	DC to 300 MHz	7 mm	Threaded	DC to 18 GHz
BNC	Twist-lock	DC to 4 GHz	3.5 mm	Threaded	DC to 34 GHz
TNC	Threaded	DC to 12.4 GHz	2.92 mm	Threaded	DC to 40 GHz
Type N	Threaded	DC to 11 GHz	2.4 mm	Threaded	DC to 50 GHz
SMA	Threaded	DC to 18 GHz	1.85 mm	Threaded	DC to 65 GHz
SC	Twist-lock	DC to 11 GHz	1 mm	Threaded	DC to 110 GHz
			0.8 mm	Threaded	DC to 125 GHz

Table 2.2: Examples of different connectors used from low RF to mmwave frequencies [12].



Figure 2.2: Different Types of Coaxial Connectors.

Due to the constant increase in frequency, in some cases, the connector manufacturers developed connectors that were ahead of current application needs which are examples of the 0.8 and 1 mm connectors. There is currently a new connector being introduced by some manufacturers, which is the 1.35 mm connector (specified up to 90 GHz maximum frequency). Among the large list of coaxial connectors, the mmWave connectors in usage are the ones in the region above 18 GHz and are pin-socket types [32].

## 2.2.5 Blind Mating 1.85 mm Coaxial Connector

The 1.85 mm connector was first introduced by HP/Agilent, and initially had a maximum frequency range of 65 GHz. Improvements on the connector design, allowed the jump to frequencies in the order of 67 GHz and more recently to 70 GHz. One of the advantages of this connector is the mechanical compatibility with the 2.4 mm coaxial connector [33].

The incorporation of a blind mating coaxial connector to settle the connection between the ATE DUT PCB test fixture and the DUT on an ATE test cell are of critical importance. The fundamental reason for the choice of the 1.85 mm connector is linked with the frequency of interest for a 5G and WiGig testing application. As addressed in chapter 1, specifically for a range of frequencies of 24-70 GHz, the choice was to use the 1.85 mm connector.

As expressed in Section 2.1, the existing standards are for threaded connectors only, which creates challenges not only in terms of the design, electrical, mechanical and environmental specifications, but also in testing and reliability for blind mating coaxial connectors [34]. The development of this connector is explained in [9] and the manufacture of the pin and socket was made according to the MIL-PRF-39012 and IEEE 287 standards. Table 2.3 presents the target specifications for the connector, as well as the list of materials.

The C17200 and C17300 alloys, also called "gold alloys", are known to be high strength alloys that are usually age hardened. The C17300 is the chosen alloy for the centre conductor of the coaxial connectors due to the improved machinability. The alloy is composed by 1-2 wt% beryllium, 0.2-0.6 wt% lead,

<b>Mechanical</b>	
Insertion force	0.9 N
Withdrawal force	0.28 N
Contact durability	20,000 Cycles
<b>Electrical</b>	
Maximum Frequency	67 GHz
Impedance	50 $\Omega$
Centre Conductor Resistance	3 m $\Omega$ Maximum
<b>Environmental</b>	
Temperature	0-55 °C
<b>Materials</b>	
Housing	303 Stainless Steel
Dielectric (Bead)	Neoflon ASTM D1430 [35]
Centre Conductor	BeCu C17300 TH04 [23]

Table 2.3: Target specifications and materials for the Blind Mating 1.85 mm connector [36].

0.2-0.6 wt% of Nickel+cobalt and 96.8-98.6 wt% of copper (Cu). The beryllium increases the ultimate strength of the copper-beryllium alloy, though the percentage added does not compromise the electrical conductivity (lower addition levels of beryllium such as 0.2-0.7 wt% have higher conductivity) [23, 24].

In order to obtain this increase in resistance, a heat treatment of precipitation hardening is performed. It involves a high temperature heating and quenching to obtain a solid supersaturated solution, and afterwards the alloy is aged (reheated at low temperatures) to allow the excess of solute precipitate removal. The aging applied in this case is at a temperature of 315 °C (600 F) during 2 hours in an inert atmosphere to create the condition TH04. Different aging temperatures influence the mechanical resistance of the final alloy. The product form of these alloys are commercialized as rod, bar, plate, tubing or strip [23–25, 37, 38].

To manufacture the centre conductors of the 1.85 mm blind mating connector, rods were selected which are then machined using CNC (Computer Numerical Control) equipment. After the centre conductors are age hardened and attain the final shape, nickel is electro plated (under plate) per QQ-N-290A [39] with a thickness between 1.27  $\mu\text{m}$  (0.00005 inch) and 3.81  $\mu\text{m}$  (0.00015 inch). Finally, the gold plate is deposited over nickel, according to MIL-DLT-45204 [40], Type II, Grade C and with a thickness between 2.54  $\mu\text{m}$  (0.00010 inch) and 3.81  $\mu\text{m}$  (0.00015 inch).

The bead chosen is PCTFE (polychlorotrifluoroethylene) which is formed by the polymerization of the homopolymer chlorotrifluoroethylene. This material has a high mechanical strength and low elongation. A extrusion process is performed followed by machining where the holes in the periphery of the bead are created. The bead material offers excellent corrosion resistance and electrical insulation, high compressing strength and a useful temperature range of -200 °C (-8 F) to +200 °C (392 F) [35, 41].

The 1.85 mm blind mating coaxial connector 3D model that is the object of this thesis is shown in Figure 2.3. Figure 2.4 shows the manufactured connectors after assembling the several materials.

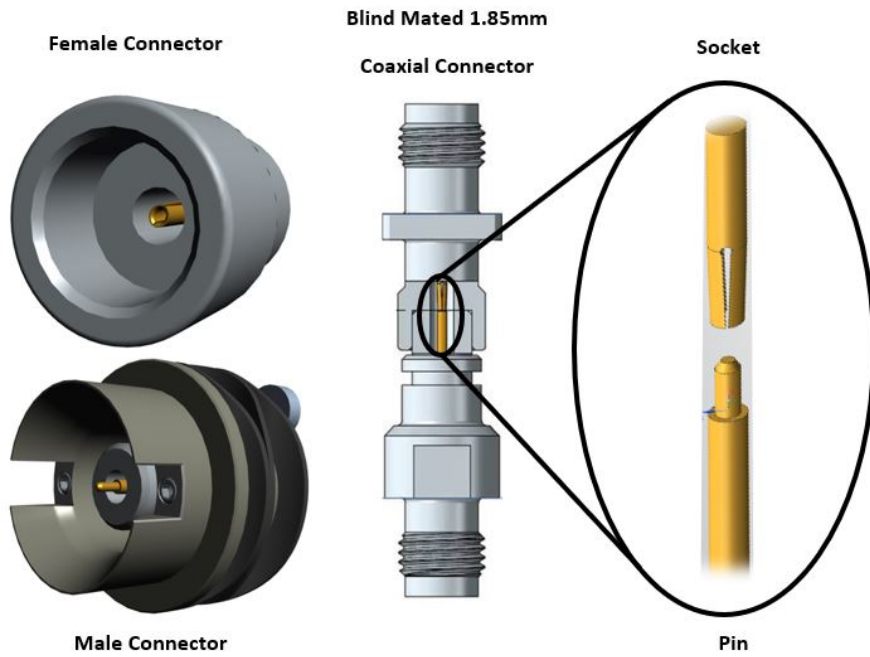


Figure 2.3: 3D models of the custom blind mating 1.85 mm coaxial connector designed for the Advantest V93000 ATE system.

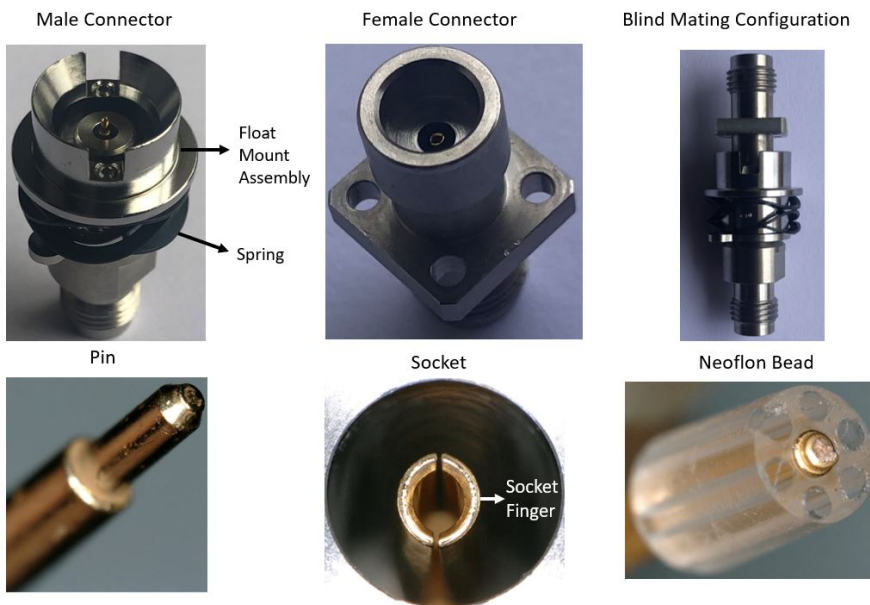


Figure 2.4: Manufactured Blind Mating 1.85 mm coaxial connector with its components.

## 2.3 Reliability Engineering

In every engineering field, during design, service, manufacture and development, reliability engineering must be taken in consideration. The common way to quantify it, is through the use of mathematical and statistical methods. Even though, problems may arise due to a variation of factors, such as operating cycles and reliability past data information. For this reason, reliability engineering rounds off the quality control where the study of quality itself is linked. The main goal of reliability engineering is to identify and correct the causes of failure, prevent and/or reduce the frequency of failures and apply methods to analyse reliability data that allow to estimate reliability [42].

Reliability study dates back to around 80 years ago, when during the World War II, the advance in electronics to control machinery, radar systems of army and military avionics led to constant early failures. On the 7<sup>th</sup> of December 1950, the low reliability of electrical and electronic systems enable the Department of Defense (DoD) to create the Advisory Group on Reliability of Electronic Systems (AGRES). Articles and books were published on reliability for the last decades that resulted in statistical methods and study of physics of failure that were fundamental to make what reliability engineering is today.

There is not a single definition of reliability. According to the most common definition, reliability is defined as the probability that a certain product does not fail for a given period of time and for certain operational and environmental conditions [43]. In a simpler way, reliability is described as the probability not to fail (probability of success) and is described by expression 2.2.

$$R = e^{-\lambda t} \quad (2.2)$$

On the other hand, F(t) is the probability of a failure or the unreliability, meaning the probability that a device will fail until the moment t. The distribution function for R(t) is the cumulative distribution function (CDF) and for F(t) is the probability density function (PDF). Other parameters in the study of reliability are the mean time to failure (MTTF) and hazard rate. MTTF is applied in systems which are non-repairable [43, 44]. Expression 2.3 defines the failure rate:

$$\lambda(t) = \frac{f(t)}{R(t)} \quad (2.3)$$

where  $\lambda$  is the failure or hazard rate (defined as the rate that a device or component is expected to fail) and t is the time.

The parameters that weigh on reliability performance are physical, mechanical, electrical and thermal mechanisms for a determined time. The reasons why a component or system fails may be of different natures, like over stressing, incorrect design, incorrect use and/or maintenance, failures caused by wear-out mechanisms or by other time dependent mechanisms. The methodology applied to quantify reliability is different for each component. Although, for every component there are three periods of time

that depend on the frequency of failure and on the failure cause pattern. The following three periods are shown in Figure 2.5, where infant mortality period is characterized by high failure rates (usually failures caused by design problems, manufacture or misapplication), constant failure rate period results by limitations concerned to design, changes of environments and unexpected accidents caused by use or maintenance and the wear-out period are failures caused by an old age (normally associated with fatigue or depletion of materials) in which metal becomes brittle [42, 45].

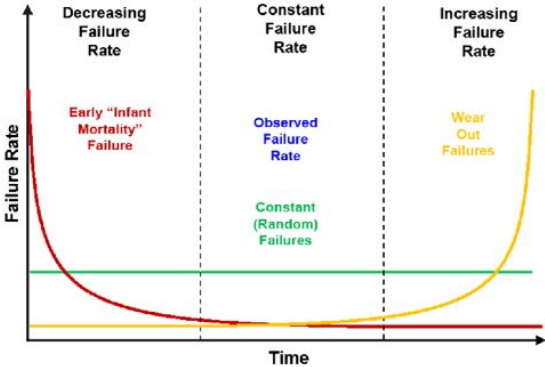


Figure 2.5: Bathtub curve with different reliability regimes.

An increasing number of samples is favourable to obtain an accurate reliability, nevertheless there are cases where the availability of samples is not possible due to for example: high costs. At this point, the importance of reliability assessment by statistical functions gains importance. Data is collected from analysis of incoming parts and materials, tests during manufacture and warranty returns. Afterwards, the collected data is treated by the adequate probability distribution. The following sections describe the three probability distributions typically used (Weibull, Exponential and Lognormal).

**2.3.1 Statistical Mathematical Methods**

The reason to apply statistical methods to the reliability of a component is to infer properties of a large population from a small sample of data. A continuous distribution is characterized by having any value and a discrete distribution when it has a specific value. The selection of the type of distribution will characterize the sample under study, meaning the test can be time determined (time can pertain to any variable, such as age, number of cycles, distance travelled or any other measurement between  $-\infty$  and  $+\infty$ ) or failure determined. Furthermore, if there are more than one failure mechanism occurring in a component, there may be different distributions for the different mechanisms of failure [42–46].

The Normal (or Gaussion) distribution is used to assess product and/or material properties and measurement errors. There is no time dependence and it is applied whenever a random variable is affected by a sum of random effects, so that any factor dominates. Examples are lives of treads of tires or cutting edges of machine tools, where the probability occurring before and after the mean time is equal. Binomial distribution is accounted for situations where there are only two possible outcomes (success or failure). The probability mass function gives the probability of how many successes are obtained in

several attempts. Binomial expansion may have interest in cases where products have different success and failure probabilities [44].

The decision of the correct statistical distribution depends on several factors, such as component properties, application, and environment. For example, exponential distribution is found to fit to analyse data of RF oscillators or PCBs and Weibull statistical distribution is applied on analysing fatigue failures. Weibull, exponential and lognormal distributions are used to analyse failure data to predict future behaviour of a component or system. Concerning the failure analysis of data of electronic equipment, the statistical distributions relevant are: Weibull, lognormal and Exponential distributions. For that reason, the main focus will retain over these distributions along this document [43, 45].

**Weibull distribution:**

Weibull is a two parameter distribution that has been applied for life distributions of a lot of engineering products, material strength and warranty analysis. It applies to a wide variety of hazard rates: decreasing failure rates, typical early failures and increasing failure rates (wear-out regime) [43]. This distribution is characterized by the expressions represented in Table 2.4:

Probability Density Function(PDF)	$f(t) = \left\{ \frac{\beta}{\eta} \left( \frac{t}{\eta} \right)^{\beta-1} \exp \left[ - \left( \frac{t}{\eta} \right)^{\beta} \right] \right\}$ (2.4)
Cumulative Distribution Function (CDF)	$F(t) = 1 - \exp \left[ - \left( \frac{t}{\eta} \right)^{\beta} \right]$ (2.5)
Reliability Function	$R(t) = \exp \left[ - \left( \frac{t}{\eta} \right)^{\beta} \right]$ (2.6)
Failure rate	$\lambda(t) = \frac{\beta}{\eta} \left( \frac{t}{\eta} \right)^{\beta-1}$ (2.7)
MTTF	$MTTF = \eta \cdot \Gamma(1 + 1/\beta)$ (2.8)

Table 2.4: Expressions that characterize the Weibull distribution [47, 48].

The 2 parameters  $(\beta, \eta)$  characterize the Weibull distribution. The scale parameter  $(\eta)$  and the shape parameter  $(\beta)$  determine the shape of the curve, the reliability and hazard rate. The shape parameter can assume the following values:

- $\beta = 1$ : Failure data could consider an exponential distribution where hazard rate is constant;
- $\beta > 1$  Means that the hazard rate is increasing, representing the wear-out failure mechanisms on the bathtub (Figure 2.5);
- $0 < \beta < 1$  Hazard rate is decreasing as a function of time and it represents early life failures;
- For the specific case where  $\beta = 2$ , a Rayleigh distribution is present and it represents corrosion failures (not used to characterize reliability of electronic products) [45].

In cases where failure data is not abundant, some difficulties may arise to plot it. Consequently, F(t) function is obtained by ranking the exact failures. As a first approximation, considering the sample



size is  $n$ ,  $F(t)$  is obtained dividing  $1/n, 2/n, 3/n$ , etc [43]. Apart of the previous one, the recommended expression 2.9 is used to obtain  $F(t)$  values.

$$F(t) = \frac{i - 0.3}{n + 0.4} \quad (2.9)$$

where  $i = 1, 2, 3, 4 \dots$  Failed component and  $n$  is the total number of components tested [45].

The median rank values  $F(t)$  are obtained by a Bernard approximation and it is demanded that the total items analysed are tested until each of them fail. According to the literature, there is a discrepancy on the minimum number of samples that shall be tested. According to [46] a minimum of 7 points/samples are necessary to obtain a Weibull plot, but at [45] a minimum of 10 samples are required.

The CDF can be transformed in a linear equation of the type  $y = mx + b$ , as demonstrated by equation 2.10.

$$\ln \ln \left( \frac{1}{1 - F(t)} \right) = \beta \ln(t) - \beta \ln(\eta) \quad (2.10)$$

The variable  $t$ , which is plotted in an ascending order as  $\ln(t)$ , represents the values of the x-axis which represents the variable under study (cycles to failure). The y-axis represents  $\ln \ln \left( \frac{1}{1 - F(t)} \right)$  and the slope corresponds to the shape parameter  $\beta$ . The parameter  $\eta$  can be calculated according to  $\eta = e^{b/\beta}$ .

Comparing Weibull to the lognormal distribution, Weibull provides a better fit to short time failures while lognormal is effective in longer lifetimes. Weibull is applied based on the weakest link theory and examples of application are dielectric breakdown, capacitor failures and fracture ceramics [43].

### **Lognormal distribution:**

The lognormal distribution, similar to Weibull distribution, is used for electrical components where wear-out hazard functions do not rise monotonically, but can also be applied to early failures and steady state regimes. A linearization of the reliability function (a logarithm applied on both sides repeatedly) results in data that is plotted as ordered times to failure in the x-axis and an estimate of reliability on the y-axis. Before that, there is [43, 44]. The expressions shown in Table 2.5 characterize the lognormal distribution.

The two parameters that define the lognormal distribution are  $\mu$  and  $\sigma$ . The parameter  $\mu$  represents the median time (50 % of the distribution will fail) and  $\sigma$  influences the shape of CDF and PDF. Larger values of  $\sigma$  (for  $\sigma > 2$ ), reflect high failure rates that decrease with time and for values in the order of 1 or less the failure rate remains constant and indicates the product is a candidate for high-reliability applications [43]. Although, similarly to the Weibull plot, the estimation of those two parameters are obtained by linearization according to expression 2.18.

Probability Density Function (PDF)	$f(t) = \left[ \frac{1}{t\sigma(2\pi)^{1/2}} \exp\left(-\frac{[\ln(t)-\ln(\mu)]^2}{2\sigma^2}\right) \right]$ (2.11)
Cumulative Distribution Function (CDF)	$F(t) = \Phi\left[\sigma^{-1}\ln\left(\frac{t}{\mu}\right)\right]$ (2.12)
Reliability Function	$R(t) = 1 - \Phi\left[\sigma^{-1}\ln\left(\frac{t}{\mu}\right)\right]$ (2.13)
Failure Rate	$\lambda(t) = \frac{\frac{1}{t\sigma(2\pi)^{1/2}} \exp\left(-\frac{[\ln(t)-\ln(\mu)]^2}{2\sigma^2}\right)}{1 - \Phi\left[\sigma^{-1}\ln\left(\frac{t}{\mu}\right)\right]}$ (2.14)
MTTF ( $\mu$ )	$\mu = e^{\mu' + \frac{1}{2}\sigma'^2}$ (2.15)
$\Phi(z)$	$\Phi(z) = \frac{1}{2} \left[ 1 + \text{Erf}\left(z/2^{1/2}\right) \right]$ (2.16)
Erf ( $z$ )	$\text{Erf}(z) = 2 \frac{1}{\sqrt{\pi}} \int_0^z e^{-t^2} dt$ (2.17)

Table 2.5: Expressions that characterize the lognormal distribution [49].

$$\ln(t) = \mu + \sigma\Phi^{-1}F(t) \quad (2.18)$$

where a straight line is obtained by plotting the  $\ln(t)$  in the y-axis and  $\Phi^{-1}F(t)$  in the x-axis. From the plot, the slope corresponds to  $\sigma$  and  $\mu$  is the value that corresponds to a probability  $F(t) = 0.5$ .

The  $F(t)$  values are obtained according to equation 2.9 and  $\Phi^{-1}F(t)$  corresponds to the values of  $z$  correspondent to the probability of the rank values  $F(t)$  (taking probability as an argument and returning the corresponding  $z$  value) [49–51].

Lognormal has the same application field of Weibull, used to model fatigue failure data. Examples of application are for strengths of metals and dimensions of structural elements, or biological parameters like loads on bone joints [43].

### Exponential distribution:

The exponential distribution is a particular case of the Weibull distribution, where the scale parameter  $\beta$  is equal to 1. Used as a first approach to characterize the electrical components, it models time between independent events that occur at a constant rate. It has the advantage of varying either the time or number of devices tested, meaning that if 100,000 units are required for testing, 10 units can be tested with 10,000 hours or 1000 units can be tested for 100 hours [42].

Probability Density Function (PDF)	$f(t) = \lambda e^{-\lambda t}$ (2.19)
Cumulative Distribution Function (CDF)	$F(t) = 1 - e^{-\lambda t}$ (2.20)
Reliability Function	$R(t) = e^{-\lambda t}$ (2.21)
Failure rate	$\lambda$ (2.22)
MTTF	$\text{MTTF} = 1/\lambda$ (2.23)

Table 2.6: Expressions that characterize the exponential distribution [47].

The expressions presented in Table 2.6 characterize the exponential distribution. Equivalently to Weibull and lognormal distributions, exponential distribution can also be plotted. An exponential probability plot is obtained by applying a logarithmic to the y-axis  $1/[1-F(t)]$ , where  $F(t)$  are the rank values calculated by equation 2.9 [50, 52]. The following expression 2.24 is obtained.

$$\ln\left(\frac{1}{1-F(t)}\right) = \lambda t \quad (2.24)$$

where  $\ln\left(\frac{1}{1-F(t)}\right)$  represents the y-axis and  $t$  the x-axis.

In case that the data is consistent with an exponential distribution, the resultant points create a straight line where the slope is  $\lambda$  (failure rate) and it passes through the origin. Usually, this distribution is applied to describe the distribution of failure times of complex equipment or loading pattern for some structural members. As well as the Weibull distribution, the failure data should be at least 10 components [45].

### 2.3.2 Physics of Failure

The basis of reliability theory is a statistical analysis as described in the previous Section 2.3.1. Whereas, another important element of the reliability assessment is the failure analysis, where the main goal is to identify the failure mechanisms of a component and predict the influence of those on stress and technological factors. Accordingly, reliability study involves not only the reliability statistics but also the reliability physics. The Physics of Failure (PoF) characteristics are to define a failure mode, failure site and failure mechanism. Firstly, an investigation is done to identify all critical failure mechanisms, followed by where and when they occur and its effect on the usage of the product. A PoF analysis can give a time variation, the failure speed, the shape of the survival function and what statistical distribution is associated resulting in a better understanding on the ways components fail and how they develop in time [42–44].

A failure mode analysis (FMA) is an investigation carried out to determine the failure causes which involve different types of testing, such as structural and chemical characterization and electrical testing. The general failure mechanisms can be mechanical, electrical and thermal. The corresponding material failure mechanism include fatigue, creep, metal migration, corrosion, wear, buckling, fracture or a combination of the previous ones. For example, for a component that has gone through some life cycle testing after a failure analysis, if a crack is identified, the SEM tool (explained in Section 5.2) enables the characterization of the crack, meaning that the fractured surface gives information on past information. In case there is a presence of progression marks (striations), fatigue is identified as the failure mechanisms. After the failure mechanism is identified, the correspondent statistical distribution model is applied [42, 44].

Reliability predictions are made based on models. The fatigue tests, as previously said are associated to Lognormal and Weibull distributions, which have a constant amplitude stress, characterized by a mean stress and a stress range [44]. The use of mechanical or electrical simulations, using the FEM,

are an alternative way to study the reliability of a component. There are an immensity of models that characterize fatigue. The family of S-N (where S is stress and N is the number of cycles to failure) or Wöhler curves are used to express the fatigue strength of a material and it represents the High Cycle to Failure (HCF) region of the Coffin-Manson plot where the fatigue damage is due to little plastic deformation. Fatigue tests are performed using specific material specimens in order to obtain the S-N curve for a specific alloy under study. The fatigue limit represented in Figure 2.6 is considered as the fatigue damage occurring under constant amplitude loading. The cyclic loading induces a micro crack that will nucleate inside the grain of the material. The micro crack can turn into a macro crack if the grain barrier is overcome.

The fatigue limit is the stage that represents the minimum stress amplitude to overcome the crack growth barrier. This fatigue limit is not common to all materials. For example, aluminium alloys do not have a fatigue limit. Therefore, fatigue testing is performed to a specific number of cycles ( $N_F = 10^6$ ) where the non failure stress amplitude is represented by endurance limit ( $S_E$ ). Although, factors like temperature, corrosion or periodic overload may influence the fatigue limit. There are methods, such as the Miner rule and Miner-Hailbach that allow to determine the slopes for the HCF stage [53, 54]. Figure 2.6 shows the stages of a S-N curve.

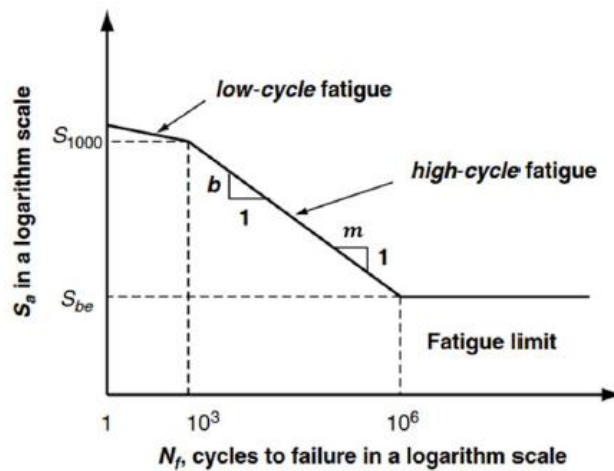


Figure 2.6: Generic S-N curve showing the different stages for a logarithmic scale [55].

The accelerated testing is another important area of the reliability testing and it involves accelerated conditions of load, stress, temperature, voltage and others that are more severe than in a normal operating level, to induce a failure in a short period and to simulate the behaviour of the component in other conditions. The usual accelerating tests are categorized in thermal stresses (temperature and temperature cycling), chemical stresses (humidity, acid or salt and other corrosives), electrical stresses (voltage, current and power) and mechanical stresses (strain cycles, stress cycles and vibration loading). The accelerated testing can be the application of one of the previous factors or a combination of them. For example, if a corrosion study is required an application of temperature and humidity is applied. An extrapolation of the results is difficult due to the uncertainties of the failure models and material properties.

There is an acceleration factor (ratio of life under normal conditions to that under accelerated condition or ratio of degradation) related with the failure models. Examples of some models are the Arrhenius model (based only in temperature stressing) and Eyring model that takes into account stresses, where based on a Nernst-Einstein allows the prediction of times to failure [43, 44].

In conclusion, reliability testing works as a process cycle, meaning that the failure analysis allows that a process change, eliminate or extend a product defect. This results, in a quality control important not only to obtain a proper design but also a control of life-cycle logistics and lower cost assessments. The manufacture of prototypes is usually aligned to the reliability testing.

### 2.3.3 Reliability of Coaxial Connectors

As referred in Chapter 1, the main function of a connector is to carry current or voltage (electrical connection) between two points, maintaining a mechanical connection easy to detach. The reliability of a connector is related with the degradation mechanisms and with the requirements it must have (range of signal distortion). The loss of the contact area, result in an increase of the contact resistance and in this section a literature review is presented to estimate the connector reliability accordingly to the corresponding degradation mechanism [56–58].

In [59], the reliability of coaxial connectors is studied based in the incorporation of silicon ( $SiO_2$ ) particles where a Weibull distribution and a maximum likelihood estimation is applied to simulate how the concentration of dust particles in the environment influences the contact failure of coaxial connectors. An exponential change was registered for particles below 1  $\mu m$  diameter. The failure of a connector is directly related with the variation of contact resistance, so changes in direct current (DC) for different particles concentration are obtained. In this case, an inverse power model was adopted as an accelerated test, where a relationship between concentration stress and characteristic life is established. This paper only considers the concentration stress factor, so the temperature or particle size are not considered.

In [60], a metallurgical investigation and a statistical analysis was done to comprehend how the contact resistance is affected and predict the life of connectors by applying an accelerated life test. There was a slight increase in the contact resistance before and after mating, which is explained by the cleaning effect during mating. Before mating, the increase of contact resistance proves that there is a presence of oxides. After mating, DC is measured and is lower because a “new” surface is created each mating cycle. The distribution used is exponential and the life stress relation follows the Arrhenius model. SEM confirmed the presence of corrosion deposits on the contact surface.

In [61], PoF and an ACT is proposed to assess connector reliability. The acceleration factors selected to study connector reliability are random vibration and current stress. The random vibration is the parameter that influence connector fretting corrosion. A two parameter Weibull distribution with maximum

likelihood estimation is applied to characterize the degradation of induced contact resistance. A distribution of contact resistance is obtained for three different levels of random vibration stresses. The possible degradation mechanisms are: wear, corrosion and stress relaxation. The first two were related with the contact finish, but the stress relaxation was related with design and materials. SEM shows that after an accelerated test, an amount of copper oxide is present on the surface and an EDS analysis reveal Zn and Ni that are elements of the base copper alloy and plating of the electrical contact.

In [62], contrary to the previous papers that focused on DC applications, it studies how the propagation of high-frequency signals is influenced with minimal loss and distortion. A series of measurements was done using a VNA to test impedance values, VSWR and insertion loss. The effect on performance of high frequency signal transmissions will vary as the contact surface degrades due to the pollution induced corrosion. Connectors were tested using nitric acid vapour to simulate a corrosion environment. The acid attack was only implemented in the pin. The S-parameters are measured between 100 KHz and 3 GHz. It is known that that the VSWR and insertion loss are affected by contact geometry and material parameters. The effect of a connector failure will alter the signal waveform. The results shown that VSWR increased as contact interface of connector degrades, which is related with the film resistance created by oxidation, and the insertion loss increased. A SEM analysis confirmed that the corroded surfaces increase the surface roughness over time. The presence of these contaminants decrease the effective contact area and so the associated current path will change. A necessity of more work between the contact aging and the consequence in electrical performance is required in this paper.

Reference [63] presents a variation of the insertion loss for different mating cycles for GPC-14, GPC-7, type N and SMA connectors to analyse how the deterioration influenced the repeatability. The total number of cycles was 10,000 cycles and the measurements were done with intervals of 2,500 cycles. The selected frequency range was 2 to 18 GHz. After the test, a standard deviation of less than 0.0082 dB of insertion loss was not exceeded for the different frequency values. The main reason for this variations are related with the stresses and strains introduced when 2 misaligned surfaces are subjected to forcibly align. An alternate alloy, temper and finish for the male pin would maximize its reliability.

Throughout this section, a lot of information is gathered from the literature related with coaxial connectors. Although there are limitations in a reliability study performed to the 1.85 mm blind mating connector. Firstly, the majority of the scientific background of coaxial connectors is for DC applications and the ones found for higher frequencies are limited to a maximum of 18 GHz. Consequently, any of the presented reliability models cannot be directly applied, because the range of frequencies of interest along this connector under study is up to 70 GHz. As explained before, the ATE system requires a fast mechanical connection so a blind mated connection is necessary. For this reason, the design limitations of the connector is another adversity, because the only available ones are for threaded connectors. Therefore, this project addresses a new area because it applies a reliability study for coaxial blind mating connectors used for a range of frequencies between 7 MHz and 70 GHz.

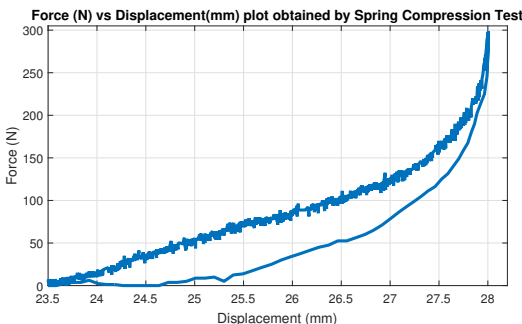
# Chapter 3

## Testing setup

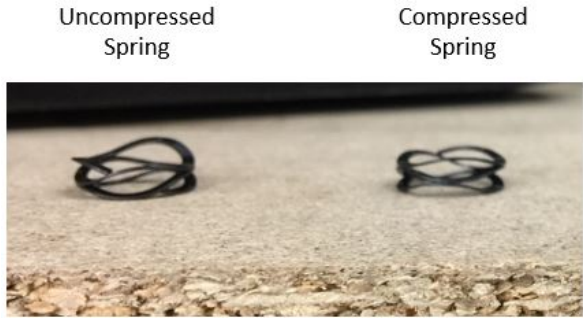
This chapter explains the conditions and equipment used for testing a 1.85 mm blind mating coaxial connector. Before measuring the results, several preparation steps were required including the automation of a testing setup.

### 3.1 Testing Conditions

In order to properly test the coaxial connector, first the number of connectors and the number of cycles (docking cycles) need to be defined. On the literature review, there are limited information on these parameters, so before the tests were performed on the brand new connectors, tests were made on used connectors to have an idea of how many cycles would be a reasonable number. Nonetheless, some unexpected failures were registered earlier, due to a spring failure (Figure 3.1 presents a compression test performed to the spring where the maximum force is 300N or 67 lbf) caused by a over compression of the connector blind mating spring which led to severe wear.



(a) Spring compression test plot.



(b) Spring before and after compression test.

Figure 3.1: Hysteresis curve of spring compression test (top curve represents the compression and bottom curve the uncompression).

Experimentation on other used connectors using a trial error approach, led to conclusion that the waiting time (cycle time) between each docking cycle has to be higher than 15 seconds. Figure 3.2 represents the interior connector degradation for different waiting times for the same number of cycles

(10,000 cycles).

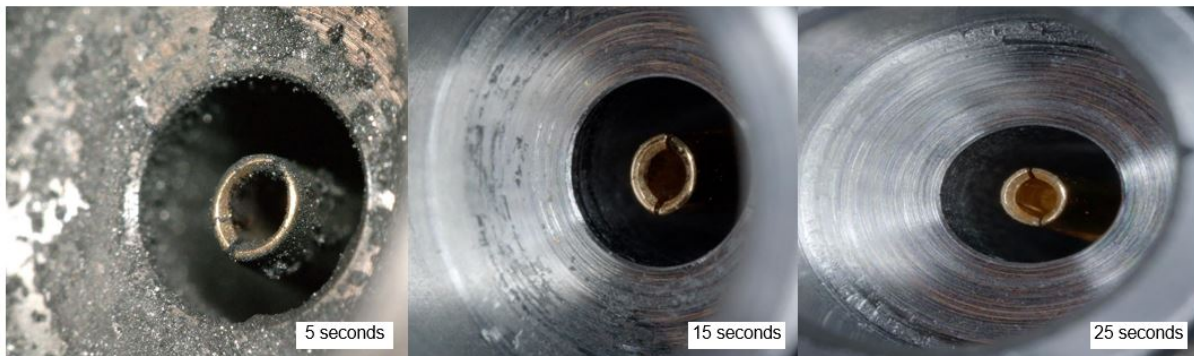


Figure 3.2: Differences of wear in the interior of female connector for different waiting times<sup>1</sup>.

The chosen number of cycles was a compromise between the available time to obtain the results for this project and what is expected to be the lifetime of the ATE system at the customer (assuming 5 insertions per day, 60,000 cycles correspond to a connector lifetime of at least 10 years). After that, conditions were gathered to define the final testing conditions applied to the brand new connectors:

- 60,000 cycles for 12 connectors and 30,000 cycles for 2 separate connectors (these connectors were subjected to an accelerated test before being placed in the ATE system) were performed;
- A total of 14 connectors were tested. The justification for this number can be explained by two separate reasons. On the first hand, the number of connectors cannot be large due to the high cost associated with each connector and the limited test resources, since only two connector pairs can be tested in parallel. On the other hand, the statistical distributions addressed in Section 2.3.1 demand that a minimum number of 10 connectors are tested. This allows to infer a statistical value to a bigger population (the goal is to infer a statistical value for 64 connectors, that correspond to the maximum number of connectors that are inside the ATE system);
  - From the 14 connectors, 10 are used to measure electrical performance through S-parameters;
  - 2 connectors are used to measure the electrical contact resistance;
  - 2 connectors to measure the electrical performance (S-parameters) after being subjected to an environment of 85 °C and 85 % humidity during 72 hours (accelerated testing) according to the diagram obtained in Figure 3.3. The standard that defines this test is JESD22 - 101. The choice of this standard is supported by the fact that it is a common test performed to coaxial connectors used in industrial aerospace applications, representing one of the most severe HAST tests of this industry.

<sup>1</sup>The waiting time is the time considered while the connector is disconnected (not docked) and the spring is uncompressed.



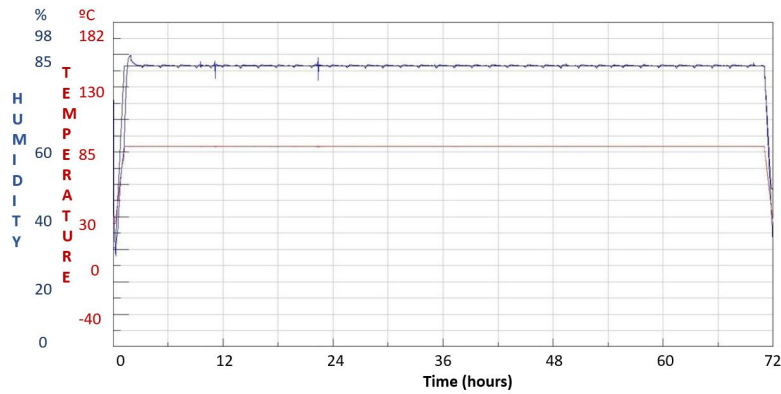


Figure 3.3: Diagram of temperature and humidity obtained from the ClimeEvent [64] for connector number 11 and 12 (connectors subjected to ACT before cyclic testing).

The used 4-Port VNA [65], only enables that 2 connectors are tested at the same time. So, as can be seen in Figure 3.4, only two connectors are placed for testing inside the ATE system and stiffner. The female part of the connector is screwed into the female bracket, which is then fixed in the stiffner and the male part of the connector is attached to the male bracket which is then fixed into the ATE system interface to the DUT test fixture. This step is also described in Figure 3.4:

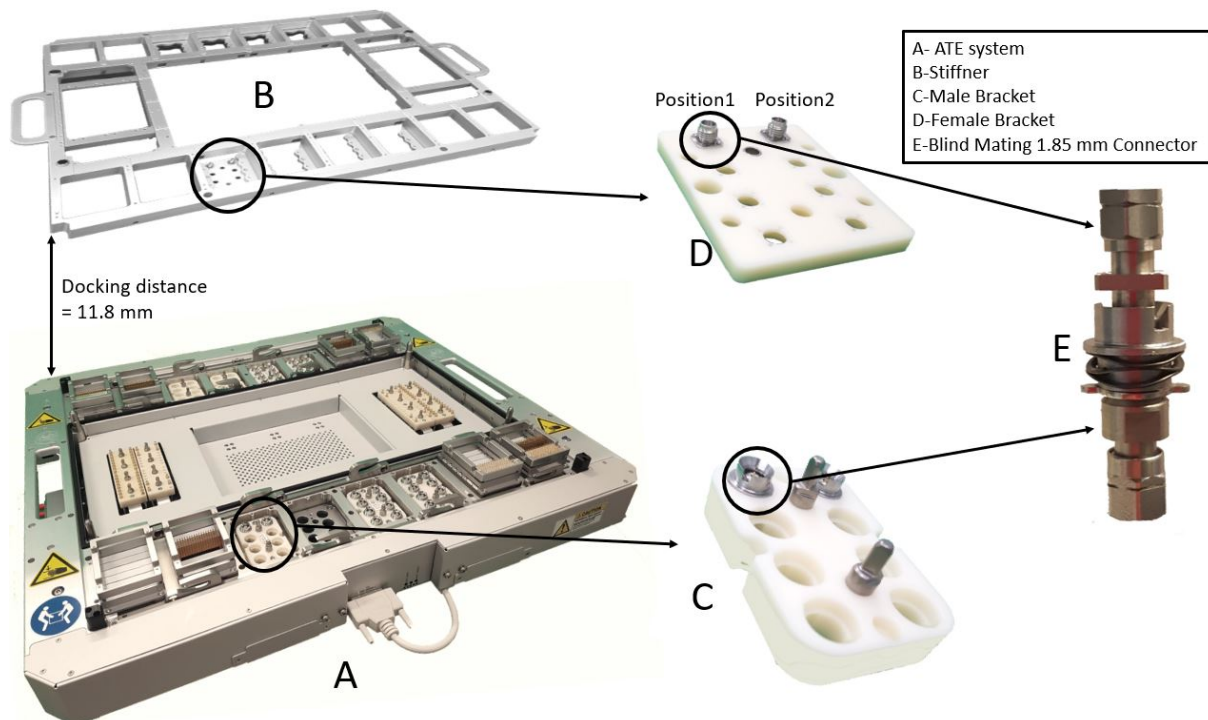


Figure 3.4: Diagram showing the integration of the 1.85mm blind mating interconnect into the brackets that are assembled in the DUT test fixture stiffener and ATE system.

For every two connectors the following steps are considered:

1. Scattering parameters are extracted from the VNA every 300 cycles. This choice was a compromise between the observation of the connector performance evolution and test time. Naturally, the

ideal option would be to extract the S-parameters every cycle, but that would result in an extended time of testing, which is not possible according to the available time for the realization of this thesis;

2. Every 6,000 cycles, the connectors are removed from the brackets (Figure 3.4 represented by letter C and D) and setup, for the following measurements to be performed:

(a) Mechanical measurements including the withdrawal and insertion forces occurring at the socket. The main goal is to obtain a plot of the influence of these forces with the increasing number of docking cycles. The description of how these forces are obtained are explained in Section 3.2. Figure 3.5 demonstrates the plots obtained for the insertion and withdrawal forces of a brand new connector before testing, where the circumferences determine the values obtained (maximum value for insertion force and minimum for the withdrawal force);

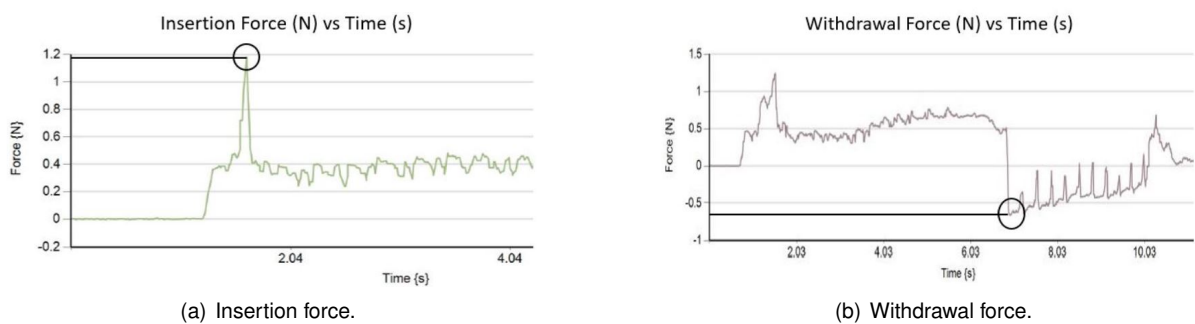


Figure 3.5: Resultant plots of forces obtained by a Chatillon Force Gauge [66] for a new connector.

(b) In the case of the dimensional measurements, two different types of measurements are done:

i. Measure the concentricity of the pin by finding the center of the outside circumference and inner circumference and calculating the distance between those two points and do the same for the socket as shown in Figure 3.6 (the only difference is that the inner surface is an ellipse instead of a circumference). The Fiji software was used [67], where the result is automatically obtained by attributing a certain number of pixels to  $\mu m$  according to the blue scale (300  $\mu m$ ) on the right bottom corner represented in Figure 3.6;



Figure 3.6: Demonstration on how concentricity is calculated.

ii. Measure pin depth distance using a pin gage from Anritsu [68] represented in Figure 3.7 by x ;

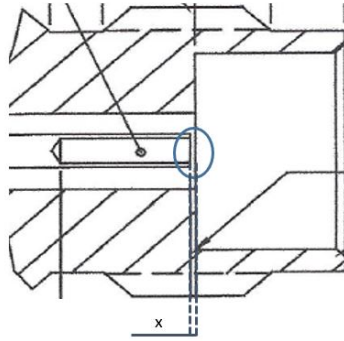


Figure 3.7: Pin depth distance according to the IEEE P287 standard [14].

(c) Lastly, a visual inspection is made to the interior of the connector using an optical microscope [69], where photos are taken of both male and female parts.

3. After, the female part of the connector in position 1 is flipped with the female part of the connector in position 2 (Figure 3.4) and the connectors are replaced back into the ATE system. This step is done every 6,000 cycles and after doing the measurements explained in point 2. The goal of this step is to replicate what occurs in a real situation at the customer, where it might occur that different DUT test fixtures are docked to different ATE systems;
4. Repeat the same steps than in 1, 2 and 3 every 6,000 cycles until the 60,000 cycles;
5. Do the previous instructions to the rest of 8 connectors.

For the 4 remaining connectors (2 connectors for DC and 2 connectors for accelerated testing), the test is completed according to the same steps explained from 1-4. The only difference for connectors 13 and 14, is that in point 1, instead of measuring the S-parameters, DC measurements are instead performed using a multimeter [70] and in the case of connectors 11 and 12, they are subjected to only 30,000 cycles instead of 60,000 due to time limitations. The total testing time for the 14 connectors, considering all the assumptions, should not be longer than 2300 hours, which corresponded to a total of 3 months to obtain all the results. This value is only considering the testing of connectors in the setup. In addition, there was the time to take all the measurements between every 6,000 cycles which is dependent on each connector and user.

For such a high number of cycles, it is expected that the remaining setup (ATE system, brackets and cables) get damaged. Therefore, every 6,000 cycles the results collected are compared to the previous ones and if any failure is registered, the root causes for the failure must be analysed. In case that a failure is induced by a setup problem, the parts damaged have to be immediately replaced by new ones before running the next 6,000 cycles. The following Figure 3.8 summarizes the reliability test plan.

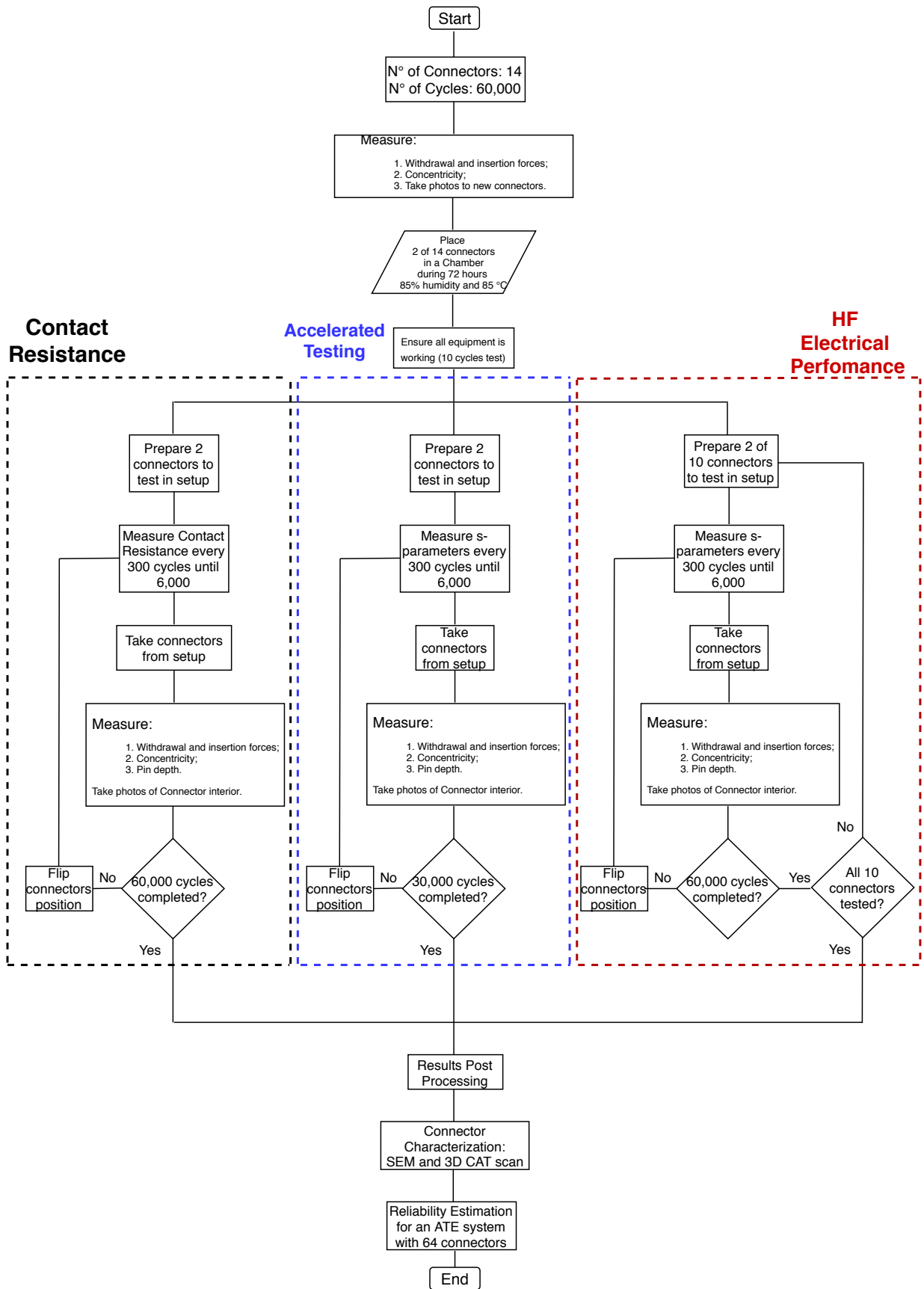


Figure 3.8: High-level block diagram of the reliability test plan for the 14 connectors.

One important point to note is the calibration of the VNA. Usually, it is important to calibrate the VNA to the end of the measurement cables so that it is able to accurately measure any item attached to the measurement cables. In the case of the interconnect studied in this thesis, since it is a very small component with low loss, its measurement with a VNA is very challenging. Also the cable movements, temperature drifts, among others will make the calibration no longer valid requiring a re-calibration. In addition, there is always the danger of the calibration masking a problem in the measurement setup.

On account of the reliability study, the focus was on how the connector performance varies with the number of cycles, so the decision was to use the VNA without any calibration. Despite this, since measurement cables loss is not removed from the measurements, there is no need to worry about the need to re-calibrate the setup or when the calibration is no longer valid. The only point of interest is the difference between measurements at different points on the testing cycle. Factors like cable movement still have an impact on the measurement results but the minimization of that movement is not possible. Instead, cables with high-performance and best phase stability with movement commercially available were used.

## 3.2 Setup Implementation

The necessary equipment for the connector reliability tests, can be separated into equipment used while testing (connectors cyclic testing) and equipment used to obtain the different mechanical and dimensional measurements(connectors outside setup).

### **Matlab**

Matlab is the software used for two different tasks: for the implementation of an automated setup where the docking and undocking of the system is controlled by the user and for processing the results from the VNA (extracted as touchstone format .s2p files) and from the multimeter (extracted as ascii .txt files). Before testing, the code in matlab was developed, so that, the number of cycles, cycle time, frequency range and regularity of saving the S-parameters is selected by the user. For the case of the contact resistance, the results obtained are a function of the resistance with the number of cycles. The manipulation of .s2p files allows that a specific scattering parameter (S11,S12,S21 or S22) can be chosen and displayed as a reliability or performance basis. This results in plots, where deviation between first and last cycle or between consecutive cycles can be shown as the number of cycles increase. This allows the easy identification of a failure.

### **Measurements Setup**

The only equipment used before testing was the ClimeEvent chamber to induce 2 connectors into an accelerated testing. The setup is controlled by a computer connected to the instruments through GPIB. The power supply controls both dock/undock applied to the ATE system [71]. The air pressure is regulated by a pressure control valve LR-1/8-D-MINI [72] which is set to 6 Bar. When the dock is activated, the power supply sends a signal to the ATE setup that allows the entrance of air. Figure 3.9 shows the automatized setup used to obtain the S-parameters and contact resistance measurements.

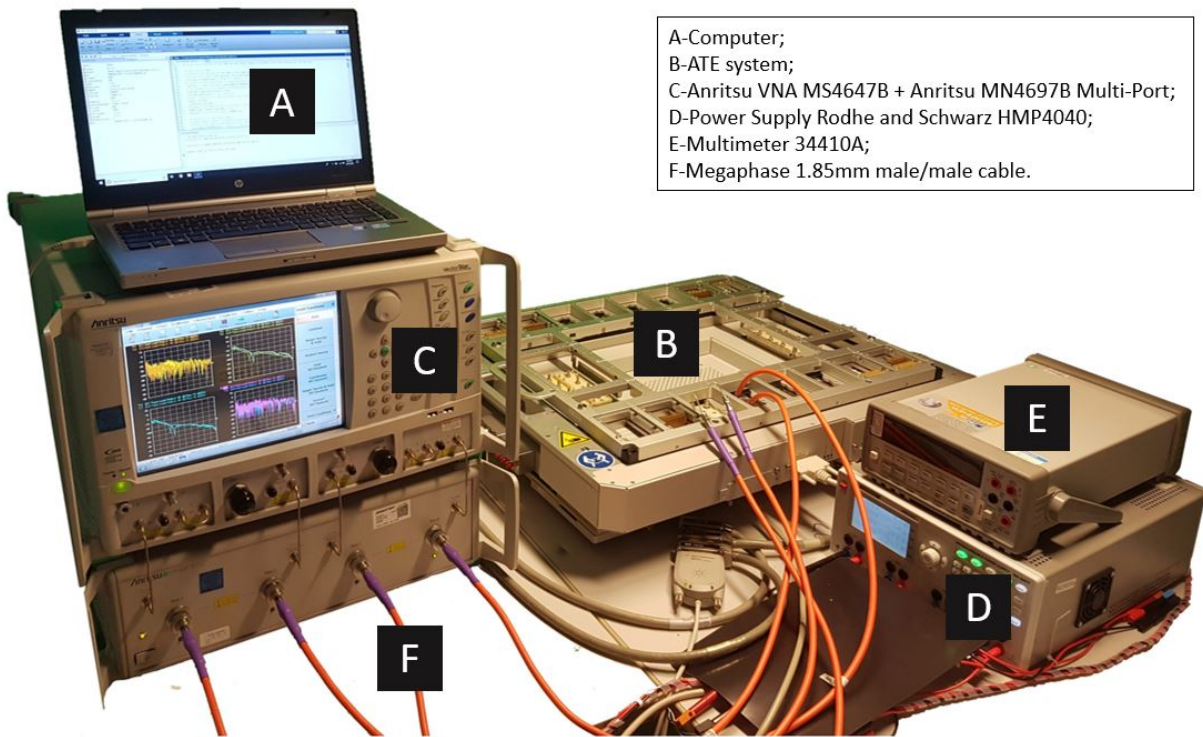


Figure 3.9: Automatized setup used to test the blind mating 1.85 mm connectors.

### Mechanical and Dimensional Measurements

For the mechanical measurements, the equipment used to obtain the withdrawal and insertion forces was a Chatillon Force Gauge DFS2-002 [66]. To take these measurements, there are no procedures in the literature that explain how to perform them. For this reason, a second setup was created as demonstrated in Figure 3.10, where a digital dial gauge, a computer and special pins are used.

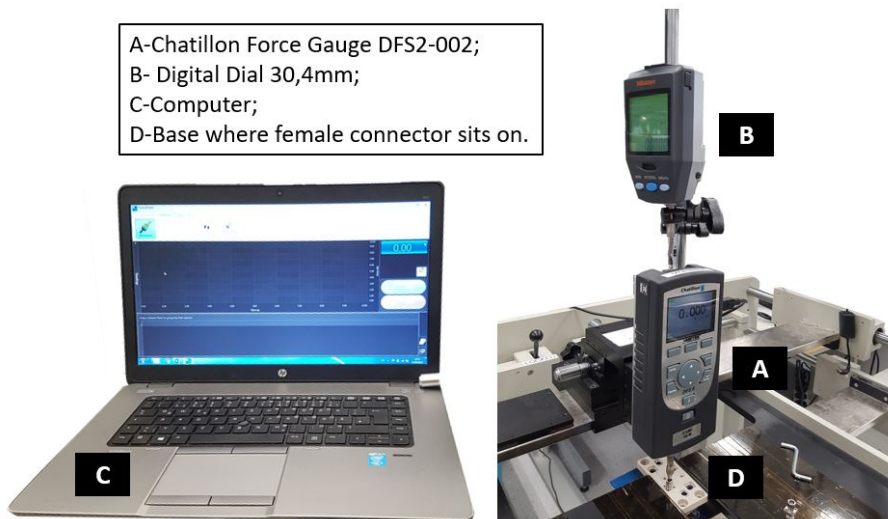


Figure 3.10: Force measurement setup to obtain the withdrawal and insertion forces.

The connector designer specifies that when the first contact between the pin and socket is established, the pin enters a distance of 1.3 mm inside the socket. Consequently, to measure the withdrawal

and insertion forces the force gauge has to go down exactly the same distance and to do that, the dial gauge is fixed on the top of the force gauge to measure the traveled distance. The computer is connected to the force gauge to obtain the measured force values. When the first contact between the socket and pin is established, the force is different from zero, so the dial gauge is set to zero. At this point the test starts and the forces are registered in the computer.

In an ideal scenario, the force gauge and the dial gauge should only have one degree of freedom along the vertical axis but that does not happen. Hence, a misalignment influences the values of force obtained. Furthermore, the pins used to attach the force gauge also play a role on the values obtained. For this test, two different pins were used represented in Figure 3.11 which are made of a tool steel and with a geometry according to the IEEE 287 standard [14]. The standard only specifies that the test must be done at the same rate, but it says nothing on the procedure to measure it.

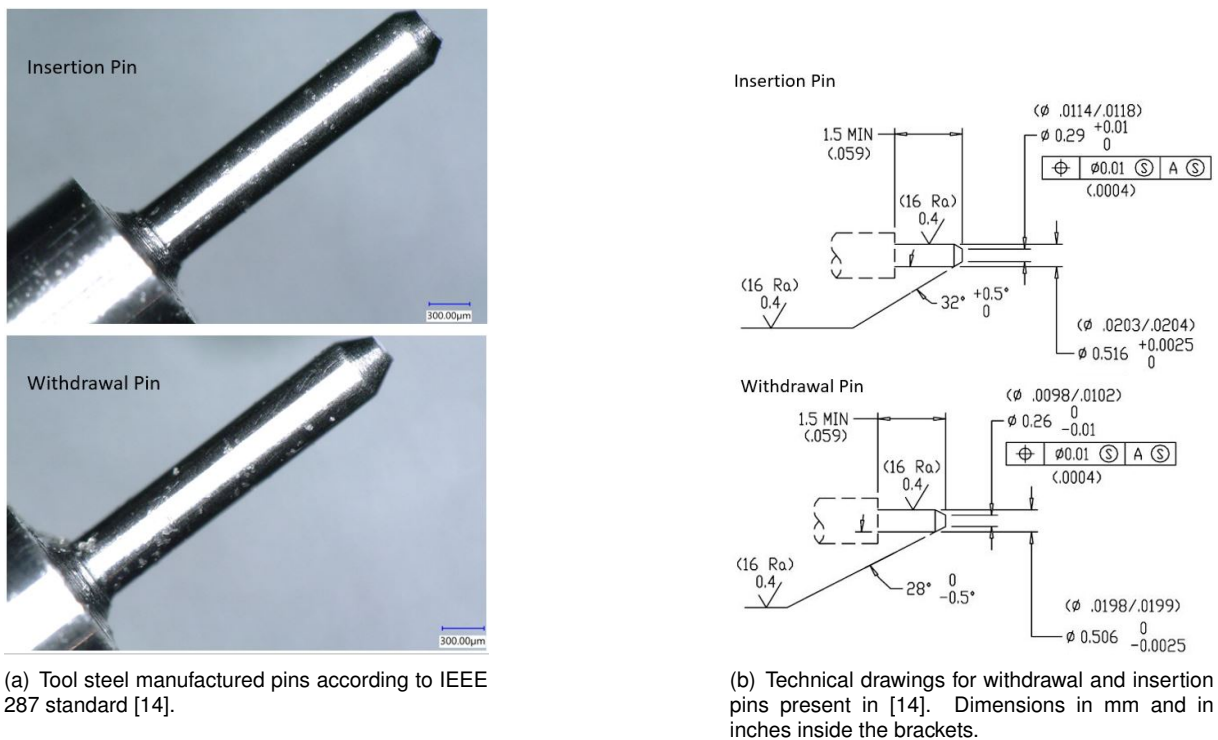


Figure 3.11: Insertion and withdrawal pins pictures and drawings.

In the case of the dimensional measurements, a pin depth gauge 01-322 included in the Anritsu V-Mechanical Calibration Kit Model 3654D/3454D-1 [68] was used to measure the pin depth with the increasing number of cycles. The digital microscope VHX-6000 [69] allows to take photos or videos which grant a visual inspection of the top view of the connector pairs. The only considerations to have while measuring the pin depth, are to make sure that the male connector is in a straight position. In the case of the microscope photos taken for the concentricity measurement, the amplification and focus area must be the same.

Figure 3.12 summarizes the equipment used, before and after testing, with detailed specifications and photos, describing the conditions applied to implement the automation of docking/undocking into the ATE system.










Equipment	Product	Conditions
Accelerated Testing	ClimeEvent C/1000/70/5 M 	<ul style="list-style-type: none"> <li>• 85% Humidity;</li> <li>• 85 degrees Celsius;</li> <li>• Time Duration: 72 hours.</li> </ul>
Measurements Setup	Anritsu VNA MS4647B plus Anritsu MN4697B Multi-Port Test Set 	Measure s-parameters without calibration. Cable connection consists of a 48 inch Megaphase 1.85mm male/male cable (rated to 70 GHz) and a RF Coax 5 inch male/female 1.85mm cable (rated to 65 GHz).
	Multimeter 34410A 	Measures contact resistance of 2 connectors using a 4-port setup.
	Power Supply HMP4040 	For undocking channel 1 – 3.3V, channel 2 – 0V and channel 3 – 24V and for docking channel 1 – 0V, channel 2 – 3.3V and channel 3 – 24V.
	Pressure Control Valve LR-1/8-D-MINI 	6 Bar are applied to the system according to Advantest specification.
Mechanical/Dimensional Measurements	Chatillon Force Gauge DFS2-002 	Special pins are used to measure withdrawal and insertion forces.
	Digital Messuhr ID-H, CEE AC-Adapter 30,4mm 	Measure the distance between reference plane and contact interface.
	Pin Depth Gauge 01-322 	Push the male connector until the end to measure pin depth.
	Digital Microscope VHX-6000 	Photos allow a visual inspection of the interior of the connectors every 6,000 cycles and the concentricity values are obtained using Fiji software.

Figure 3.12: Summary of the used equipment.



# Chapter 4

## Testing Results

This chapter presents the results obtained for the mechanical, electrical and dimensional measurements performed in the context of this thesis. Due to the large volume of measured data, only a subset of the measured results will be presented in this chapter, where some specific connectors are used to explain the results in several sections. Even so, in the appendix sections the complete results for each connector are shown for the electrical, mechanical and dimensional measurements. At the end of this chapter, the application of reliability statistical models considering only the connectors that failed are presented.

### 4.1 Electrical Measurements

#### 4.1.1 Scattering Parameters (S-parameters)

As discussed in the previous chapters, the main application of this blind mating coaxial connector, is to establish an electrical connection between the ATE measurement instruments and the DUT. The S-parameters provide a complete description of the connector electrical performance of a connector. The S-parameters were measured with a VNA without calibration, where for the measured range of frequencies (7 MHz-70 GHz) problems arise related with the cable movement, temperature variations, etc... For this reason, Figure 4.1 demonstrate what is considered a connector failure in the measured S-parameters and how it is identified. The presented S-parameters are focused only on the insertion loss ( $S_{12}$ ), assuming that  $S_{12}$  is equal to  $S_{21}$  due to the reciprocity of the connector. The plot represents an overlap of 200 lines, which correspond to the measurements done along the 60,000 cycles with intervals of 300 cycles for connector 5. In Figure 4.1 there is a resonance around 20 GHz in the measured insertion loss. This is considered as a failure since no resonance should be present in the entire frequency domain. A failure identification is done based on the repeatability of  $S_{12}$  along the number of cycles. So, in the case of  $S_{12}$ , for each value of  $S_{12}$  corresponding to each frequency point (there are 10,000 frequency points of equal step size, to allow for an harmonic sampling), the variability defined is of 2 dB which accounts to the variations of temperature, the cables folding and the VNA calculations for each measurement. In summary, if a variation of  $S_{12}$  is higher than 2 dB the connector is considered as failed. Because in this setup, the measurement cables loss is not calibrated, the return loss ( $S_{11}$ ) is not

used as a failure criteria since its values would be dominated by the measurement cable loss. One way to better observe the variation of the S-parameters is to compare the measured S-parameters during the testing process (i.e. at each 300 cycles) with the original measured S-parameters before the connector testing started. This is shown in Figure 4.2. In the figure, the first plotted line represents the difference of the measured S12 at cycle 300 with the S12 at cycle 0. The second plotted line the difference of the measured S12 at cycle 600 with the S12 at cycle 0 and so forth. The last plotted line is the difference of the measured S12 at cycle 60,000 with the S12 at cycle 0. This allows to see clearly any change on the measured S-parameters when compared with the initial measurement (before the test cycle started).

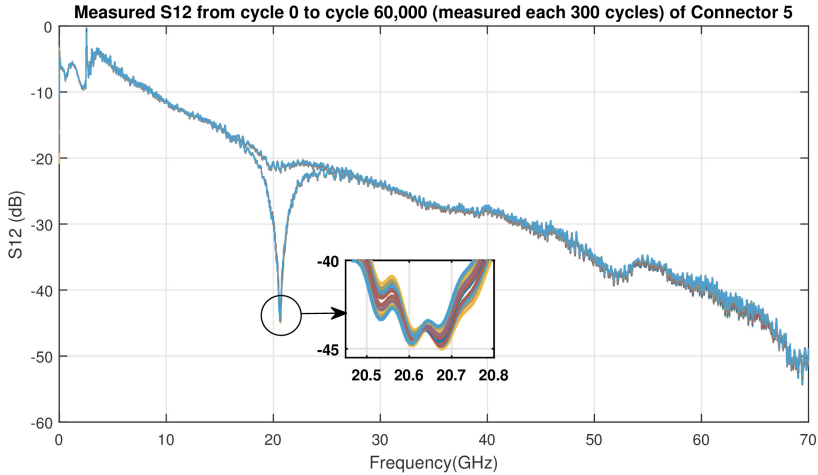


Figure 4.1: S12 measured for connector 5 in intervals of 300 cycles until 60,000 cycles.

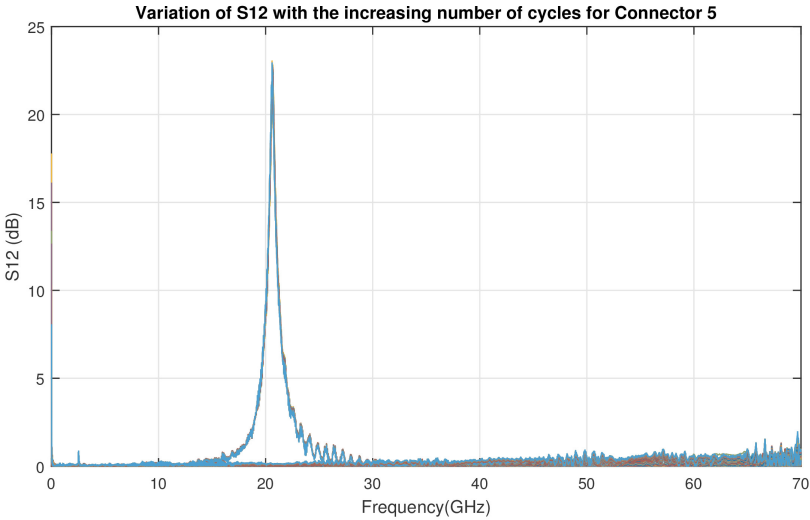


Figure 4.2: Variation of S12 for connector 5 measured every 300 cycles until 60,000 cycles.

Connector number 5, is one of the 10 connectors tested where the S-parameters were measured and it is an example of a failed connector. From the plot of S12, in Figure 4.1, there is a drop of more than 20 dB at a frequency of around 20.6 GHz. After post processing the results, the failure was identified at the cycle 54,000, although as it will be explained in Section 4.2.2, this connector failed earlier, at the cycle 48,000. When the connectors were disassembled to do a physical characterization study (Chapter 5),

the ones that presented a failure in terms of the S-parameters showed a crack in the socket as can be seen in Figure 4.3. Only one of the fingers of the socket has a crack but that is enough to increase the socket aperture. For cases where the socket is widely opened, a gap is created between the pin and the socket. This gap is responsible for the resonance observed in the S12 measurements.

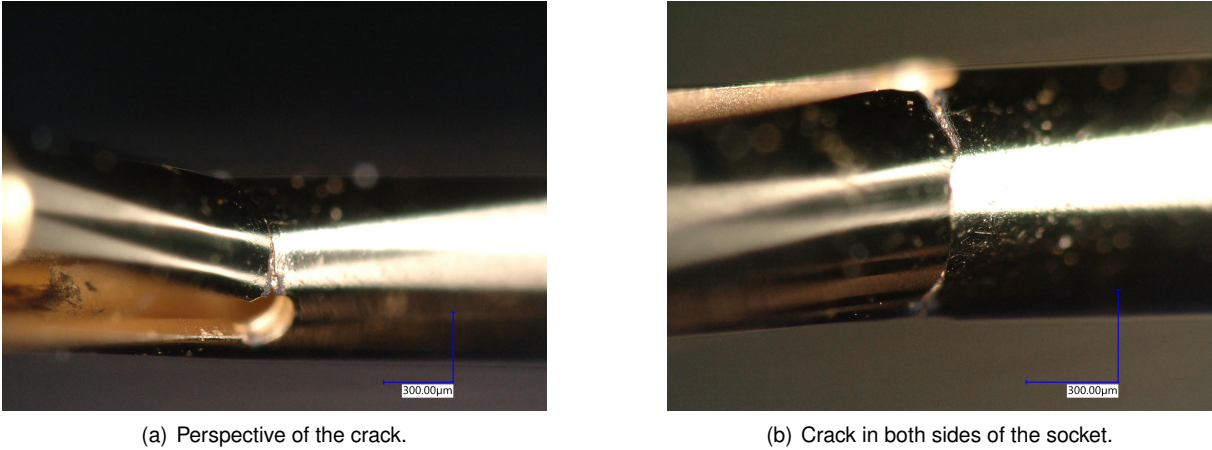


Figure 4.3: Different perspectives of the crack in connector pair 13.

Connector 11 and 12 were subjected to an accelerated test before the stress life test. Connector 12 is an example that demonstrates how a connector behaves after an ACT. Connector 12 presented an earlier failure compared to the connectors tested under normal conditions of humidity and temperature. The failure occurred at the 24,900 cycle, showing a resonance in the frequency domain around 8 GHz. Figure 4.4 shows the variation of S12 at every 300 insertions, from 0 until 30,000 insertions and Figure 4.5 shows a 3D plot of the variation of S12 over the number of insertions but only for the range between 24,900 and 30,000 insertions.

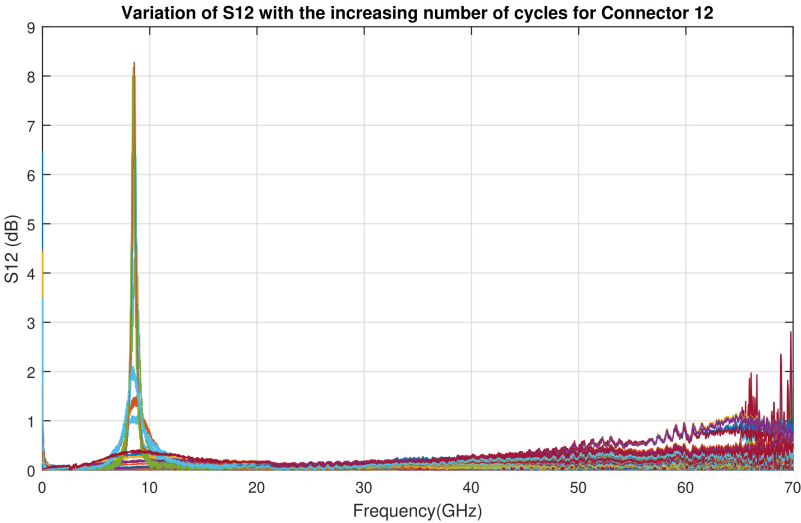


Figure 4.4: Variation of S12 for connector 12 measured every 300 cycles until 60,000 cycles.

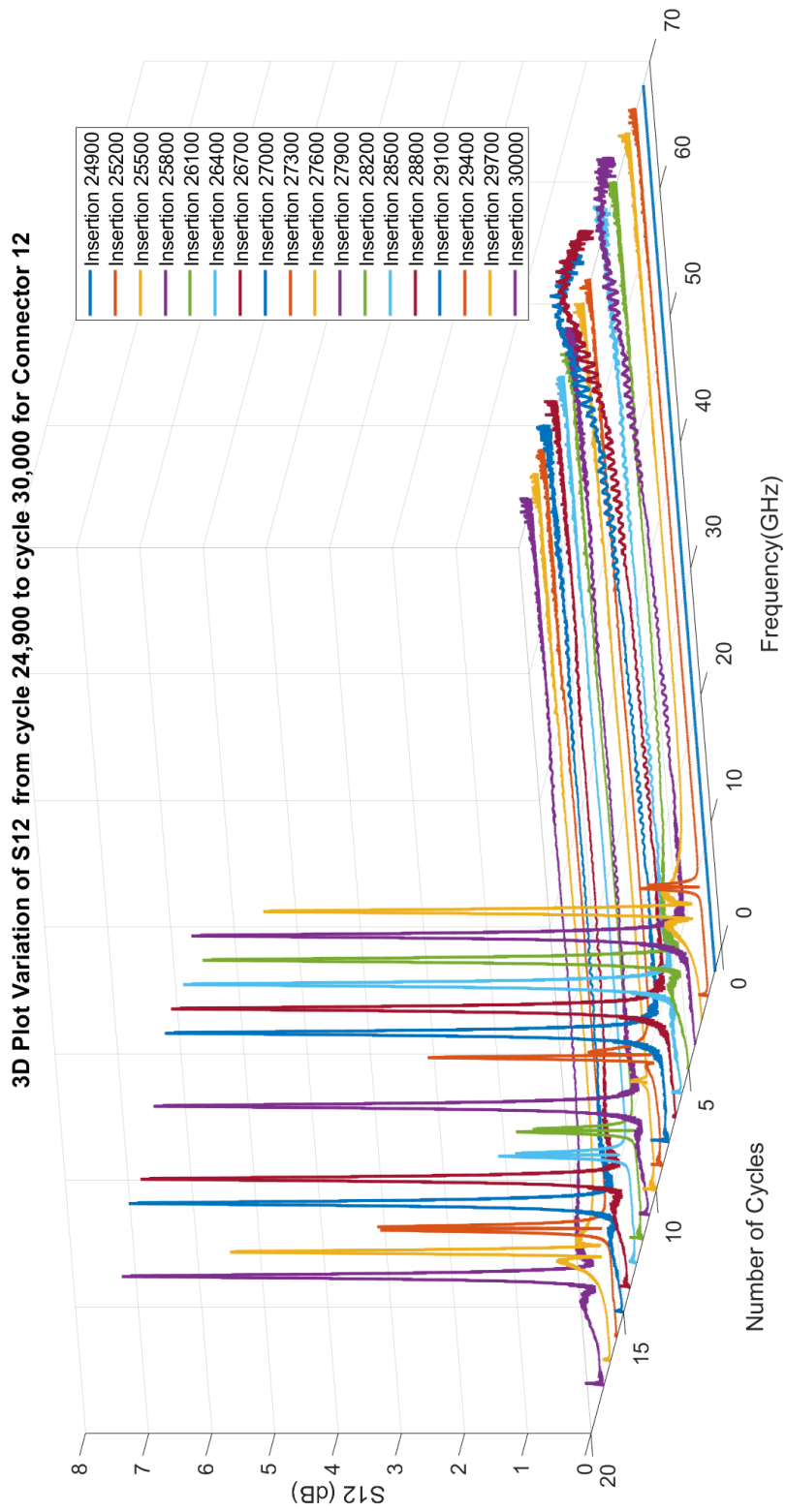


Figure 4.5: 3D plot that demonstrate the variation of S12 for the different number of cycles.

Figure 4.5 shows an intermittent failure phenomena. This means that, for example at the 25,500 cycle there is a difference of 8 dB compared to cycle 25,200 and in the 28,200 cycle the difference is lower than 2 dB. Consequently, according to the threshold defined previously, this connector would represent a failure at the 25,200 cycle and no failure at the 28,200 cycle. Even though, the first failure defines directly the cycle value that the connector as failed. In this case, this connector should be immediately replaced at the 25,200 cycle. The reasons why this intermittent failure occurred are explained in Section 4.2.

The earlier failure registered for connector 12, allowed to infer that the ACT influences the lifetime of the connector. Consequently, applications that require higher temperatures and humidity levels result in a lower reliability (around 25,000 cycles). The reasons for an earlier failure compared to the other connectors are addressed in the following sections. Connector 11, another connector subjected to an ACT before testing, presented no failure for the 30,000 cycles as can be seen in Figure D.6.

### Electrical Performance

In order to characterize the connectors in terms of absolute performance, the S-parameters were measured before and after testing with calibration using a 70 GHz 2-Port VNA setup with shorter measurement cables. The results are focused on the S12 parameter. Figure 4.6 and 4.7 show the performance for two different connectors, namely connector 8 and connector 11. The blue line represents the Anritsu calibration kit reference 1.85 mm female to female adapter, which is used as a comparison reference for any 1.85 mm connector performance.

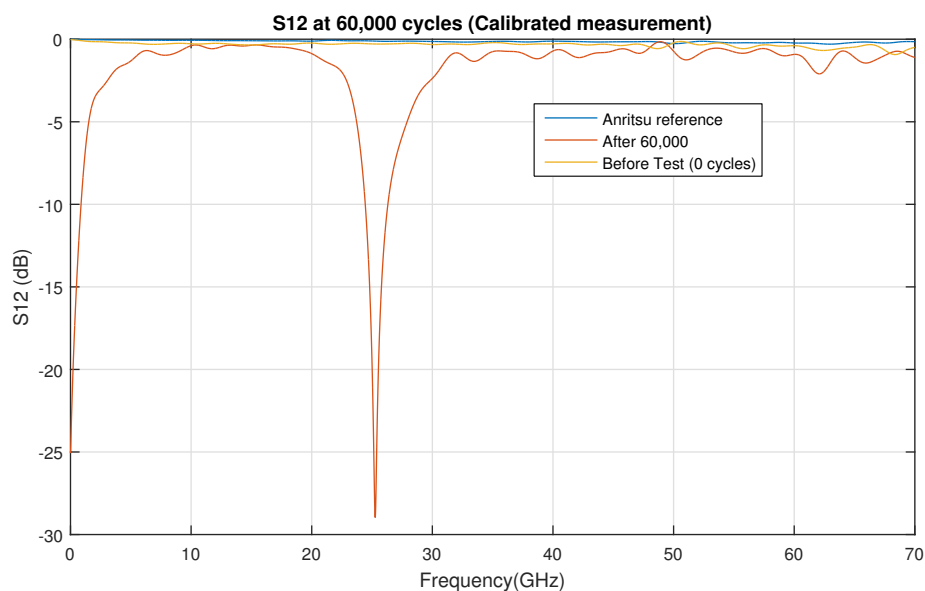


Figure 4.6: Measured S12 performance of connector 8.

In Figure 4.6, connector 8 shows two resonances in the working frequency band of the connector with one of them at a very low frequency which could even mean that there is no direct current con-

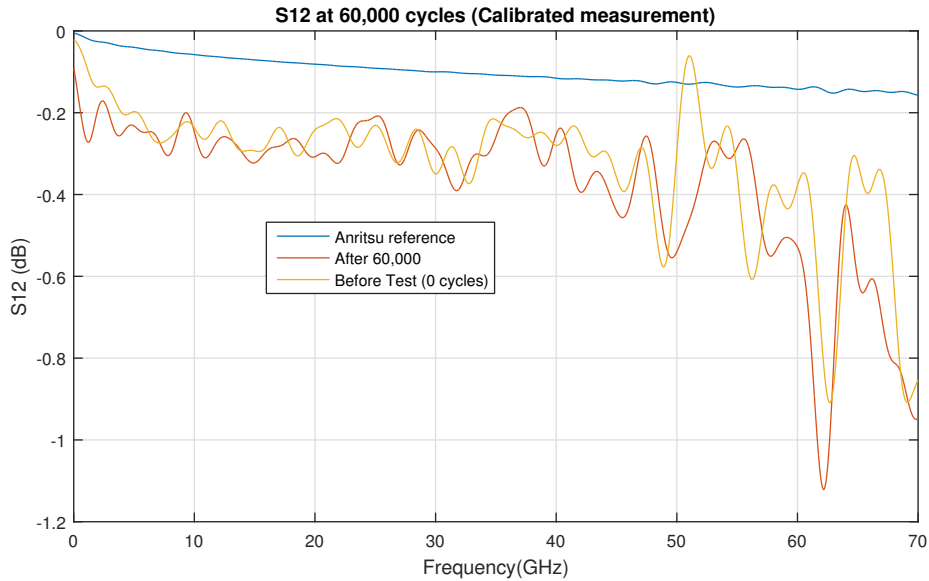


Figure 4.7: Measured S12 performance of connector 11.

nection, i.e. no physical contact between the pin and socket. The frequency value of the resonance peak will be somehow related to the mechanical deformation inside the connector that generated the resonant behavior for that frequency. To properly analyze the causes of the resonance it would require to understand first the mechanical deformation and then perform an electromagnetic simulation using a finite elements approach. This was outside the objectives of this thesis. This is because from a connector failure point of view it does not matter at what frequency the resonant behavior appears, it only matters that it exists.

For connector 11, the resultant performance after 30,000 cycles remains practically the same as shown in Figure 4.7. The red line follows practically the same behaviour than the yellow line which proves that the performance was not degraded by the high number of cycles. Around 63 GHz occurs the highest variation (around 0.2 dB) between the two lines.

#### 4.1.2 Contact Resistance

As described before, this connector is intended for 5G/WiGig applications where the behaviour at frequencies bellow 24 GHz or at DC has no consequences. In order to study the application of this connector in another areas (like high-speed digital applications), contact resistance measurements were also done for 2 connectors (connector 13 and 14). The results for the contact resistance as a function of the number of cycles are shown in Figure 4.8 and 4.9.

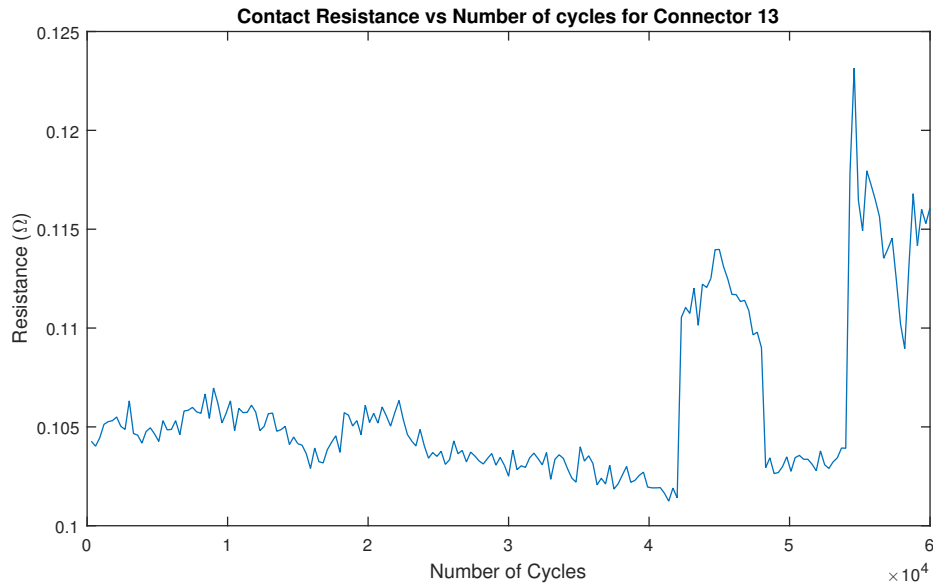


Figure 4.8: Contact resistance versus number of cycles for connector 13.

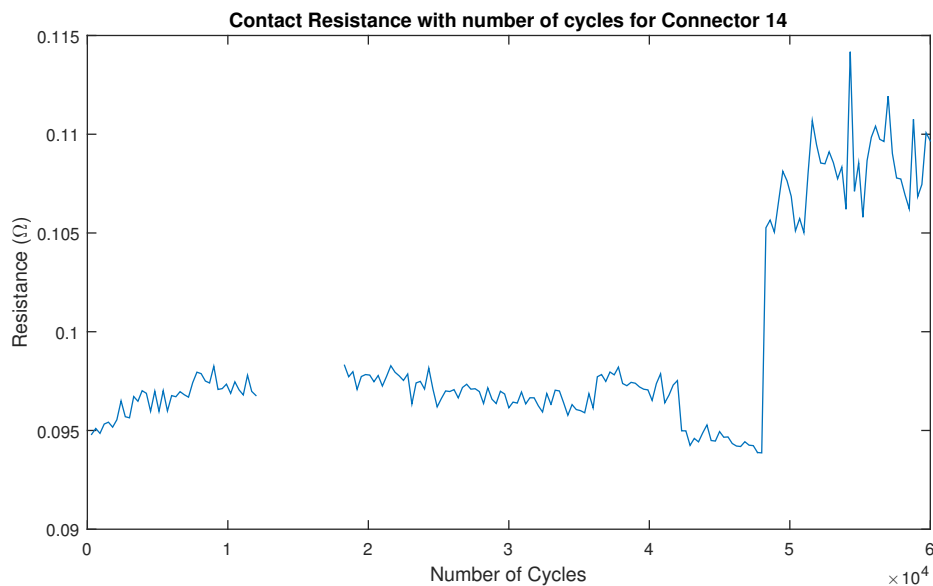


Figure 4.9: Contact resistance versus number of cycles for connector 14<sup>1</sup>.

The contact resistance is directly related with the area of contact between the socket and the pin. With the increasing number of cycles, the wear between the surfaces influences the area of contact. This area of contact is created by the points of contact, which are normally called as asperities or a-spots. There are two phenomena that should be taken in account. First, the number of asperities decrease with the number of insertions (decrease in the measured contact resistance value). On the other hand, the area of contact increase because the gold particles from the plating are being dragged down to the same position each docking cycle due to the wear action, which in turn increases the area of contact.

<sup>1</sup>No measured contact resistance between 12,000 and 18,000 cycles since the measurement cables were not properly threaded.

The small variations on the contact resistance until 42,000 cycles are related not only to the physics of the contact described in the last paragraph, but also due to the measurement accuracy of the multimeter and the flipping of female connectors 13 and 14 (area of contact is different for female pairs of connector 13 and 14) every 6,000 cycles. The values of contact resistance before failure are around 0.105 mΩ. This value is below what IEEE 287 defines for the 1.85 mm threaded connector [14]. The main justification for this difference is related with the gold used, the finishing of the surface after plating and the specific design of the measured 1.85 mm connector.

The exponential increase in the contact resistance for the 42,000 insertion, is confirmed by the failure of the connector. Even though, between 42,000 and 48,000 cycles, the female pair of the connector corresponds to connector 14, so this increase in contact resistance and consequently failure, is not directly related to connector 13.

In Figure 4.8, for the same range of cycles, there is not a considerable variation on contact resistance, so the female pair of connector 13 shows no failure. For the next 6,000 insertions (between 48,000 and 54,000 cycles), connector 13 present lower values of contact resistance, which proves that until the 54,000 cycle, the female pair of connector 13 did not have a failure. On the last 6,000 cycles, both connectors show values in the order of 0.110 mΩ, so after 54,000 cycles both connectors are considered as failed.

In the case of a failure, similarly to the S-parameters, the contact resistance values are higher because the contact of the male and the socket is only established by one finger of the socket. So, that creates a gap between the other finger and the pin. Once the contact is established in only one finger, the area of contact decreases which results in an increase of the contact resistance.

## **4.2 Mechanical and Dimensional Measurements**

This section separates the mechanical measurements into insertion and withdrawal forces and the dimensional measurements into concentricity and pin depth.

### **4.2.1 Withdrawal and Insertion Forces**

These forces were measured to determine how the physics of contact between the socket and pin is influenced along the cycles. Due to time limitations, the forces measured until the 12,000 cycle for connector 5 and 13 were measured using pins which were not manufactured in accordance to the IEEE 287 standard. That is the reason why in Figure 4.10 and 4.11, there is an increase, in its absolute value, between the 6,000 and 12,000 cycle for both withdrawal and insertion forces. The measurements of connector 12 were all made using the new correct pins, hence there is a linear decrease for both forces.



Every point on the plots is an average value of 5 measurements done for each force.

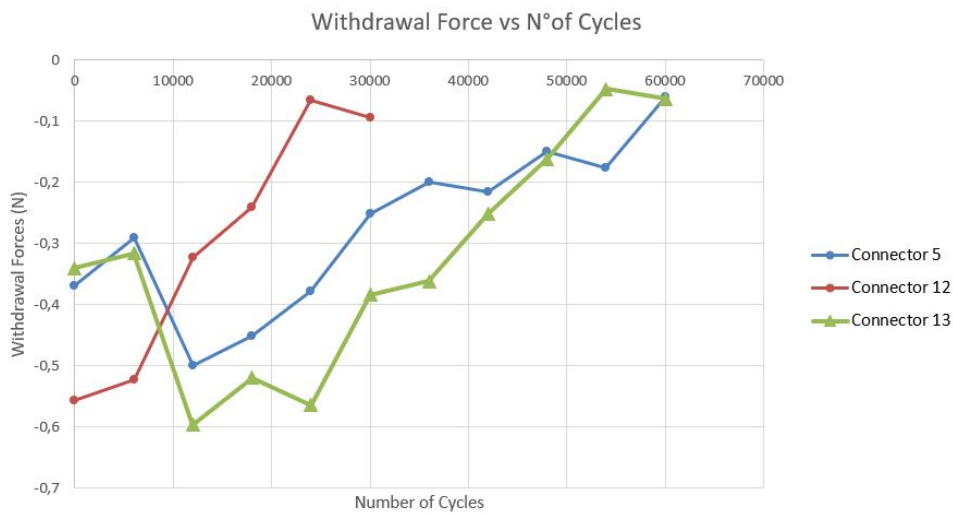


Figure 4.10: Withdrawal forces of connectors 5, 12 and 13, at different number of cycles.

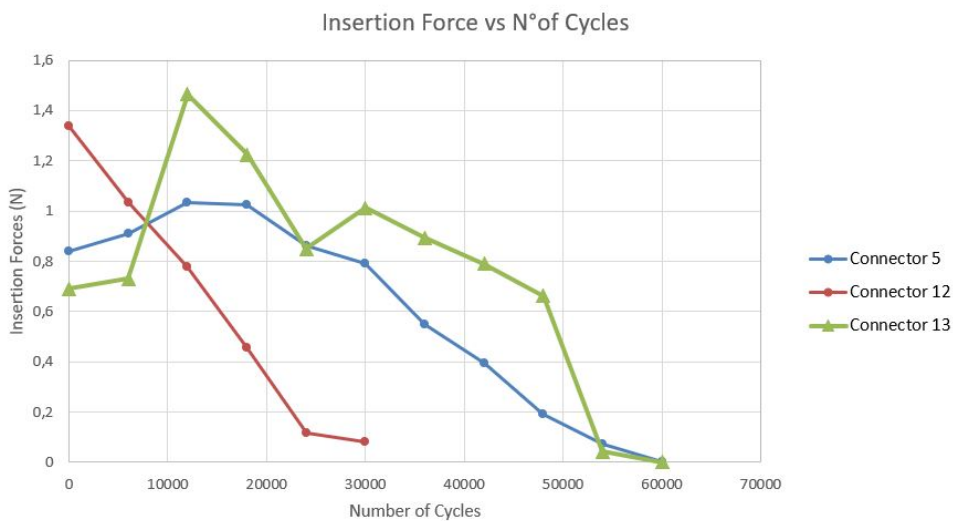


Figure 4.11: Insertion forces of connector 5, 12 and 13 at different number of cycles.

IEEE P287 defines a maximum insertion force of 0.9 N and the minimum withdrawal force is 0.14 N [14]. The insertion and withdrawal forces obtained at 12,000 insertions, are above the values found in the literature. The discrepancy of these values cannot be directly compared because the values defined in IEEE P287 are for threaded connectors. The IEEE 287 standard gives no information regarding the design or manufacturing of the sockets. Also, the measurement instrumentation is not the same. Furthermore, the socket closure process of the tines obtained during heat treatment and manufacturing processes is an important factor that directly affects the values of insertion force. Consequently, each manufacture has its socket own design and manufacturing methodology which directly influences the values of force.

For connector 13, the insertion force is 0.85 N and the withdrawal force is 0.56 N after 24,000 cycles.

At 30,000 cycles, the insertion force is 1.01 N and at 18,000 cycles the withdrawal force is 0.52 N. It was expected that both insertion and withdrawal forces decrease with the number of cycles. The reason why in this range it did not, might be related with the measurement instruments setup. Since the alignment between the socket and the pins is manually done by the user, the value obtained for the forces vary and there is always an associated error.

There is a correlation between the S-parameters and the values of the withdrawal and insertion forces. At the 54,000 cycle, connectors 5 and 13 present withdrawal and insertion forces close to zero which correlates with the failure registered in the measured S-parameters. For these connectors the failure was caused by the measurement instruments used to collect the insertion and withdrawal forces and not by the life stress (docking/undocking) itself. That is why the majority of connectors fail at specific cycle transitions (point where the mechanical measurements are performed every 6,000 cycles).

Even though the failure occurred due to the mechanical measurements while the connectors were out of the ATE system, it is still considered as a failure. There are no assurances the connectors were close to fail. Assuming a situation where the mechanical measurements were not performed, the failure phenomenon could be studied by performing a SEM analysis or a CT scan every 6,000 insertions. Even so, the occurrence of this failure confirms that the socket closure increases, so the socket loses elasticity with the increasing number of cycles.

The previous paragraphs, allow to infer conclusions about the pins used to do the measurements. The misalignment of the pins create high stresses at the surfaces of contact. A solution to avoid that, would be to manufacture a specific component (with a same design than the male pair) where the withdrawal and insertion pins are placed inside that male and on the other side the thread was compatible with the screw of the force gauge equipment. During mating, the resultant self-alignment would reduce the high stresses resultant during measuring.

Nonetheless, the measured forces before failure may have influenced the lifetime of the connector. The reason behind the intermittent failure for connector 12 may be related with the docking depth. Figure 4.12 and 4.13 show how the resultant plot for the insertion force is affected at different number of cycles.

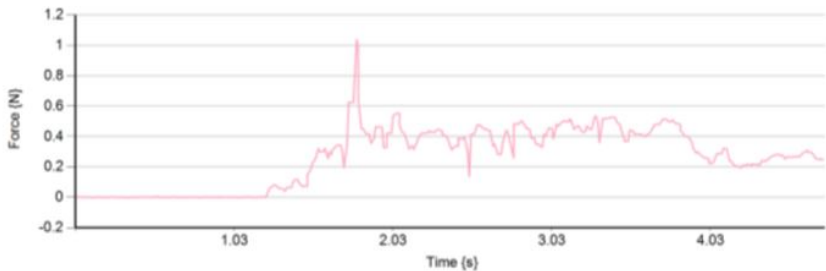


Figure 4.12: Insertion force plot of connector 12 before the first docking cycle (cycle 0).

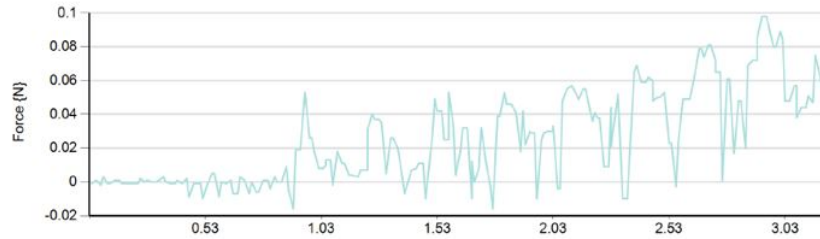


Figure 4.13: Insertion force plot of connector 12 after 24,000 cycles.

Usually, the highest force occurs at the start, which is when the first contact is made, so where the higher stresses occur (Figure 4.12). Otherwise, in Figure 4.13 the highest force occurs around 3 seconds increasing linearly until that point. The difference between the two plots is related with the socket aperture. In Figure 4.13, the socket is more open and so the contact is only established for higher docking depths. This phenomenon explains the intermittent failure. For the range of 24,900 and 30,000 cycles of connector 12, the docking travelling distance every insertion may vary and that influences the contact between the socket and the pin and then it explains the presence of a failure.

According to the 24,000 cycle where the connector was still working without any failure, a minimum value of 0.12 N for the insertion force is achieved. No conclusions can be taken from the withdrawal force for connector 12, since the value is close to zero. Albeit, by looking to the withdrawal forces of connector 5 and 13 at cycle 42,000 (immediately before failure), where both had no failure registered, a minimum of 0.2 N was measured.

## 4.2.2 Concentricity

The concentricity measurements are dimensional measurements in units of distance between the centre of two geometric shapes. Higher concentricity values are related to higher stresses during contact, which means higher insertion forces. The reason to consider this measurement as part of the test plan, is to check if the flipping of the female components every 6,000 insertions influences concentricity. This measure is not addressed in any standard. The connector manufacturer specified a maximum acceptable concentricity value of  $50 \mu\text{m}$  (0.002 inch) for both pin and socket. The photos presented in Figure 4.14 show the connector concentricity at 0, 30,000 and 60,000 cycles where a clear enlargement of the socket is observed.

As can be seen in Figure 4.15, the pin concentricity is not affected with the increasing number of cycles. The small variations are probably related with the flipping of the female every 6,000 insertions and with the error associated with measuring the centre of the surfaces using Fiji software.

Concerning Figure 4.16, the concentricity of the socket changes exponentially which means the female connector is affected in terms of concentricity. For connector 12, the concentricity of the socket is  $118 \mu\text{m}$  after 30,000 insertions. This value makes sense since the first failure was registered around the 25,000 cycle so the concentricity measurement is out of specification only after the 30,000 insertions.

Additionally, the value of concentricity for the female connector 13 is on specification before the

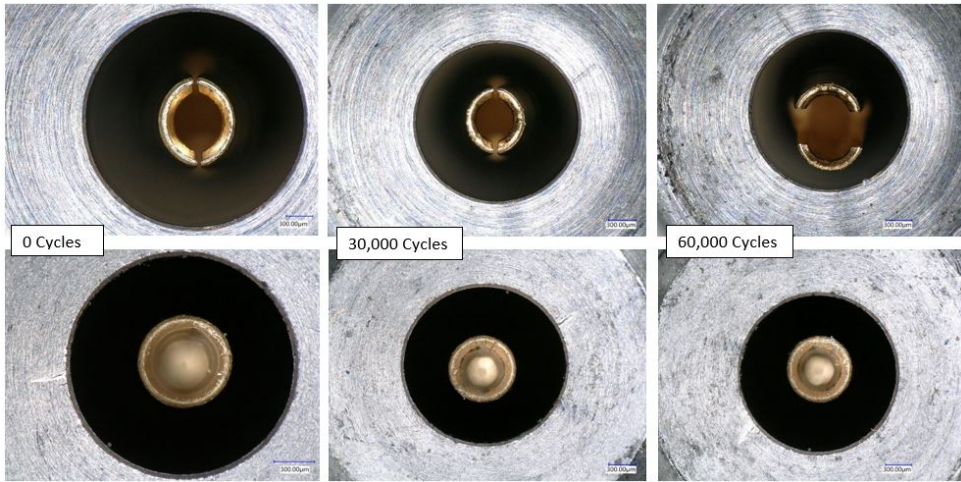


Figure 4.14: Interior picture of the connector pairs at different number of cycles.

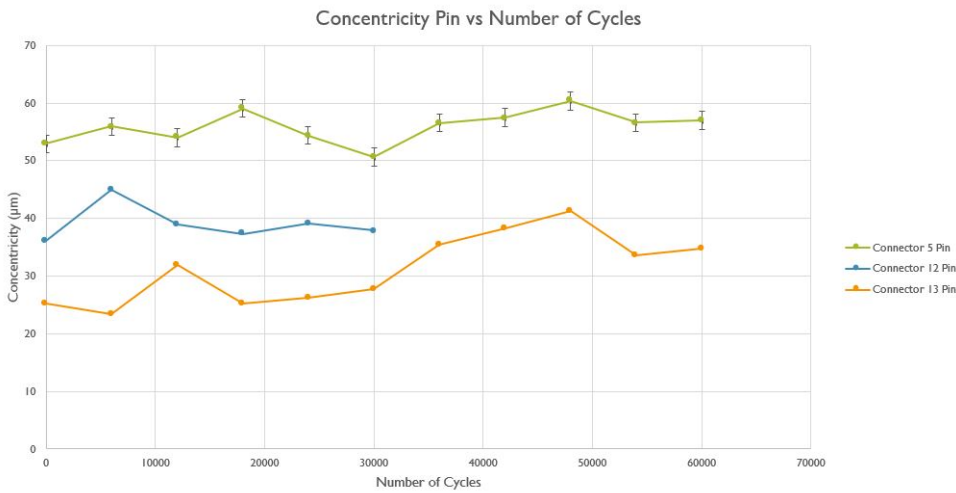


Figure 4.15: Concentricity of the pin as a function of the number of cycles for connector 5, 12 and 13.

54,000 cycle, but according to the contact resistance measurements in Figure 4.8 and to the values of forces in Figures 4.10 and 4.11, the connector has failed. Thus, this is an example why it is relevant to compare the values of the other measurements to the concentricity measurements. If one of the mechanical or dimensional measurements are out of specification, a resulting failure in the form of a resonance will be observed in the measured S-parameters.

Connector 5 was an interesting case. After 48,000 cycles, before placing the connector back in the setup to continue the test, the fingers of the socket were manually pushed back to the initial position to study how it would behave in terms of electrical parameters. According to the S-parameters of connector 5, the connector has no failure until the 54,000 cycle, although the concentricity of the socket ( $173 \mu m$  in Figure 4.16 for connector 5) is out of specification at 48,000 cycles. This suggests that, although the measured concentricity was out of specification, because probably the socket fingers have lost their elasticity, when the tines were manually pushed back to the initial position in this specific connector, no failure was registered on the S-parameter measurements for the range of 48,000 to 54,000 cycles.

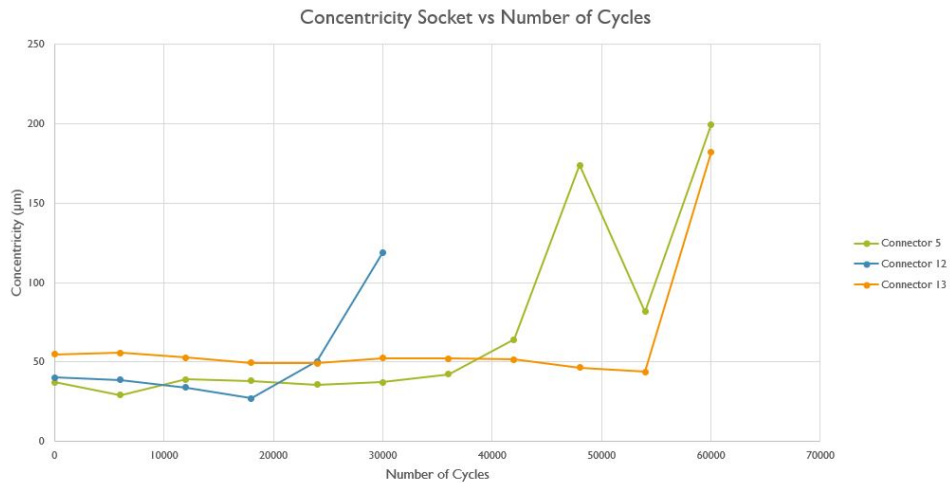


Figure 4.16: Concentricity of the socket as a function of the number of cycles for connector 5, 12 and 13.

### 4.2.3 Pin Depth

Pin depth is a dimensional measurement taken by the pin depth gauge shown in Figure 3.12. In an opposite way to the results of the previous measurements, the pin depth measurements do not define the connector reliability in terms of electrical or mechanical specifications and no correlation can be defined. This measure represents the distance of the pin relative to the surface of contact, as discussed in Section 3.7.

As the number of cycles increase, the surfaces of contact becomes more degraded and consequently the values of the pin depth change. As the surface of contact is ripped off, the pin is pushed down with the increasing number of cycles, which is translated in a recession of the pin depth. Thus, the pin depth measurement is directly related to the degradation of the surface. Figure 4.17 represents the measures of pin depth at different number of cycles for different connectors.

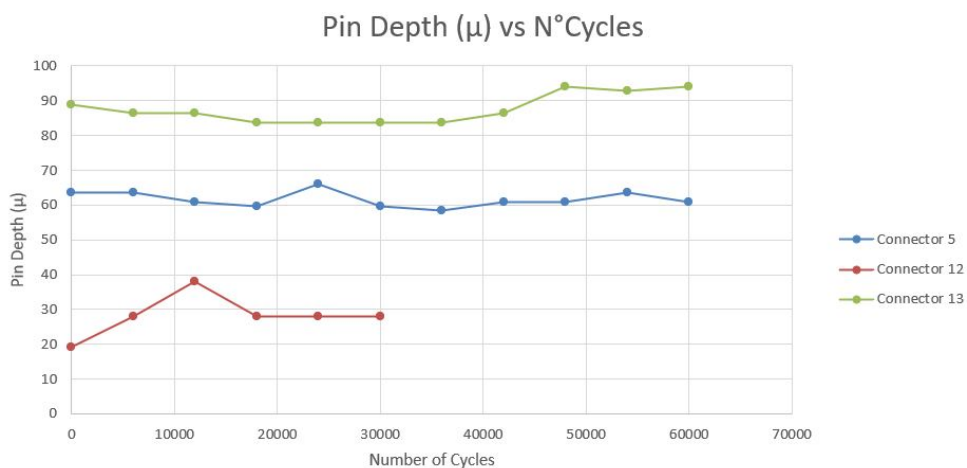


Figure 4.17: Pin depth for connector 5, 12 and 13.

The values remain practically constant for the different number of cycles for each connector, which suggests that there is not a considerable wear occurring in the surfaces of contact. Still, the values of

pin depth differ a lot for the different connectors. The reason behind that, is related with the connector design, more specifically with the position of the bead. For connector 12, the value is considerably lower compared to connector 5 and 13. That can be justified by the fact that this connector was subjected to an accelerated testing before where its action is explained in Section 5.1. Moreover, it is difficult to have a flat surface while measuring.

### 4.3 Application of Reliability Models

In this section, based on the results from the tested connectors, the Weibull, lognormal and exponential distributions are applied as reliability models, that characterize the probability before failure  $R(t)$  of a 1.85 mm blind mating coaxial connector for different cycles to failure. Table 4.1 shows the 14 connectors tested and the correspondent cycles to failure ( $t$ ). The S-parameters are the metric that define either the connector has failed or not. In the appendix D, the measured S-parameters are shown for the 12 connectors.

Connector	1	2	3	4	5	6	7	8	9	10	11 <sup>1</sup>	12 <sup>1</sup>	13	14
Cycles to Failure	-	-	42,000	30,000	48,000	54,000	45,900	45,000	36,000	30,000	-	24,900	48,000	36,000

Table 4.1: Cycles to failure for the different connectors tested along the reliability stress testing.

From Table 4.1, only connector 1, 2 and 11 have not failed for the stress cycling test. According to [46], a minimum of 7 components (tested under the same conditions) is necessary to implement a reliability model where a distribution plot is obtained based on the calculation of the rank values  $F(t)$ . Taking this into account, connector 1 and 2 cannot be considered on the reliability model, because the insertion pins used to perform the mechanical measurements each 6,000 cycles were not the same as the ones used for the remaining connectors. Connectors 11 and 12 also have to be discarded because they were subjected to an ACT before the cyclic testing. In the case of connectors 13 and 14, since the S-parameters were not measured for these connectors, the cycles to failure represented are assumed based on the dimensional and contact resistance measurements. So, connectors 13 and 14 are also not considered for the reliability model.

Apart from the different conditions during testing, conclusions cannot be made on the exact number of cycles to failure for connector 10 due to setup problems while measuring the S-parameters (frequency drops at different values of frequency, Figure D.5 in Appendix D) shows the degradation of the ATE mechanical docking system for such a high number of cycles. The cycles to failure represented in Table 4.1 for connector 10 are determined based on the concentricity measurements (that is why in Table D.1 there is no frequency of failure associated). So, this connector is also not taken into account for the application of the reliability model.

<sup>1</sup> Connectors subjected to an accelerated test before cyclic testing.

The connectors used on the reliability model are shown in Table 4.2. The goal is to linearize the CDF function and write it according to the equations correspondent for each distribution. As addressed in Section 2.3.1, the estimation of the Weibull, exponential and lognormal parameters are analytically calculated via probability plotting.

The rank values  $F(t)$  correspondent for the different cycles to failure ( $t$ ) are shown in Table 4.2. The values of the cycles to failure are expressed in an ascending order.

Connector	4	9	3	8	7	5	6
$t$	30,000	36,000	42,000	45,000	45,900	48,000	54,000
$\ln(t)$	10.31	10.49	10.65	10.71	10.73	10.78	10.9
$F(t)$	0.0946	0.2297	0.3649	0.5	0.6351	0.7703	0.9054
$\ln\left(\frac{1}{1-F(t)}\right)$	0.0993	0.2610	0.4539	0.6931	1.0082	1.4709	2.3582
$\ln\ln\left(\frac{1}{1-F(t)}\right)$	-2.3089	-1.3432	-0.7898	-0.3665	0.0082	0.3858	0.8579

Table 4.2: Connectors considered for the reliability models and the correspondent expressions used for the different distributions.

The resultant plot of the Weibull distribution considering the connectors tested is shown in Figure 4.18 (with a correlation coefficient of 98.9 %), where the y-axis represents  $\ln\ln\left(\frac{1}{1-F(t)}\right)$  and the x-axis represents  $\ln(t)$ . These variables are calculated accordingly to equation 2.9.

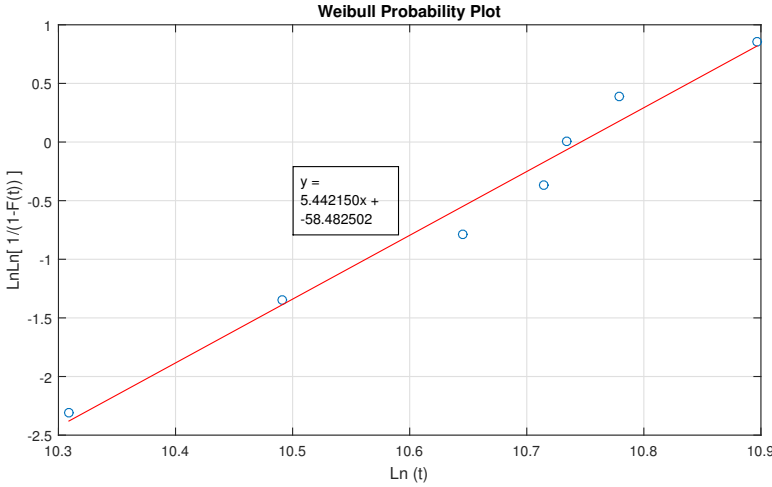


Figure 4.18: Resultant plot obtained from the linearization using the Weibull distribution.

From the equation shown in Figure 4.18, the Weibull parameters are estimated. The shape parameter ( $\beta$ ) which is the slope is 5.44 and the scale parameter ( $\eta$ ) is 46,453 cycles to failure (calculated from  $\eta = e^{b/\beta}$ ). At this point, the failure rate and MTTF (where  $\Gamma(1 + 1/\beta) = 0.923$ ) can be calculated according to the respective equations 2.7 and 2.8 shown in Table 2.4. The resultant values of these variables are shown in Table 4.3.

The variation of the reliability function demonstrated in Figure 4.19, shows the behaviour of the reliability of a 1.85 mm blind mating coaxial connector with the increasing number of cycles to failure.

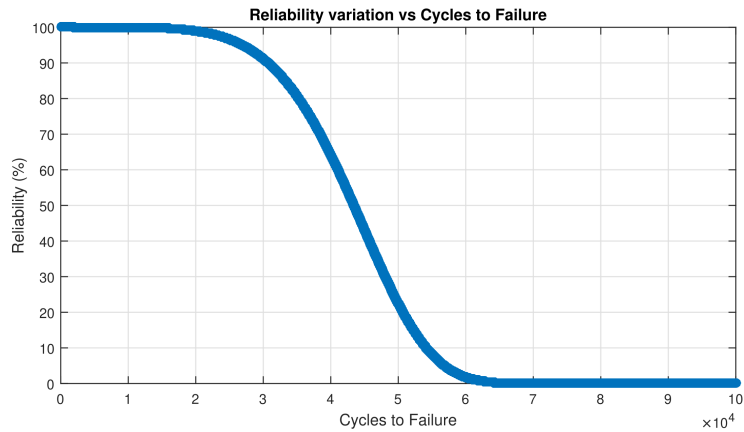


Figure 4.19: Reliability as a function of the number of cycles (until cycle 100,000) for a blind mating coaxial connector using the Weibull distribution.

As a similar approach to the Weibull distribution, according to equation 2.10 the plot shown in Figure 4.20 describes the lognormal distribution (with a correlation coefficient of 96.8 %).

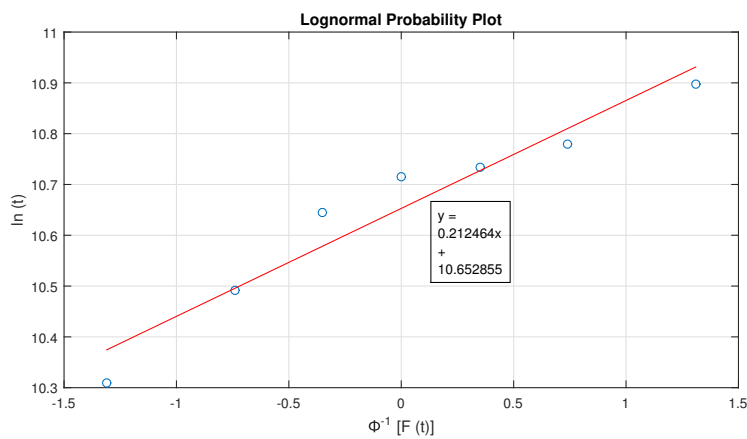


Figure 4.20: Resultant plot obtained from the linearization using the lognormal distribution.

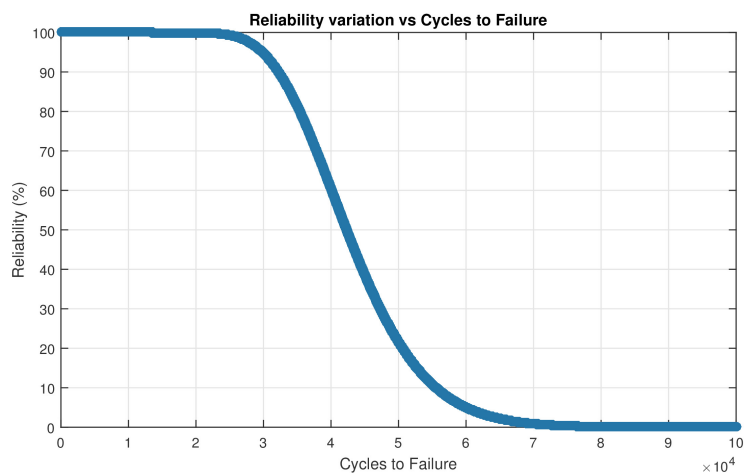


Figure 4.21: Reliability as a function of the number of cycles (until cycle 100,000) for a blind mating coaxial connector using the lognormal distribution.



From equation  $y = 0.2125x + 10.65$  shown in Figure 4.20, the parameter  $\sigma$  is 0.2125 and  $\mu$  is 10.65. Based on the equations of the Erf and  $\Phi$  functions represented in Table 2.5, that results in Figure 4.21. The calculation of reliability,  $\lambda$  and MTTF is based on the equations 2.13, 2.14 and 2.15 demonstrated in Table 2.5 where the results are presented in Table 4.3.

Another approach would be to use the exponential distribution. Albeit, when the linearization is applied according to equation 2.24, the resultant straight line ( $y = 0.000090x - 2.989$ ) does not go through the origin (shown in Figure 4.22) so it is not of the type  $y = mx$ . Consequently, the data does not follow an exponential distribution. Because of this fact, the failures of a 1.85 mm blind mating coaxial connector cannot be characterized using an exponential distribution.

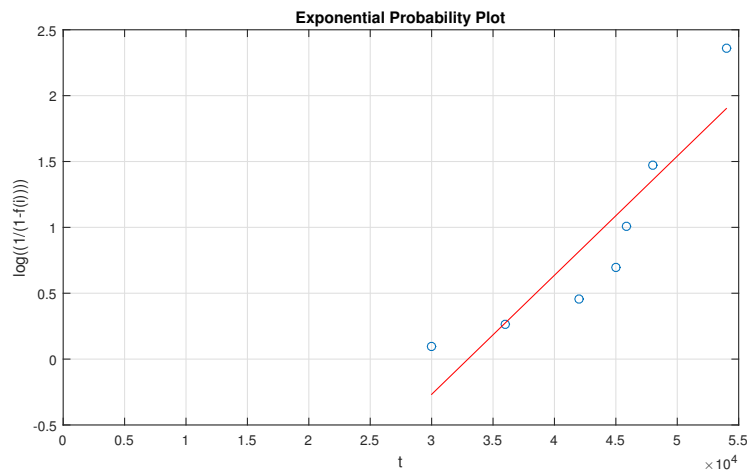


Figure 4.22: Resultant plot obtained from the linearization using the exponential distribution.

An alternative would be to consider that the MTTF = 42,985 cycles to failure. The calculation of this value is based on the average value of the cycles to failure of the 7 failed connectors expressed in Table 4.2. Figure 4.23 represents the reliability as a function of the number of cycles to failure considering the exponential distribution, where from equation 2.21, the resultant equation is  $R(t) = e^{-(1/42985)t}$ .

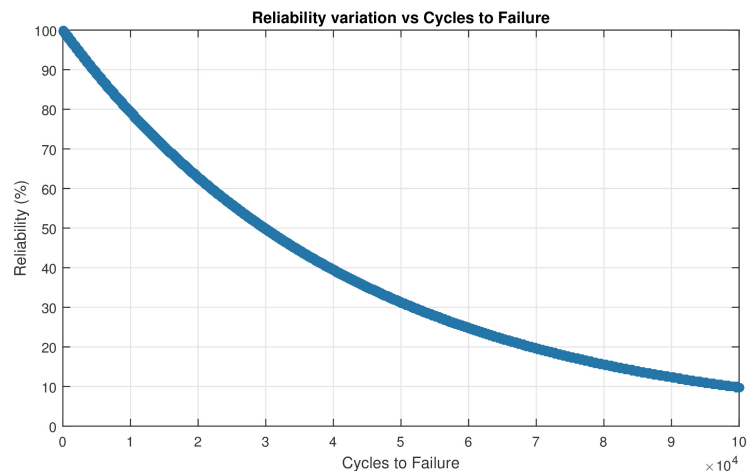


Figure 4.23: Reliability as a function of the number of cycles (until cycle 100,000) for a blind mating coaxial connector using the exponential distribution.

In agreement with Figure 4.19, 4.21 and 4.23, the reliability decreases with the increasing number of cycles to failure. Table 4.3 represents the comparison of different reliability percentages, as well as the failure rate and MTTF, for the different distributions used to model the connector reliability.

Distribution	Weibull	Lognormal	Exponential
$R(t) = 99\%$	19,948 <i>cycles</i>	25,822 <i>cycles</i>	430 <i>cycles</i>
$R(t) = 95\%$	26,914 <i>cycles</i>	29,836 <i>cycles</i>	2,203 <i>cycles</i>
$R(t) = 90\%$	30,721 <i>cycles</i>	32,226 <i>cycles</i>	4,527 <i>cycles</i>
<i>MTTF</i>	42,859 <i>cycles</i>	43,156 <i>cycles</i>	42,985 <i>cycles</i>
$\lambda(\text{constant})$	-	-	$2.32 \times 10^{-5} \frac{\text{failure}}{\text{cycles}}$
$\lambda(t = 20,000)$	$2.77 \times 10^{-6} \frac{\text{failure}}{\text{cycles}}$	$1.98 \times 10^{-7} \frac{\text{failure}}{\text{cycles}}$	-
$\lambda(t = 40,000)$	$6.02 \times 10^{-5} \frac{\text{failure}}{\text{cycles}}$	$7.08 \times 10^{-5} \frac{\text{failure}}{\text{cycles}}$	-
$\lambda(t = 60,000)$	$3.65 \times 10^{-4} \frac{\text{failure}}{\text{cycles}}$	$4.43 \times 10^{-4} \frac{\text{failure}}{\text{cycles}}$	-

Table 4.3: Comparison of different reliability percentage, failure rates and MTTF for the different distributions.

Exponential distribution represents a huge difference on the results obtained compared to the remaining distributions, though it is proved that the data does not follow an exponential distribution, so no physical meaning can be attributed to the application of this distribution on a reliability model for the studied 1.85 mm blind mating coaxial connector. Additionally, in [59, 61] examples of reliability studies using an exponential distribution are not shown, but instead 2-parameter Weibull distribution. Moreover, the failure mechanism identified by the characterization method SEM was fatigue. The exponential distribution is not used to model high cycle failures like is common in a fatigue test.

Otherwise, the Weibull and lognormal distributions present similar values. These distributions are considered as valid distributions to consider for reliability model of these components. The variations of the results concerning these distributions are based only on the 7 connectors that failed, therefore the considerable discrepancy is associated with the low number of components tested. For that reason, a future recommendation would be to increase the number of tested connectors so that a more realistic reliability estimation is obtained.

Nonetheless, since the target lifetime of the ATE system is 20,000 cycles to failure (insertions/ $N^{\circ}$  docking cycles), so even considering the highest value of reliability ( $R(t) = 99\%$ ) the 1.85 mm blind mating coaxial connectors withstand 19,948 insertions without failing assuming that the conditions of temperature, humidity, stress, among others are the same than the ones tested along this reliability test, which proves the high reliability of the studied 1.85 mm blind mating connector.

# Chapter 5

## Characterization

In this chapter, an introduction to SEM and CT methods is made. Then, a connector characterization identifying the failure mechanism and mode using both techniques is discussed.

### 5.1 Computed Tomography

The Computed Tomography (CT) technique used in medicine has evolved into a powerful investigation method for industrial and scientific purposes. Figure 5.1 demonstrate the main components inside a CT industrial machine, where the basic components are the x-ray tube, object manipulator and a detector.

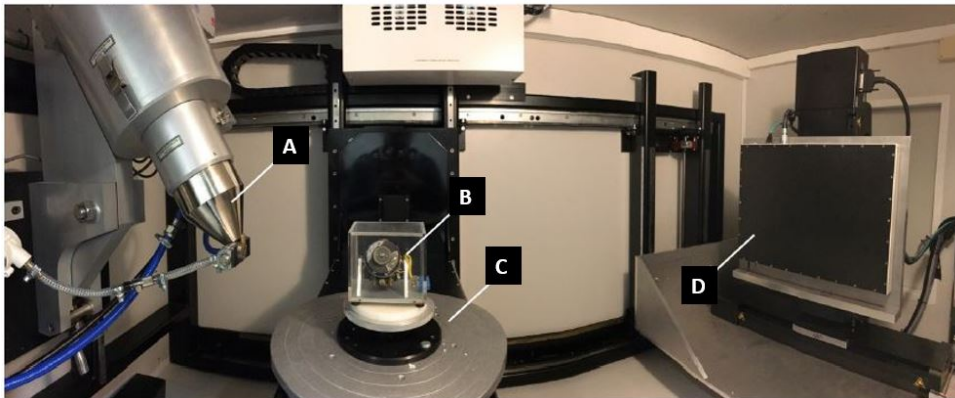


Figure 5.1: CT industrial measurement setup. A) X-ray tube, B) Part under test, C) Object manipulator, D) Flat panel detector.

The object manipulator is where the part under test is placed and works as a rotating plate. Electrons inside the x-ray tube are accelerated in the direction of tungsten (which is a heavy element) and due to a deceleration of the particles, electromagnetic radiation is produced within the x-rays band. The resultant beam penetrates any object. A projection is obtained in the x-ray detector on the other side. Using several projections under different rotations, a 3D reconstruction is obtained. This technique offer advantages in the development or maintenance of a product, since it is a non destructive technique where a full scan gives information on the surfaces of the exterior and interior of a component [73].

The contrast quality of the object depends on the interaction of the x-rays with the different materials. The atomic number is an indicator of the extent that a material can be radiated through, since a higher atomic number means a higher attenuation of the radiation. This means that, to compensate the differences of the levels of absorption for the different materials, higher energy levels have to be generated which leads to a saturation of the detector that compromises the image quality. The goal is to find an adequate level of penetration which depends on the detector [73]. An advantage of this technique is that it does not require any sample preparation. The connector has to be placed inside the CT machine and after some hours, the scan is obtained. The objective was to study if the body and surfaces of contact suffer considerable wear that affects directly the connector reliability and performance. The main goal of using this technique is to try to find a correlation between the mechanical and dimensional measurements obtained while testing and also to compare this technique to the SEM approach explained later.

There were two connectors (connectors 12 and 13) subjected to a physical characterization using the CT technique. A total of three scans were done to connector 12 and five scans to connector 13. For connector 12, the scans were performed before the accelerated test, after the accelerated test and after 30,000 cycles. For connector 13, each figure show an overlap of two consecutive scans (performed in ranges of 12,000 cycles), in order to compare the dimensional variations which are represented by a scale in mm. As addressed in the previous sections, the components of interest are the pin and socket. Although, a full scan let us make relevant conclusions about the remaining parts of the connector, such as the spring and the housing.

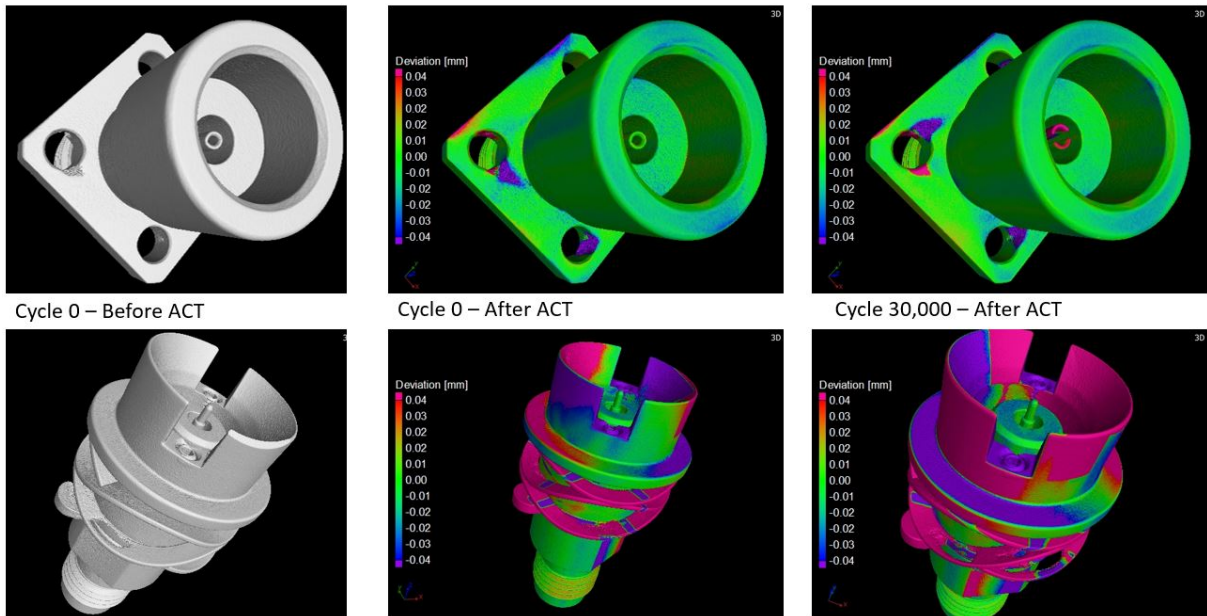


Figure 5.2: CT scans performed for the connector pairs 12.

Figure 5.2 represent the resultant scans for connector 12 using Volume Graphics software [74]. The scans with a grey coloration represent the first scan and the colored scans represent the maps of the resultant scan in comparison to the first one. Considerable variations are only registered at the last scan

(after 30,000 insertions). In the case of the second scan, after the accelerated test, a degradation of the housing is present but the pin and the socket seem to not demonstrate any degradation. In the case of the male housing, the dimensional variations represented for the spring and top part of the male are not valid, since the design itself has mechanical tolerances (male float mount is not fixed) so it is normal that the scans show colored regions in these zones. For this reason, the male scans are no longer discussed in the remainder of this chapter.

Furthermore, the maps of Figure 5.2 and 5.6, demonstrate that the surfaces of contact (in the interior of the connector housing) have shown a deviation between 10 and 30  $\mu m$ . This proves that the stainless steel is an adequate material for the connector housing and that the coupling while docking is smooth. The reduction of this value correlates with the pin depth measurement. The software allows to apply clipping planes to the object. Figure 5.3 demonstrates the socket and the pin of the last scan (after 30,000 insertions) by applying a clipping box cut.

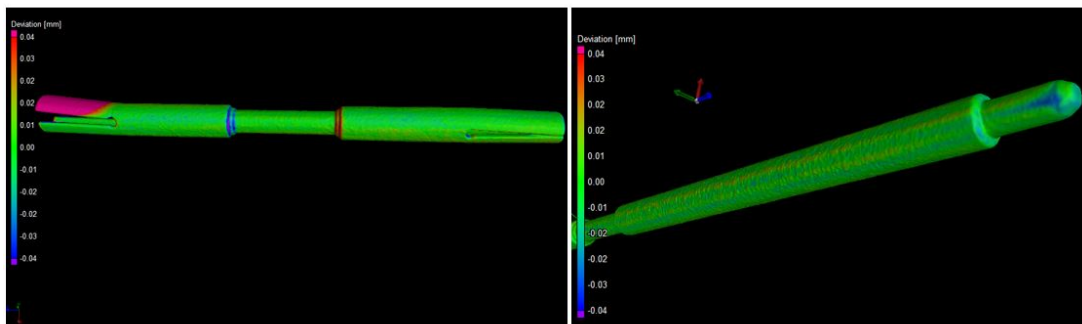


Figure 5.3: CT scan of the socket (on the left) and pin (on the right) of connector 12 after 30,000 cycles.

The only component that is not visible by a CT scan is the bead, since it is the only non metal material. When the connectors are subjected to an ACT, the bead loses strength with temperature. Consequently, after an ACT and with the increasing number of insertions the centre contact retention impacts the socket and the pin. The centre retention variations justify the red and blue areas of the socket shown in Figure 5.3 and the difference of the values of pin depth shown in Figure 4.17. Appendix B shows pictures of the connector housing after the ACT.

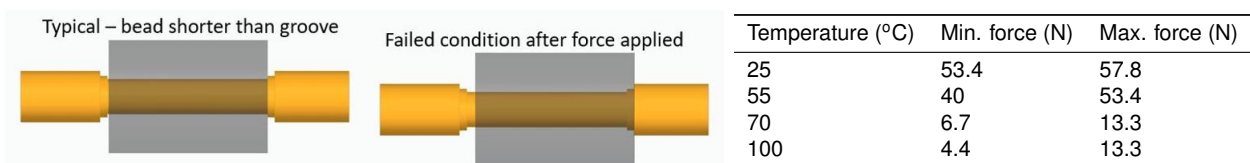


Figure 5.4: Centre contact retention deviation and temperature impact on the connector bead (provided by connector designer).

In practice, the application of temperature (85 °C) has not destroyed the bead but it degraded it. In order to study the behaviour of the bead with temperature, the connector designer measured the insertion forces after subjecting the bead to several temperatures. In Figure 5.4 is shown that from a temperature above 55 °C the minimum and maximum insertion forces decrease considerably. Then, the

connector is compromised due to the bead for applications that involve temperatures above 55 °C. This test was only executed after the connectors had been tested.

Similarly, Figure 5.5 shows the scans of connector 13 at different number of cycles. Each scan is done during the test with intervals of 12,000 cycles. The results obtained for each scan, are a comparison between cycle 0 and cycle 12,000, 24,000, 36,000, 48,000 and 60,000.

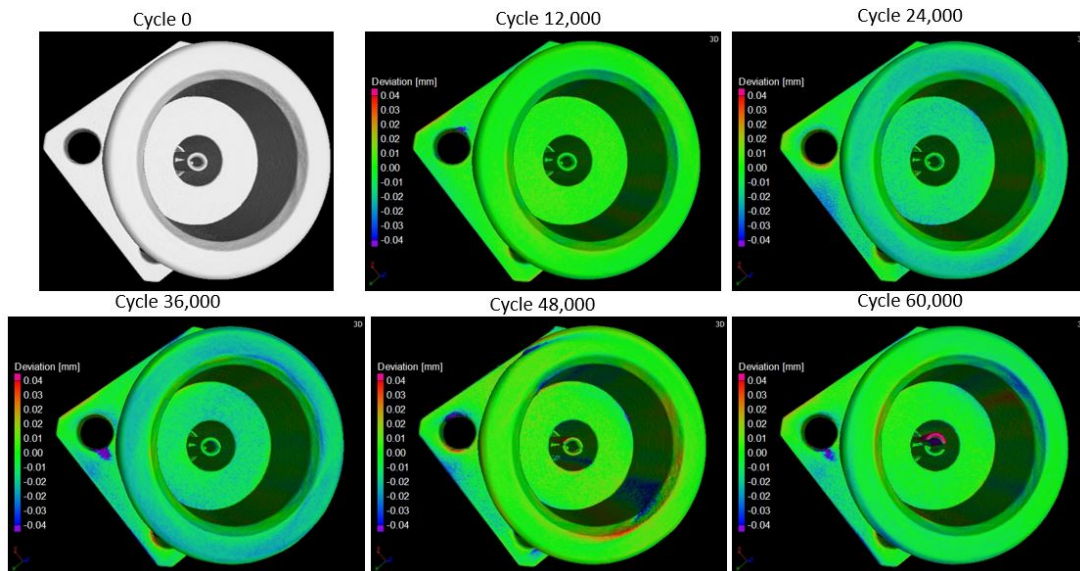


Figure 5.5: Scans at different cycles of the female connector 13.

Before 48,000 cycles, there is not a huge variation in the socket. This correlates to the contact resistance measurements and to the dimensional measurements shown in Section 4.1.2 and 4.2.2 respectively. After 30,000 cycles, Figure 5.6 shows the scans for the socket and pin of connector 13.

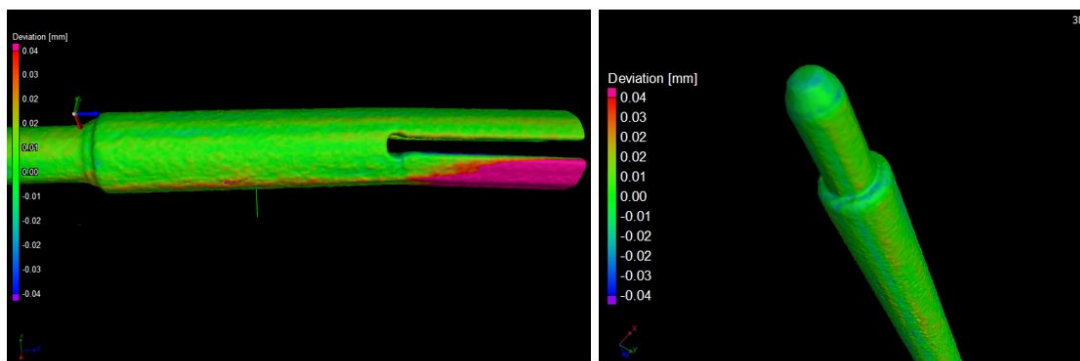


Figure 5.6: CT scan of the socket (on the left) and pin (on the right) for connector 13 after 60,000 cycles.

The scans performed for both connectors (Figure 5.3 and 5.6), let us conclude that the wear occurring at the pin is not considerable (the highest deterioration occurs on the top of the tip represented by a blue coloration). Regarding the socket, it does not show a uniform wear all over the surface of contact. Although, for both connectors, one of the fingers turned widely opened at the end of the tests. The aperture of the finger is translated in a failure in terms of S-parameters.

Another way to analyse if the connector is still on specification, an alternative to the concentricity

experimental measurement, is the measurement of the angle  $\alpha$ . This angle allows to register the socket aperture. It is represented in Figure 5.7 and the table on the side represents how these values vary for different number of cycles.

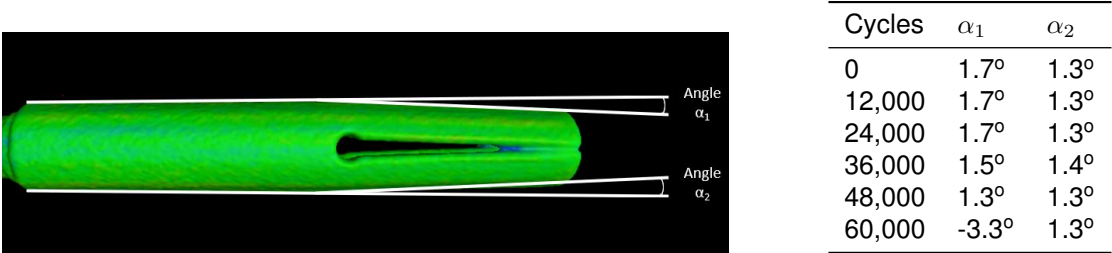


Figure 5.7: Explanation of the measurement angle  $\alpha$  and the resultant angles for the different number of cycles.

Angle  $\alpha_2$  remained practically the same during the 60,000 cycles. On the other hand,  $\alpha_1$  decreased after 24,000 cycles. Although there is some variation of the angle  $\alpha_1$  between cycle 24,000 and 48,000, that has no direct relation in terms of the connector reliability. Furthermore, the angle  $\alpha_1$  is the one that represents a higher angle (1.7 degrees) which means that the contact is established first in this finger. Therefore, higher stresses occur during contact and that is probably the reason why the failure occurred in this finger. Instead of placing both male and female parts inside of the CT equipment, only the female was inserted to find out the failure mechanism. This allows a better resolution of the final scan. Figure 5.8, shows the resultant scan.

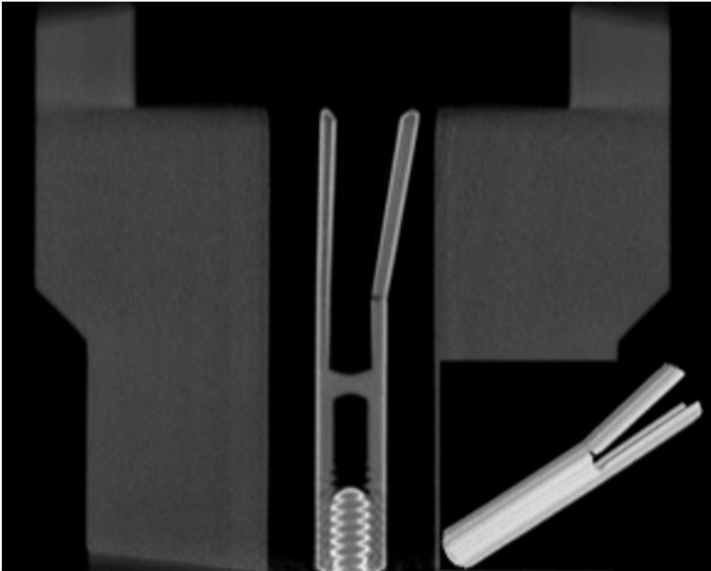


Figure 5.8: CT measurement of the crack of the female part of connector 13.

This scan suggests that the reason for the wide socket aperture and, consequently the connector failure, is due to a presence of a crack. The identification of a crack can be performed at any cycle since it is a non destructive technique. Moreover, in the case that a crack is in an initial phase, if the crack size can be measured, this allows to predict the lifetime of the connector. Although, limitations arise concerning the usage of this technique to measure this value.

The usage of this technique has two major limitations. One problem with metal objects is beam hardening artefacts. These effects reduce the contrast around metal edges and also make the crack difficult to detect. One solution to reduce these artefacts is to use a energy sensitive detector, which provides the intensity and energy of the photons. The second problem, is the focal spot of the x-ray source itself, where for the performed scans it was  $5 \mu m$ . This creates a physical limit on the resolution of the scan. The x-ray tubes with a focal spot of 500 nm are preferred. The use of better x-ray tubes improve the overall resolution of the system.

## 5.2 Scanning Electron Microscope

A Scanning Electron Microscope (SEM) is the ideal tool for high-resolution imaging of small structural features. A SEM also allows a chemical analysis, microstructural imaging and an electrical characterization of materials. It has a higher resolution than an optical microscope by a factor of 100 times, and allows the discovery of intermetallic phases formed between different materials, corrosion of metallic leads and migration of material due to high current densities on leading paths. The electron beam of a SEM gives also the possibility to obtain 3D images [43, 75].

The SEM is the second characterization tool used to characterize the connector in terms of physics of failure. The parts of interest to be analyzed by the SEM are the pin and the socket, which is where the contact occurs. Once these components are taken away from the connectors, they can no longer be replaced back so the connector is considered as destroyed. For this reason, this technique compared to the CT scan is a destructive method. Consequently, the characterization of these samples can only be done before and after testing for the same connector. The main goals are to measure the gold thickness and perform an Energy dispersive x-ray spectroscopy (EDS) analysis where the chemical elements are identified before and after testing for both pin and socket. In case a failure is registered after testing a connector, a detailed surface characterization of the pin and socket of that connector is performed.

Similarly to the CT scan technique, connector 12 and 13 were the samples chosen to do this SEM characterization. When the pin or socket are removed from the interior of a connector, they can no longer be replaced back (destructive test). Therefore, to measure the nickel and gold thickness before the cyclic stress testing, other pins and sockets under the same conditions of manufacturing were used for this initial measurement. The samples preparation is described as follows: First, the pin and socket are embedded in a resin; Afterwards, a grinding and polishing process is performed to expose the metal according a longitudinal section A-A represented in Figure 5.9; Finally, since the gold is in contact with the resin (the resin is a polymer, so a non conductive material), the samples were coated with a thin layer of gold (approximately 10 nm) to turn the samples conductive. Figure 5.10 presents the 4 samples studied before testing, where the samples on the left are for the pin and the samples on the right are for the inside surface of the socket. The gold and nickel layers are also shown in Figure 5.10.



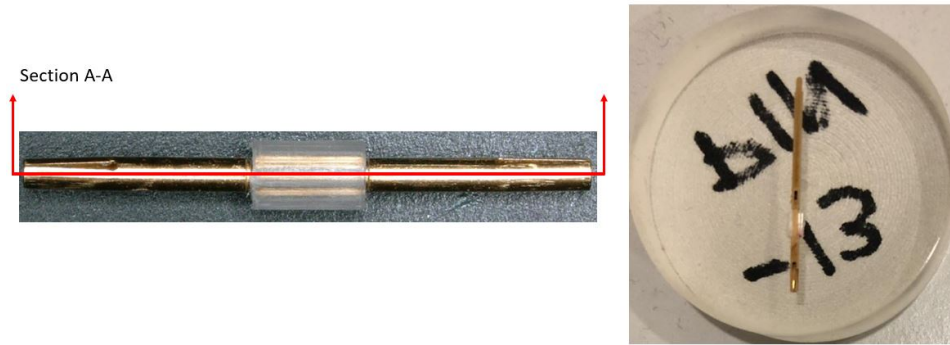


Figure 5.9: Sample preparation before SEM (on the left section A-A and on the right the resultant pin embedded in the resin).

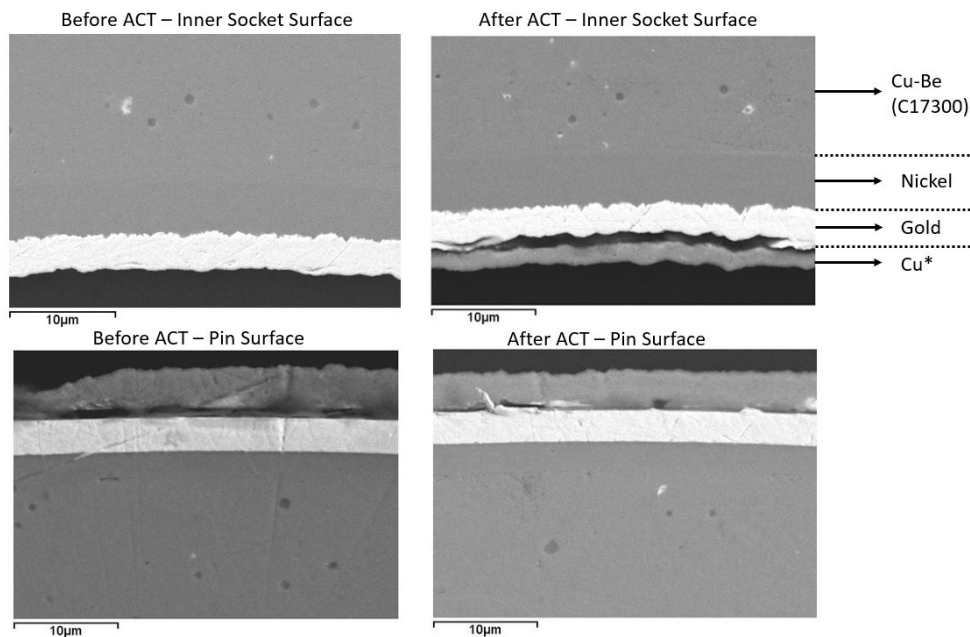


Figure 5.10: Measurement of inner and outside layers of the plating applied to the pin and socket <sup>1</sup>.

In the 4 samples there are some black particles (shown in Figure 5.10 with black circles) which are the beryllium precipitates added that are responsible for the high resistance conferred to copper beryllium alloys. It is expected that the coating thickness decreases with the number of cycles. Table 5.1 shows the gold and nickel thickness for the 4 samples calculated using fiji software [67]:

	Before Accelerated test (ACT)		After Accelerated test (ACT)	
	Pin	Socket	Pin	Socket
Gold Thickness ( $\mu\text{m}$ )	3.53	4.22	3.27	3.43
Nickel Thickness ( $\mu\text{m}$ )	3.02	5.58	2.91	5.69

Table 5.1: Measurements of gold and nickel thickness for pin and inner surface of the socket.

First of all, comparing the values in Table 5.1 with the values defined by the connector designer for the gold and nickel thickness (Section 2.2.5), the values of the nickel thickness are slightly higher for the socket. That might be related with the difficulties faced during the plating deposition for an inner surface.

<sup>1</sup>Cu\* required for sample preparation (turn the sample conductive).

The values before and after and accelerated test remained the same. Therefore, the ACT by itself has no direct influence in the gold and nickel coatings as it was proved by the CT technique. An EDS was performed where a chemical evaluation of the sample is performed. Figure 5.11 shows a spectrum of the inside surface of the socket after an ACT.

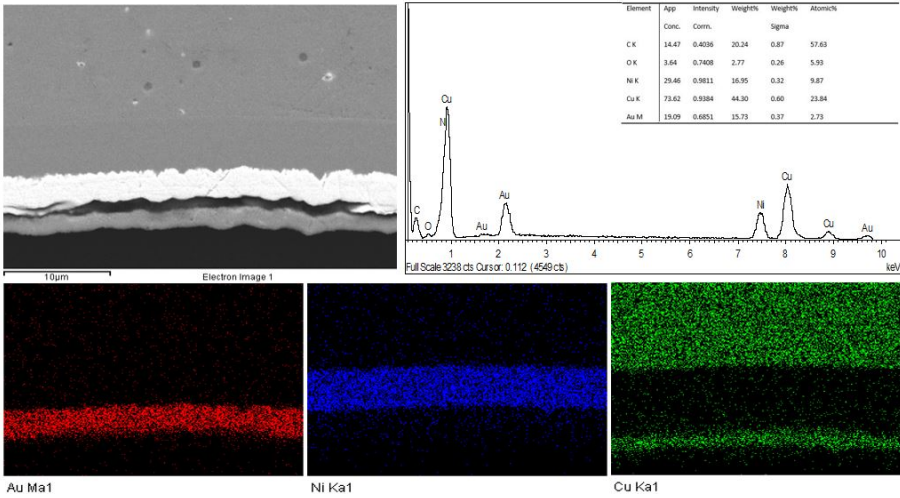


Figure 5.11: EDS analysis of the inner surface of the socket and correspondent spectrum.

The elements represented in Figure 5.11 are copper (Cu), gold (Au) and nickel (Ni). Beryllium was not detected because the x-ray interaction of this element is not captured with the source used, even though Figure 5.10 demonstrates that it is present. This allowed to conclude that after the ACT, there are no other chemical elements detected that may accelerate corrosion. Even though, the formation of compounds such as oxides, which may be masked by the oxygen percentage represented in the spectrum, during the test may work as an acceleration factor that influences the degradation of the gold and nickel layers rapidly and inhibit the electrical connection between the centre contacts which is translated in an electrical performance degradation. Figure 5.12 shows the surfaces of contact for connector 12 and 13.

Although connector 13 was tested for a higher number of cycles (60,000), it shows less degradation compared to connector 12 that has gone through a less number of insertions (30,000). In addition, connector 12 that has gone through an ACT before the cyclic testing, shows deeper grooves. Hence, the action of temperature and humidity plays a role in the surfaces of the socket and pin. Furthermore, for both connectors considerable wear occurs at the tip of the pin and the socket (represented by black regions) which is where the first contact is established during docking. In order to characterize those black regions, an EDS analysis was performed for connector 12 which is shown in Figure 5.13 and 5.14.

From EDS 1 and 2, the black regions represent that nickel is coming out to the surface, which means that the gold layer was ripped off in some zones. Although, gold represents better electrical conductivity and corrosion resistance than nickel, the reason for the connector failure was not due to a surface degradation. Then, unless all the gold layer disappears or the contact settles in a nickel area, the reliability of the connector is not directly affected by the wear but rather the electrical performance of the connector. As explained in the previous sections, the reason for the failure is related with the

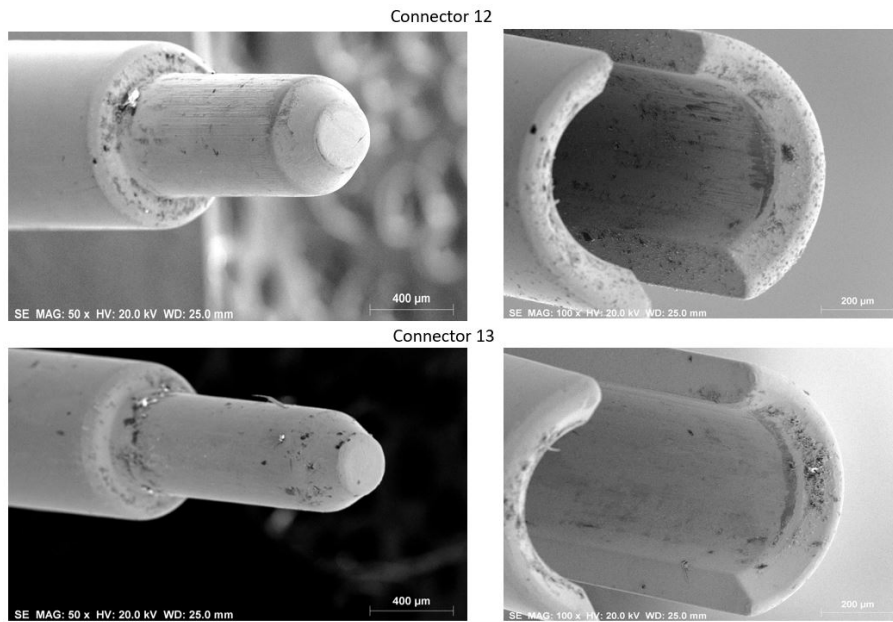


Figure 5.12: Pictures of contact surfaces of connector 12 and 13 after the reliability stress testing.

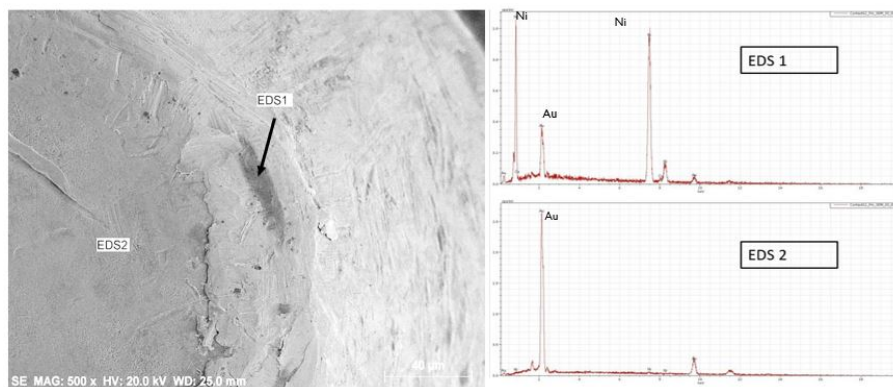


Figure 5.13: Localized EDS 1 and EDS 2 analysis of connector 12 (Top view at the tip of the pin, where first contact is established).

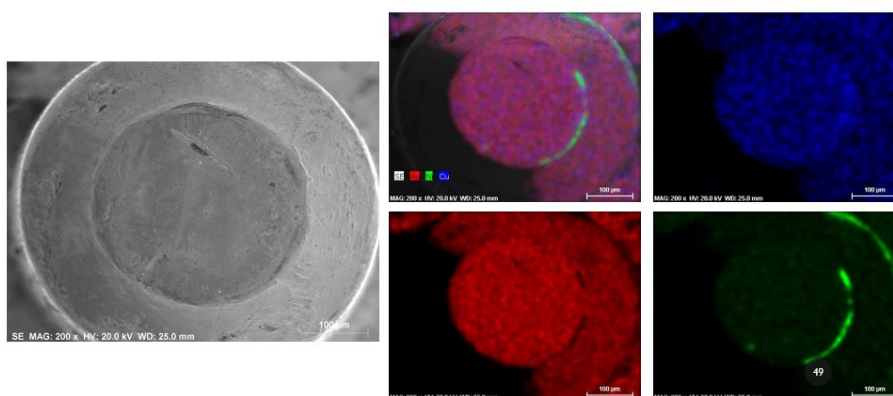


Figure 5.14: EDS analysis performed at the tip of the pin (connector 12).

appearance of a crack in the socket. In order to evaluate the reason why the crack appeared, an analysis of the fractured surface was conducted.

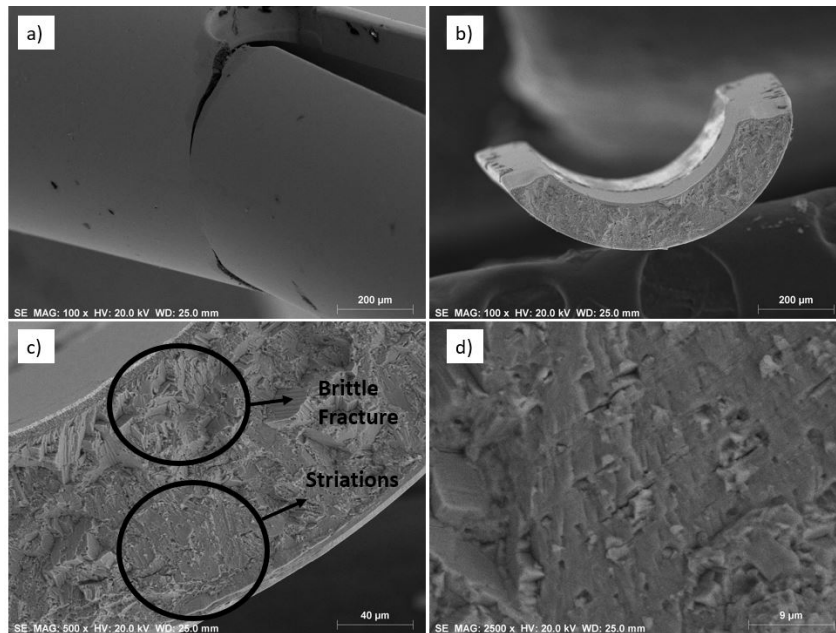


Figure 5.15: Analysis of fractured surface of connector 13. a) Crack appearance at the bottom of the socket; b) Picture of inside fractured surface after removing the finger from the socket; c) Picture of the brittle fracture; d) Amplification of the striations generated by fatigue.

Figure 5.15 shows the fractured surface of connector 13 when the finger is removed from the socket. In Figure 5.15 c), two different regions are identified. The first one indicates the presence of a brittle fracture where the cleavage fractures occur across crystallographic planes creating the ledges or steps represented. The second area exhibits what appears to be striations, which are more perceptible in Figure 5.15 d), although a more extensive study is necessary to confirm the presence of these striations. Rather than, in appendix F other figures show different areas of the fractured surface. Other failed connectors should be analyzed preferably using a Transmission electron microscopy (TEM) which allows a better resolution and amplification.

The formation of fatigue striations are caused by localized cyclic plastic deformation, therefore confirming the presence of fatigue. As the number of cycles increase, the presence of stress risers induces that the formation of micro cracks initiates. The micro cracks may initiate due to machining problems, corrosion pits or stress corrosion cracking. After several cyclic loading, the multiple micro cracks join together (crack propagation) until the fracture occurs, where the tensile stress exceeds the load carrying capacity of the remaining material section. The striations provide information on the material lifetime. According to [76], it is demonstrated how the counting of striations can relate to the number of cycles where the failure is initiated.

In this sample no ductile fracture was registered. As explained previously, the pins used to measure the withdrawal and insertion forces each 6,000 cycles generated high stress levels that induced fracture. Although, the high number of cycles represents a fatigue behaviour and it was a phenomena that contributed to the fracture created by the insertion and withdrawal pins.

# Chapter 6

## Modelling

In nature, several phenomena can be quantified with the application of physical laws by means of algebraic, differential and/or integral equations. Mathematical models are developed using assumptions concerning how the process works and the processes studied are simplified so that the governing equations can be solved. The Finite Element Method (FEM) is an example of a method used to solve those equations. It is a numerical method that involves a physical process governed by equations, a geometry and boundary conditions, where a given domain is viewed as a collection of subdomains. For each subdomain, the solution to the governing equation is approximated by any of the traditional variational methods. The several subdomains (also called finite elements) that include the geometrically domain of interest, are referred as geometric regions over which the equations are solved. Finally, the relationships between the different elements are assembled for the total model and allow to infer properties of the object under study [77, 78]. This chapter describes a model of the contact between the socket and pin based on the FEM. The main goals are to obtain the stresses and strains along the surfaces of contact. Two different types of simulations are accounted (one under the elastic regime and the other under the elastic-plastic regime). At the end of this chapter, the application of a fatigue module is used to calculate the number of cycles to failure. The application of mechanical simulations is an alternative way to study the reliability of the connector that allows to save time and resources.

### 6.1 Geometry and Global Definitions

The model used for the simulations was provided by the connector designer as a CAD file in the .step format. Figure 6.1 shows the geometry of the socket and pin prior to any modification. The software used to perform the mechanical simulations is COMSOL Multiphysics. The first step is to simplify the geometry (since there is symmetry), by applying a cut of one fourth of the total model. Secondly, the materials of the components must be defined. Considering that COMSOL Multiphysics library does not include the Beryllium Copper alloy UNS C17300 TH04, which corresponds to the socket and pin material, then the physical and mechanical properties needed, shown in Figure 6.1, were extracted from [79] and added to the model. Some properties shown in [79], such as the yield strength and the

ultimate strength, were presented in ranges, although for the simulation study, the minimum values were considered. The reason for this, is to consider a worst case scenario.

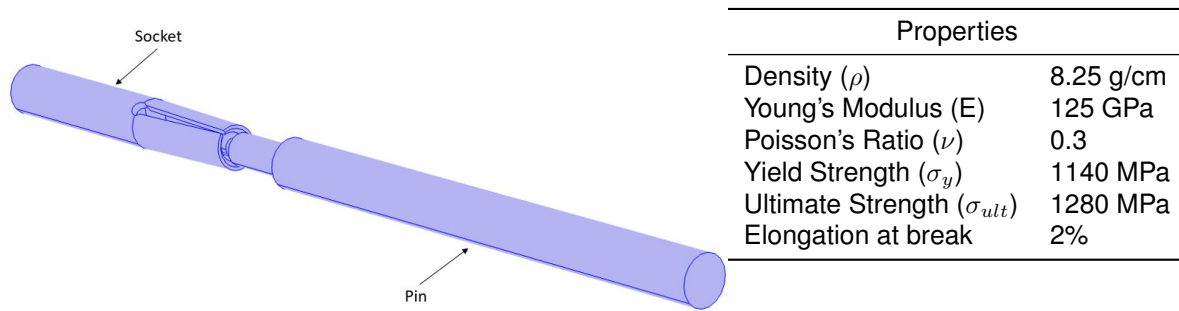


Figure 6.1: Socket and pin full model and table with the properties of a C17300 alloys under condition TH04.

As presented in section 2.2.5, the pin and socket materials are not only constituted by the beryllium copper alloy. Still, for the simulation study, since the thickness of nickel and gold are small compared to the total model, they are not considered, since they do not change considerably the mechanical strength of the component. Afterwards, the physics of contact is established. In order to do a mechanical evaluation, the components are initially defined as a linear elastic material in the solid mechanics option of COMSOL Multiphysics. Then, the surfaces of contact, boundary conditions and constraints are applied as can be seen in Figure 6.2. The socket is defined as free (no constraints), meaning that the movement is exercised by the socket only and the pin is fixed, as it occurs in reality during the ATE system docking cycle.

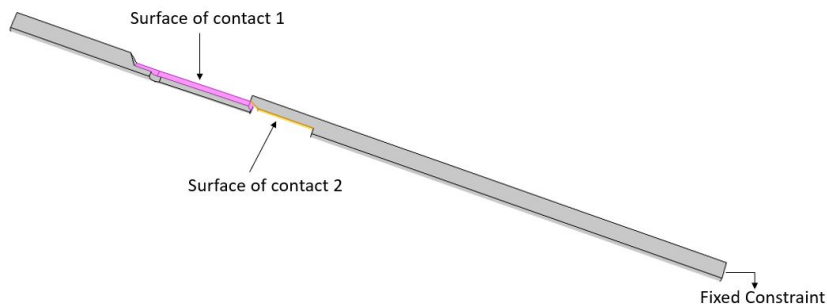


Figure 6.2: Final geometry used to simulate the contact between socket and pin.

In order to define the movement of the socket, a prescribed displacement was applied. The movement takes place only in one direction and the distance during contact (docking distance), as it is addressed in section 3.1, is 1.3 mm. Since the movement is characterized by a downward translation (docking) and afterwards an upward translation (undocking), it makes sense to define a periodic function in order to parametrize it. In the definitions tab of the COMSOL Multiphysics model builder, an analytic sine(x) function is defined, where x defines the displacement applied to the socket in the x direction. Figure 6.3 demonstrates the contact for different displacements/steps.

The elements used for the mesh were free tetrahedral quadractic elements. The size of the elements are predefined by COMSOL Multiphysics, according to parameters such as maximum and minimum

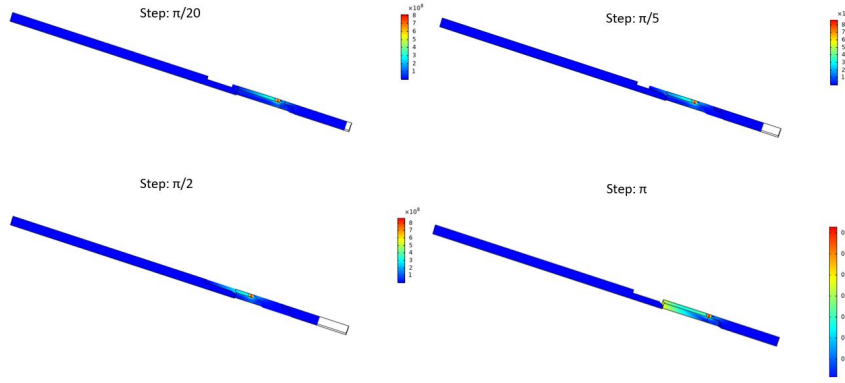


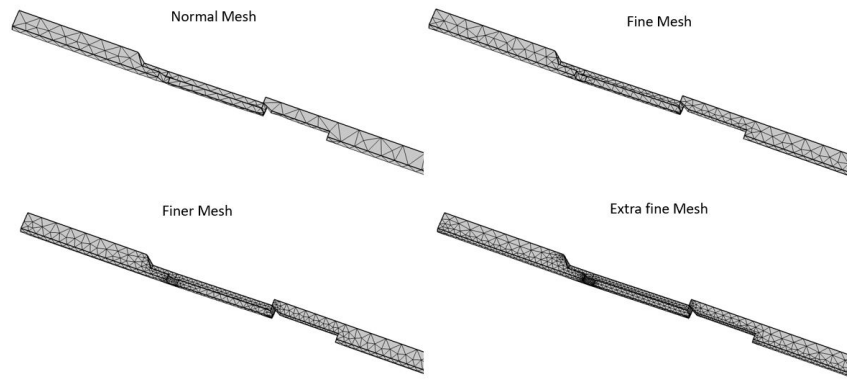
Figure 6.3: Representation of the contact at different steps for von Mises Stresses.

element size, maximum element growth rate, curvature factor and resolution of narrow regions. The simulation time and results are influenced by the choice of the mesh. The options of different predefined meshes include extremely fine, extra fine, finer, fine, normal, coarse, among others that are characterized by the parameters previously explained. In order to ensure an adequate mesh for the components, it is necessary to do a mesh convergence study. The mesh convergence study is done by using different meshes and comparing the result (the result can be a force, a stress, a strain, among others) for the different meshes. In this case, the result selected is the von Mises stress which is characterized by the following equation:

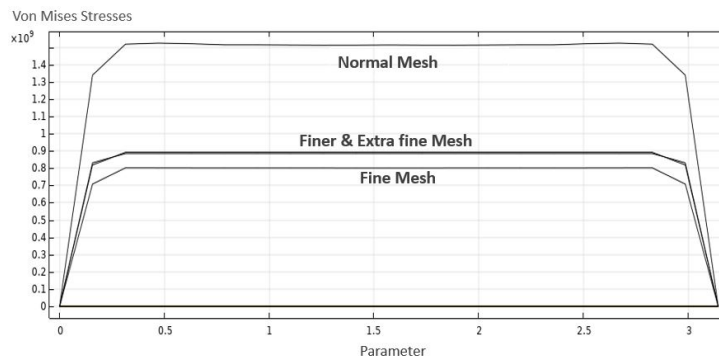
$$\sigma_v = \sqrt{\frac{(\sigma_1 - \sigma_2)^2 + (\sigma_2 - \sigma_3)^2 + (\sigma_3 - \sigma_1)^2}{2}} \quad (6.1)$$

When an error of around 1% is registered between two different meshes, the results converge to a value, meaning that the solution converges. The different meshes considered for this study are an extra fine, finer, fine and normal mesh. To accomplish that, a parametric sweep is performed, in which for each mesh the results of the von Mises stresses are plotted. The plot represented in Figure 6.4 shows four different lines, where each line corresponds to a different mesh. The y-axis are the von Mises stresses and x-axis the variable parameter. The meaning of the parameter variable is explained in the next paragraph. For the fine and finer meshes represented in Figure 6.4, the maximum error obtained for different parameters is of 1.48 % which in terms of von Mises stresses correspond to a difference of 7 MPa. This means that the used mesh for the simulations is the fine mesh.

In the study field of COMSOL Multiphysics tab model, a stationary step is designated where the parameter variable is defined. The parameter variable corresponds to the x variable of the sine function that defines the movement and where the range is between 0 and  $\pi$ . So, the step of the simulation is done considering the variable parameter and is defined by the user. In this case, the parameter has a step of  $\pi/20$  which corresponds to an increment in displacement of 0.2 mm. There are a total of 20 steps ( $\pi/20, 2\pi/20, 3\pi/20, 4\pi/20, \dots, \pi$ ). This value was chosen considering the displacement and the time of each simulation. All conditions are now gathered to perform the computational study and obtain the results which are presented in the following section.



(a) Different types of meshes.



(b) von Mises stresses vs parameter for different meshes.

Figure 6.4: Study of the convergence of the mesh.

## 6.2 Simulation Results

Initially the simulations were performed considering that the contact established between surfaces occurred under elastic conditions only. Hence, the defined material properties for these results did not include the yield and ultimate strength and the elongation at break presented in the table of Figure 6.1. Figure 6.5 represents the values of von Mises stresses in Pa at two different displacements.

At a displacement of 0.2 mm, the maximum von Mises stress is of 708.3 MPa and at a displacement of 0.92 mm the maximum von Mises stress is of 801.5 MPa. For both displacements, the higher values of stresses occur at the keyhole of the socket. This circular geometry works as a stress concentration riser, where the existence of micro flaws created by machining, empower the formation of a crack. Additionally, according to the simulations, and contrary to the expectation that was explained in the mechanical measurements section 4.2.1, the higher values of stresses do not occur when the first contact is established but for higher displacements. Then, the vertical alignment plays an important role on the influence of these values. Since the values of stresses remain constant between a displacement of 0.4 and 1.3 mm, then the results obtained for the first simulation consider always the same displacement, which corresponds to a prescribed value of 0.92 mm (step =  $\pi/4$ , parameter defined by the sine function). In the Appendix E, the values of stress and strain tensor components are represented. The prescribed displacement occurs in the x-direction, although during contact the displacements in the y and z axis are also of interest. Figure 6.6 represents the principal strain 1, 2 and 3 which allows to obtain a three dimensional evaluation of deformation.



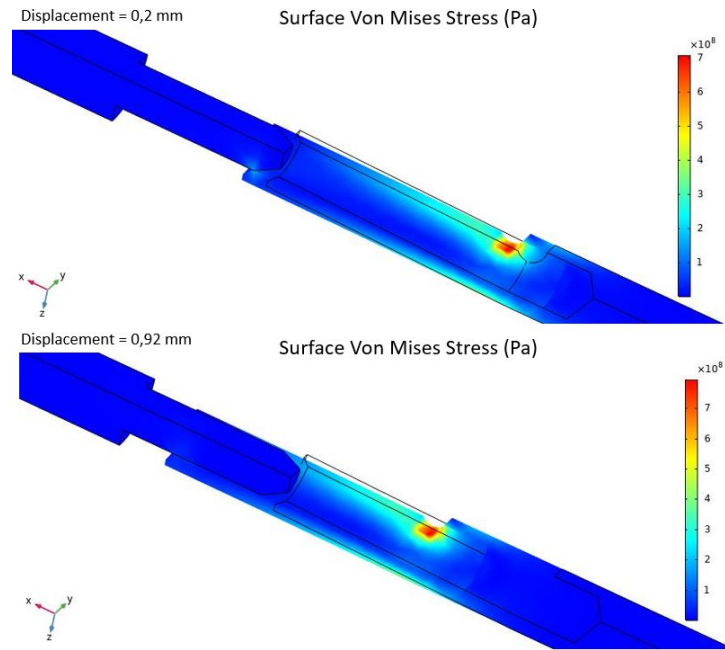


Figure 6.5: von Mises stresses at different displacements assuming only the elasticity regime.

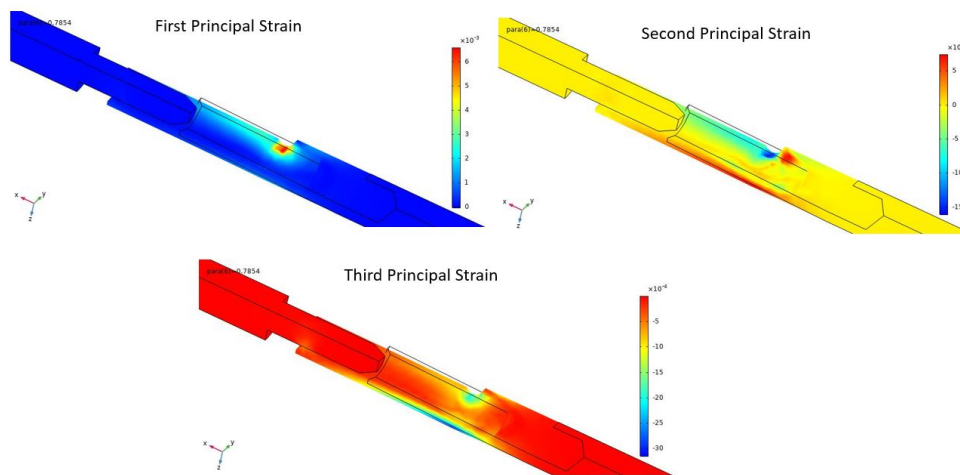


Figure 6.6: Principal strain components.

The presence of strain for the three directions allows to conclude, that the stresses and forces during contact also exist for different axis. There is a functionality in COMSOL Multiphysics that provides the force of contact between 2 surfaces. The resultant forces of contact for the x, y and z direction are respectively 0.25, 0.08 and 0.4 N. These forces of contact, are correlated with the insertion forces addressed in section 4.2.1. According to what was measured experimentally, the insertion force for 0 cycles are around 0.8 N, although this is a resulting force from the 3 directions measured by the force gauge equipment. The disparity of the experimental values compared to the simulation, might be related with the absence of a friction coefficient and to a vertical misalignment while measuring the insertion forces with the equipment. In a second step, the same simulation was done but considering the yield strength and isotropic tangent modulus (see Figure 6.7) in order to determine if there is plastic deformation. The exact same results were obtained, and no plastic strain was found which suggests that there is no plas-

tic deformation (under the test conditions that were simulated). This was expected since the maximum value of the von Mises stress is considerably below the theoretical yield stress (1140 MPa), which means that this simulation occurs only in the elastic regime.

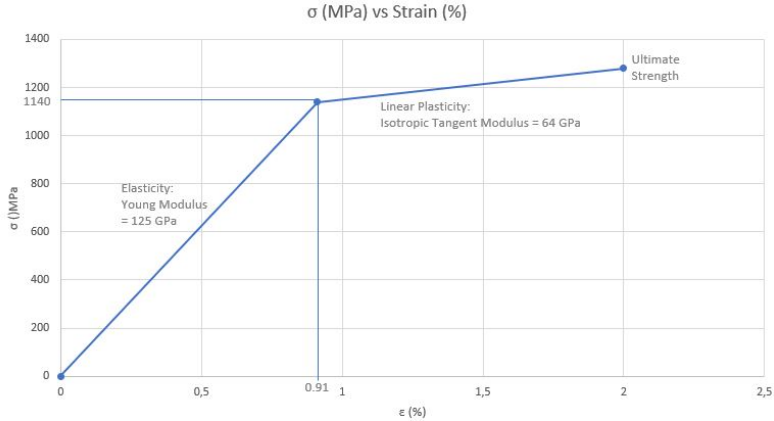


Figure 6.7: Stress-strain plot considered for the simulations.

In a realistic scenario, it is improbable that there is a perfect alignment between the socket and pin during contact (as it was shown by the concentricity measurements), because of all the mechanical tolerances encountered by the setup during docking. In order to mitigate this event, the pin was moved to a distance of 0.05 mm in the y and z directions, that corresponds to a deviation in terms of concentricity of 70  $\mu m$ . Figure 6.8 represents the von Mises stresses for this second simulation.

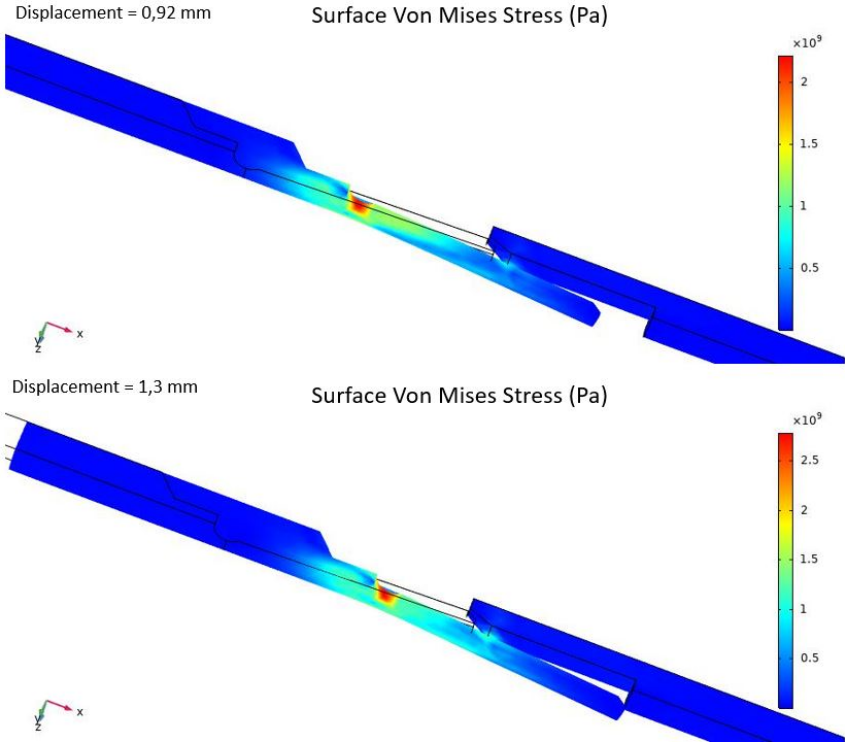


Figure 6.8: von Mises stresses at different displacements assuming the plasticity regime.

In this case, opposite to the first simulation, the value of the stresses and strains do not remain

constant, increasing with the displacement imposed. The maximum von Mises stress is of 4180 MPa for a displacement of 1.3 mm. This value is above the yield strength which indicates the presence of plasticity. The effective plastic strain is characterized by means of expression 6.2 which accounts for the integral of plastic strain rate which provides a measure of average plastic strain. In Figure 6.9 it is shown the resultant effective plastic strain during contact.

$$\epsilon_{ef} = \int_0^t \sqrt{\frac{2}{3} \epsilon_{ij} d\epsilon_{ij}} \tag{6.2}$$

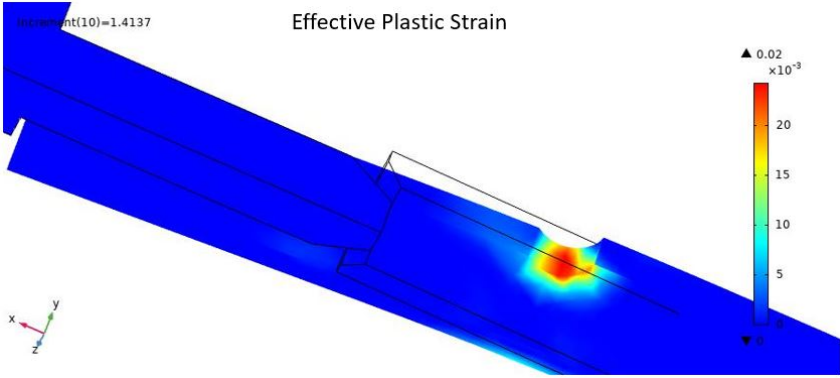


Figure 6.9: Effective plastic strain for a displacement of 1.3 mm.

The calculation of the number of cycles to failure was performed based on the fatigue module available in COMSOL Multiphysics. The results obtained from the second simulation were the values used to run the fatigue module, because it represents a more realistic situation in a worst case scenario. Moreover, the fatigue module of COMSOL Multiphysics is related with the stress or strain cycling methods, where a relation between stress or strain to cycles to failure is settled. The high cycle fatigue can be addressed with the classical S-N curves and Basquin model. On the other hand, the low-cycle fatigue prediction is based on the strain life models consisting of Coffin-Manson and E-N curve [80].

In this case, the usage of the fatigue model had as an input an S-N curve. In the literature it was not found any S-N curve for the copper beryllium alloy C17300 TH04. However, in [24] it was found a S-N curve for the alloy C17200 TH04 with a rod configuration, which is the most similar one in terms of mechanical properties and geometry to the one under study. In Figure 6.10 it is represented 2 different S-N curves, where the one chosen was the one for a diameter < 100 mm. At the right side of the figure, there is a table that correspond to the values inserted as a table which represents the S-N curve used in the fatigue module.

Based on Figure 6.10 the simulation was executed, and the critical zones were identified as well as a representation of cycles to failure in Figure 6.11. The red regions indicate the zones where the fatigue is more critical, so where the cracking will occur. Alike the von Mises stresses, the area where the plastic deformation is more intense is at the bottom of the socket. A future possibility to tone down this phenomena would be to think on a redesign of the socket in this region.

The calculated minimum number of cycles to failure due to fatigue is 106,000 cycles. This value is

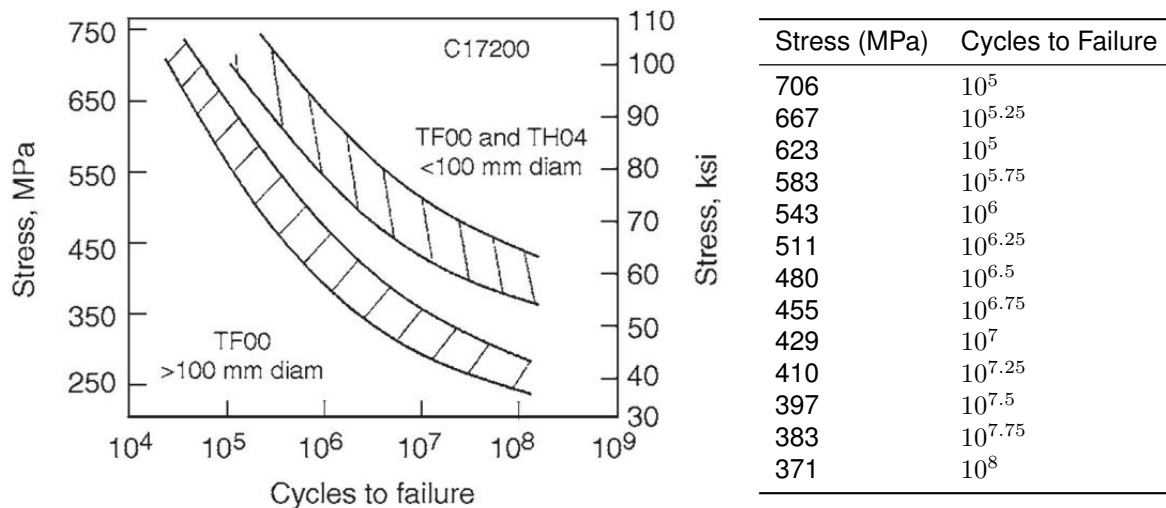


Figure 6.10: S-N curve of C17200 TH04 rod and table showing the correspondent values inserted in COMSOL Multiphysics.

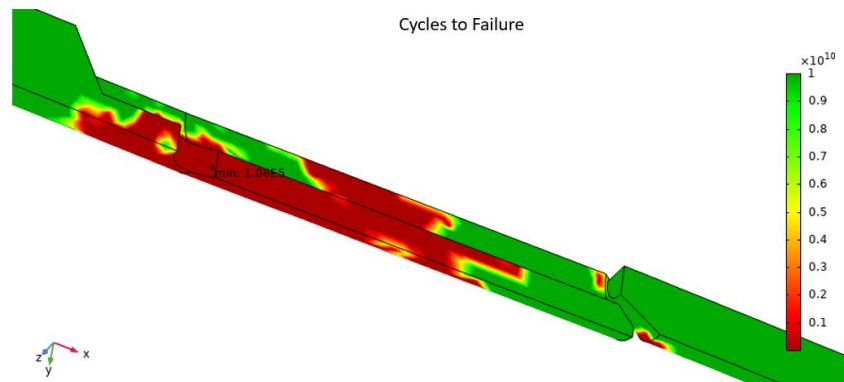


Figure 6.11: Cycles to failure obtained using the fatigue module available by COMSOL Multiphysics software.

above the experimental values where the failures were registered between 30,000 and 54,000 cycles. The difference of these values can be partially attributed to the uncertainty of the S-N curve. Likewise, the fatigue under study is multiaxial and of contact, meaning that a more comprehensive approach around the fatigue modules involving this type of fatigue should be equated, so that a equivalent uniaxial stress is calculated for the effects of the S-N curve. Even so, this is a work in progress so the module used can still be considered as an initial accurate approximation to the reality.

### 6.3 Simulation and measurements correlation

This section specifies the critical zone during the mechanical simulations. As can be seen in Figure 6.12, the keyhole of the socket undergoes the highest stress zone. This correlates to the failure site identified by the SEM and CT characterization methods. In Table 6.1 a comparison between the mechanical simulations is shown using different concentricity values and the experimental values for different connectors. The simulation results shown consider plasticity conditions.

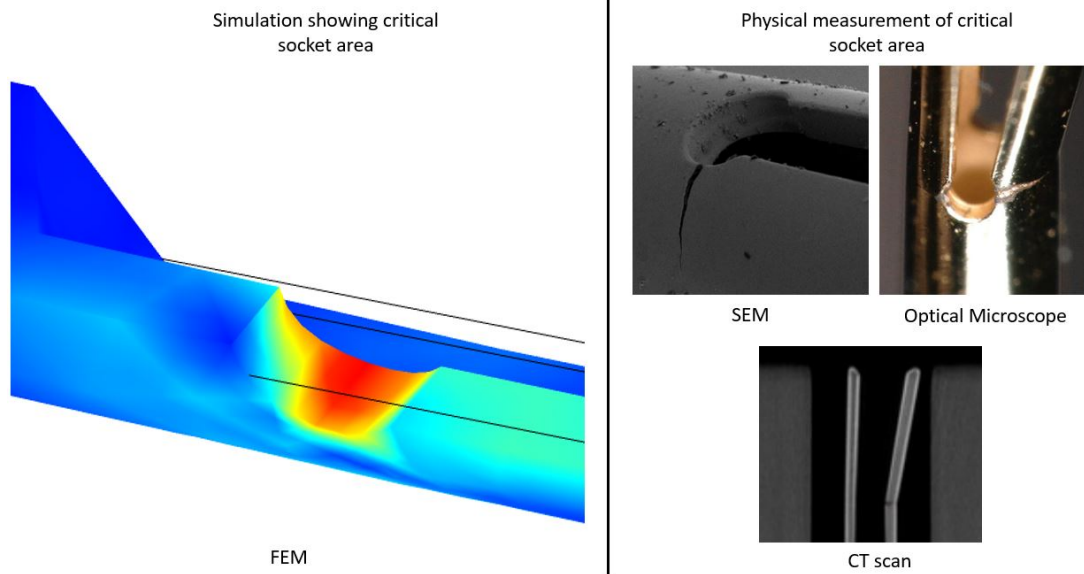


Figure 6.12: Comparison of the critical zone between the FEM simulation and the results from the physical characterization methods.

Simulation Results					Measured Results				
Concentricity ( $\mu m$ )	0	20	50	70		Connector 7		Connector 5	
von Mises stress (MPa)	801.5	1286	2043	4180		Cycle 0	After Failure	Cycle 0	After Failure
Contact Force x (N)	0.25	1.6	3.19	3.52	Insertion force (N)	1.18	0.058	0.84	0.19
Contact Force y (N)	0.08	4.51	8.3	8.8	Withdrawal force (N)	0.67	0	0.37	0.15
Contact Force z (N)	0.4	2.5	4.7	4.79	Socket Concentricity ( $\mu m$ )	37	212	37	173
Cycles to Failure	$4.11 \times 10^7$	165,000	109,000	106,000	Failure Cycle	-	45,900	-	48,000

Table 6.1: Comparison between simulation and experimental results.



# Chapter 7

## Conclusions

The main goal of this thesis was to perform a reliability study of a custom designed 1.85 mm blind mating coaxial connector. The commercial reason behind this project was the need of a reliable blind mating connector for automated testing of IC applications at a frequency range of 24-70 GHz.

In order to test the connectors, a reliability test plan was developed where an automated setup was implemented with different measuring instruments that were controlled by Matlab via GPIB.

The evaluation of the connector was performed using electrical measurements (S-parameters), that define if the connector has failed or not. Mechanical and dimensional measurements were also done so that a correlation to the electrical measurements is achieved. Moreover, after the stress testing, the connector characterization was implemented using a SEM and a CT techniques to understand the failure mode and mechanism.

The tests suggests that the failure occurs at the female component of the connector, more specifically at the keyhole of the socket. In these cases, the S-parameters show a in-band resonance for the S12 measurement and the contact resistance measurements demonstrate an increase of 10 m $\Omega$ . A correlation was found between the electrical, mechanical and dimensional measurements. The insertion and withdrawal forces decreased linearly with the increasing number of cycles. The limit with no failure was settled at 0.12 N for the insertion force. In the case of concentricity, it remained constant for the pin and socket until the cycle of failure and after that it increased but only for the sockets that failed. The pin depth remained constant during the whole test, so this measurement could not be correlated to a failed connector.

From the 14 tested connectors, only connector 1, 2 and 11 have survived with no failures. The failure for the connectors tested under the same conditions, occurred at different cycle numbers, where the earliest failure was registered at 30,000 cycles. The ACT have influenced the lifetime of the connectors due to a bead degradation, where the earliest failure was at 25,200 cycles (connector 12). The failed connectors were used to develop a reliability model. From the reliability models implemented, only Weibull and lognormal distributions are valid for this application. The Weibull distribution represented a number of cycles to failure of 19,948 and the lognormal distribution of 25,822 number of cycles to failure for a reliability of 99% of a generic 1.85 mm blind mating coaxial connector.

The SEM and CT techniques also proved that the failed pair component was the female. Both techniques demonstrated the presence of a crack at the keyhole of the socket. The CT scans evidenced a diminished wear of the housing of the connector although an increase of the socket aperture with the increase of cycle insertions. From a SEM analysis of the fractured surface, it allowed to conclude that there was a presence of striations. This indicates that fatigue was identified as the critical mechanism that caused the failure.

Finally, FEM was used to do a mechanical simulation on the contact between the socket and pin of the blind mating connectors. Two different types of simulations were performed. On the first simulation no plasticity was registered and the maximum von Mises stress was 801.5 MPa. The second simulation considers a deviation in terms of concentricity of the socket and demonstrates the occurrence of higher stresses and strains. The maximum von Mises stress was 4180 MPa (indicating the presence of plasticity) and occurs for the highest displacement (1.3 mm). For both simulations, the critical area was identified for the socket and exactly at the same place where the crack occurs experimentally as addressed by using SEM and CT methods. The usage of a fatigue module considering the second simulation, allowed to infer that the minimum cycles to failure was of 106,000 cycles.

Summarizing, the connectors demonstrated a high reliability (more than 30,000 insertions) considering that for the target ATE application a minimum number of 20,000 cycles is required.

## 7.1 Achievements

The major achievements of the presented work are:

- The development of an automated measurement setup to execute a reliability analysis plan;
- Development and implementation of a plan defining the conditions under test and the relevant electrical, mechanical and dimensional measurements required for the reliability analysis;
- The analysis concluded that the failure occurred at the female component, more specifically due to the presence of a crack in the socket;
- SEM and CT demonstrated to be extremely important methods to characterize the connector failure site and mechanism;
- The mechanical FEM simulation, simulation results correlate well with the measured data as well as with the characterization techniques, so it can be seen as a crucial part to consider while designing and testing of coaxial connectors.

## 7.2 Future Work

After completion of the task described in the present thesis, some recommendations can be given for future work in this topic. For example, the setup used to measure the withdrawal and insertion forces influenced the test itself. Therefore, an improvement on the setup used, could be to consider eliminating



the problem of misalignment so that no extra stresses are generated while measuring. Furthermore, for the pin depth measurement performed with the pin gauge, a smaller tip must be used or other alternative method would be to use a x-ray microscope.

The used reliability models show that the low number of tested connectors is a limitation to infer the number of cycles to failure to a bigger population. Therefore, more connectors should be considered and without doing any mechanical measurements that may influence the connector lifetime along the test, so that a more accurate statistical set of values is obtained. On the other hand, the use of a reliability model using Neural Networks could be of great advantage since there is a huge amount of data (scattering matrix). The prediction of the cycles to failure for a used connector that has not failed could be implemented using a time series or Recurrent Neural Networks (RNN) approach.

In terms of the characterization techniques, the CT scans could be done every 1,000 cycles to register the dimensional differences in more detail. In addition a different source could be used to allow better quality scans and also the recognition of the small cracks; then, based on the crack size, the number of cycles to failure may be estimated. Concerning SEM, an extensive analysis into the microstructure may also be of interest.

Hopefully, the hereby generated knowledge can be applied for further connectors with a higher frequency range of operation.



# Bibliography

- [1] M. Journal. 5G Opportunities and Challenges for the Microwave Industry, 2016. <https://www.microwavejournal.com/articles/25906-g-opportunities-and-challenges-for-the-microwave-industry> (accessed December 30, 2019).
- [2] S. Ellis. Cables, Connectors, and 5G: A Rosy Future, 2016. <http://www.mpdigest.com/2016/11/22/cables-connectors-and-5g-a-rosy-future/> (accessed December 30, 2019).
- [3] Y. Nishi and R. Doering. *Handbook of semiconductor manufacturing technology*. CRC Press, 2007.
- [4] P. Mhaisekar. An Incisive, In-depth Analysis on the 5g Tester Market, 2019. <https://www.futuremarketinsights.com/reports/5g-tester-market> (accessed December 30, 2019).
- [5] J. Davies. Anticipating And Addressing 5G Testing Challenges, 2019. <https://semiengineering.com/anticipating-and-addressing-5g-testing-challenges/> (accessed December 30, 2019).
- [6] Accton. The Emergence of 5G mmWave. <https://www.accton.com/Technology-Brief/the-emergence-of-5g-mmwave/> (accessed December 30, 2019).
- [7] J. Mundy. What is WiGig? <https://5g.co.uk/guides/what-is-wigig/> (accessed December 30, 2019).
- [8] J. Kastrenakes. Qualcomm's new Wi-Fi chips are meant to rival 5G speeds, 2018. <https://www.theverge.com/circuitbreaker/2018/10/16/17980124/80211ay-wigig-qualcomm-wifi-10-gigabit-speeds> (accessed December 30, 2019).
- [9] B. Rosas, J. Moreira, and D. Lam. Development of a 1.85 mm coaxial blind mating interconnect for ate applications. In *2017 IEEE MTT-S International Microwave Symposium (IMS)*, pages 503–506. IEEE, 2017.
- [10] M. Burns, G. W. Roberts, and F. Taenzler. *An introduction to mixed-signal IC test and measurement*, volume 2001. Oxford University Press New York, 2001.
- [11] J. Moreira and H. Werkmann. *An engineer's guide to automated testing of high-speed interfaces*. Artech House, 2010.

- [12] M. Maury Jr. Microwave coaxial connector technology: a continuing evolution. *Maury Microwave Corporation*, pages 1–21, 2005.
- [13] D. McReynolds. Optimize Your RF/MW Coaxial Connections. <https://www.rfindustries.com/resources/white-papers/optimize-rf-microwave-coaxial-connections.php> (accessed December 30, 2019).
- [14] G. Subcommittee. Ieee standard for precision coaxial connectors. *IEEE Trans. Instrum. Meas*, 17 (3):204–204, 1968.
- [15] N. Doertenbach. Power supply ess: A case study evaluating ipc 9592a recommendations. In *2012 Proceedings Annual Reliability and Maintainability Symposium*, pages 1–5. IEEE, 2012.
- [16] J. De Vries and E. Janssen. Humidity and reflow resistance of flip chip on foil assemblies with conductive adhesive joints. *IEEE Transactions on Components and Packaging Technologies*, 26 (3):563–568, 2003.
- [17] E. I. Association et al. Steady state temperature humidity bias life test. *EIA/JEDEC22-A101-B (Rev. JESD22-A101-A)*, 1997.
- [18] C. Zorn and N. Kaminski. Acceleration of temperature humidity bias (thb) testing on igbt modules by high bias levels. In *2015 IEEE 27th International Symposium on Power Semiconductor Devices & IC's (ISPSD)*, pages 385–388. IEEE, 2015.
- [19] D. of Defense. "MIL-PRF-39012, Connectors, Coaxial, Radio Frequency, General Specification for", April 2005. Retrieved 13 April 2012.
- [20] M. Specification. Mil-std-202g-method 204d. *Test method standard: electronic and electrical component parts. Vibration, high frequency. Department of Defense*, page 6, 2002.
- [21] D. of Defense. "Reliability Prediction of Electronic Equipment", December 1991.
- [22] J. Browne. Cables and Connectors Head for Higher Frequencies, August 2017. <https://www.mwrf.com/components/cables-and-connectors-head-higher-frequencies> (accessed December 30, 2019).
- [23] J. Harkness, W. Spiegelberg, and W. Cribb. *Guide to Beryllium Copper*. Brush Wellman Cleveland, OH, 1988.
- [24] J. R. Davis et al. *Copper and copper alloys*. ASM international, 2001.
- [25] C. EnriqueRocha-Rangel, José A.Rodríguez-García. Precipitation hardening of cu-be alloys. *ChemXpress*, pages 132–136, 2014.
- [26] A. C. Charles Tumbaga. 0.8 mm Connectors Enable D-Band Coaxial Measurements, March 2019. <https://www.microwavejournal.com/articles/31899-8-mm-connectors-enable-d-band-coaxial-measurements?v=preview> (accessed December 30, 2019).

- [27] D. M. Pozar. *Microwave engineering*. John Wiley & Sons, 2009.
- [28] D. T. Phillips and A. Garcia-Diaz. *Fundamentals of network analysis*, volume 198. Prentice-Hall Englewood Cliffs, 1981.
- [29] Anritsu. About S-Parameters and the Frequency Domain, 2009. <http://na.support.keysight.com/plts/help/WebHelp/Analyzing/Analyzing> (accessed December 30, 2019).
- [30] P. Gressens. Modeling Devices with S-parameters, May 2019. <https://www.gquipment.com/blog/modeling-devices-with-s-parameters> (accessed December 30, 2019).
- [31] BNC connector, September 2019. [https://en.wikipedia.org/wiki/BNC\\_connector](https://en.wikipedia.org/wiki/BNC_connector) (accessed December 30, 2019).
- [32] New Spinner 1.35 mm E Connector, November 2018. <https://www.spinner-group.com/en/news/news-centre/514-1-35-mm-e-connector> (accessed December 30, 2019).
- [33] B. Oldfield. *The Importance of Coax Connector Design Above 110 GHz*. Anritsu, September 2014. <https://dl.cdn-anritsu.com/ja-jp/test-measurement/reffiles/About-Anritsu/R.D/Technical/E-22/22.07.pdf> (accessed December 30, 2019).
- [34] M. D. Dale Johnson, David Hu. Multi-site dut to tester interfacing for mmwave devices. Proceedings of ITC 2019 : IEEE International Test Conference, Nov 12 - Nov 14, 2019, Washington D.C., USA.
- [35] Standard Classification System for Polychlorotrifluoroethylene (PCTFE) Plastics, 2017. <https://www.astm.org/Standards/D1430.htm> (accessed December 30, 2019).
- [36] B. Rosas. *Technical report of AM70F70-101 and AF70F70-102 Connector Series Specifications*. Signal Microwave, April 2019.
- [37] X. Guoliang, W. Qiangsong, M. Xujun, X. Baiqing, and P. Lijun. The precipitation behavior and strengthening of a cu–2.0 wt% be alloy. *Materials Science and Engineering: A*, 558:326–330, 2012.
- [38] I. Lomakin, M. Castillo-Rodríguez, and X. Sauvage. Microstructure, mechanical properties and aging behaviour of nanocrystalline copper–beryllium alloy. *Materials Science and Engineering: A*, 744:206–214, 2019.
- [39] *Nickel Plating (Electrodeposited)*. Federal Specification, April 1954. <https://www.engineersedge.com/qq-N-290A.PDF> (accessed December 30, 2019).
- [40] *Gold plating, Electrodeposited*. Departments and Agencies of the Department of Defense, June 1993. [http://everyspec.com/MIL-SPECS/MIL-SPECS-MIL-DTL/MIL-DTL-45204D\\_23625/](http://everyspec.com/MIL-SPECS/MIL-SPECS-MIL-DTL/MIL-DTL-45204D_23625/) (accessed December 30, 2019).

- [41] Compression Molding and Machining of PCTFE / Kel-F® / NEOFロン (Thermech), 2019. <http://www.thermech.com/PCTFE-Kel-F-NEOFロン-compression-molding.html> (accessed December 30, 2019).
- [42] T. I. Băjenescu, T.-M. I. Băjenescu, and M. I. Băzu. *Component reliability for electronic systems*. Artech House, 2010.
- [43] M. Ohring. *Reliability and failure of electronic materials and devices*. Elsevier, 1998.
- [44] M. Pecht. *Product reliability, maintainability, and supportability handbook*. CRC Press, 2009.
- [45] D. Natarajan. *Reliable Design of Electronic Equipment*. Springer, 2015.
- [46] J. A. Defeo and J. M. Juran. *Juran's Quality Handbook: The Complete Guide to Performance Excellence 6/e*. McGraw Hill Professional, 2010.
- [47] P. Nuñez. Análise da fiabilidade e disponibilidade de sistemas de navios. Master's thesis, Instituto Superior Técnico, December 2014.
- [48] ReliaWiki. The Weibull Distribution, 2019. [http://reliawiki.org/index.php/The\\_Weibull\\_Distribution](http://reliawiki.org/index.php/The_Weibull_Distribution) (accessed December 30, 2019).
- [49] ReliaWiki. The Lognormal Distribution, 2019. [http://reliawiki.org/index.php/The\\_Lognormal\\_Distribution](http://reliawiki.org/index.php/The_Lognormal_Distribution) (accessed December 30, 2019).
- [50] E. S. Handbook. Probability plotting, 2019. <https://www.itl.nist.gov/div898/handbook/apr/section2/apr221> (accessed December 30, 2019).
- [51] E. S. Handbook. Lognormal, 2019. <https://www.itl.nist.gov/div898/handbook/apr/section1/apr164> (accessed December 30, 2019).
- [52] ReliaWiki. The Exponential Distribution, 2019. [http://reliawiki.org/index.php/The\\_Exponential\\_Distribution](http://reliawiki.org/index.php/The_Exponential_Distribution) (accessed December 30, 2019).
- [53] Y.-L. Lee, M. E. Barkey, and H.-T. Kang. *Metal fatigue analysis handbook: practical problem-solving techniques for computer-aided engineering*. Elsevier, 2011.
- [54] S. of Automotive Engineers. *SAE Fatigue design handbook: AE-22*. Society of Automotive Engineers, 1997.
- [55] F. Goedel, G. P. Mezzomo, and Z. M. C. Pravia. Fatigue lifespan of a fillet welded joint-hybrid approach to obtain the sn curve with a reduced number of tests. *Latin American Journal of Solids and Structures*, 15(10), 2018.
- [56] P. van Dijk. Critical reliability aspects of electrical contacts. [http://www.pvdijk.com/pdf/PVDDIJK\\_ICREPEC2007.pdf](http://www.pvdijk.com/pdf/PVDDIJK_ICREPEC2007.pdf) (accessed in December 30, 2019).

- [57] R. S. Mroczkowski. Concerning reliability modeling of connectors. In *Electrical Contacts-1998. Proceedings of the Forty-Fourth IEEE Holm Conference on Electrical Contacts (Cat. No. 98CB36238)*, pages 57–68. IEEE, 1998.
- [58] R. S. Mroczkowski. A perspective on connector reliability. In *Proc. 50th IEEE Holm Conf. Electr. Contacts 22nd Int. Conf. Electr. Contacts*, pages 1–28, 2004.
- [59] Y. Zhou, Y. Su, Q. Li, Q. Jin, and J. Gao. A new lifetime prediction method based on particulate contaminants for coaxial connectors. In *2016 International Conference on Applied Mathematics, Simulation and Modelling*. Atlantis Press, 2016.
- [60] P. Varde, M. Agarwal, P. Marathe, U. Mohapatra, R. Sharma, and V. Naikan. Reliability and life prediction for electronic connectors for control applications. In *2010 2nd International Conference on Reliability, Safety and Hazard-Risk-Based Technologies and Physics-of-Failure Methods (ICRESH)*, pages 63–67. IEEE, 2010.
- [61] Y. Ren, Q. Feng, T. Ye, and B. Sun. A novel model of reliability assessment for circular electrical connectors. *IEEE Transactions on Components, Packaging and Manufacturing Technology*, 5(6): 755–761, 2015.
- [62] R. Ji, J. Gao, G. Xie, G. T. Flowers, and Q. Jin. The impact of coaxial connector failures on high frequency signal transmission. In *2015 IEEE 61st Holm Conference on Electrical Contacts (Holm)*, pages 298–303. IEEE, 2015.
- [63] D. Bergfried and H. Fischer. Insertion-loss repeatability versus life of some coaxial connectors. *IEEE Transactions on Instrumentation and Measurement*, 19(4):349–353, 1970.
- [64] *Klimaprüfschränke ClimeEvent*. Weistechnik, Greizer Straße 41–49 35447 Reiskirchen/Germany, 2018. <https://www.weiss-technik.com/fileadmin/Redakteur/Mediathek/Broschueren/WeissTechnik/Umweltsimulation/Weiss-Technik-ClimeEvent-DE.PDF> (accessed December 30, 2019).
- [65] Anritsu. *VectorStar MS4640A Series Microwave Vector Network Analyzers (VNAs)*. 490 Jarvis Drive Morgan Hill, CA 95037-2809 USA, April 2005. <https://dl.cdn-anritsu.com/en-us/test-measurement/files/Manuals/Operation-Manual/10410-00266L.pdf> (accessed December 30, 2019).
- [66] *DF II Series Digital Force Gauges for DFS II, DFS II-R, DFS II-R-ND and DFE II Models*. AMETEK Measurement and Calibration Technologies, 8600 Somerset Drive Largo, FL 33773 United States of America, July 2017. [https://www.ametektest.com/-/media/ametektest/download\\_links/data-force-gauges-dfs-ii-1803.pdf](https://www.ametektest.com/-/media/ametektest/download_links/data-force-gauges-dfs-ii-1803.pdf) (accessed December 30, 2019).
- [67] J. Schindelin, I. Arganda-Carreras, E. Frise, V. Kaynig, M. Longair, T. Pietzsch, S. Preibisch, C. Rueden, S. Saalfeld, B. Schmid, et al. Fiji: an open-source platform for biological-image analysis. *Nature methods*, 9(7):676, 2012.

- [68] *365xx-x Mechanical Calibration Kits*. Anritsu, 490 JARVIS DRIVE MORGAN HILL, CA 95037-2809, March 2018. <https://dl.cdn-anritsu.com/en-us/test-measurement/files/Manuals/Users-Guide/10200-00040C.pdf> (accessed December 30, 2019).
- [69] VHX-6000 Series Digital Microscope Catalog (Keyence), 2019. <https://www.keyence.com/products/microscope/digital-microscope/vhx-6000/index.jsp> (accessed December 30, 2019).
- [70] *Agilent 34410A/11A 6 Digit Multimeter*. Agilent Technologies, Agilent Technologies, Inc. 3501 Stevens Creek Blvd. Santa Clara, CA 95052 USA, June 2012. <https://www.keysight.com/us/en/assets/7018-01326/data-sheets/5989-3738.pdf> (accessed December 30, 2019).
- [71] *Power supply HMP4030 HMP4040 Handbuch / Manual*. HAMEG Instruments GmbH, May 2009. [https://scdn.rohde-schwarz.com/ur/pws/dl\\_downloads/dl\\_common\\_library/dl\\_manuals/gb\\_1/h/hmp](https://scdn.rohde-schwarz.com/ur/pws/dl_downloads/dl_common_library/dl_manuals/gb_1/h/hmp) (accessed December 30, 2019).
- [72] *Pressure regulators LR/LRS/LRB/LRBS, D series*. Festo, July 2017. <https://www.festo.com/media/pim/124/D15000100122124.PDF> (accessed December 30, 2019).
- [73] T. M. Buzug. Computed tomography. In *Springer Handbook of Medical Technology*, pages 311–342. Springer, 2011.
- [74] V. Graphics. myVGL Is the Free Viewer App for Projects Created with Volume Graphics Software, June 2019. <https://www.volumegraphics.com/en/products/myvgl.html> (accessed December 30, 2019).
- [75] L. Reimer. *Scanning electron microscopy: physics of image formation and microanalysis*, volume 45. Springer, 2013.
- [76] P. DeVries, K. Ruth, and D. Dennies. Counting on fatigue: Striations and their measure. *Journal of failure analysis and prevention*, 10(2):120–137, 2010.
- [77] J. N. Reddy. An introduction to the finite element method. *New York*, 1993.
- [78] Z. Bofang. The finite element method theory and applications. *China Water & Power Press, Beijing*, 1998.
- [79] Beryllium Copper, UNS C17300, TH04 Temper rod (Matweb), March 2019. <http://www.matweb.com/search/datasheet.aspx?matguid=20a32394534d43129772921eec296ace> (accessed December 30, 2019).
- [80] Comsol. Analyze Stress- and Strain-Based High- and Low-Cycle Fatigue with the Fatigue Module, September 2019. <https://uk.comsol.com/fatigue-module> (accessed December 30, 2019).

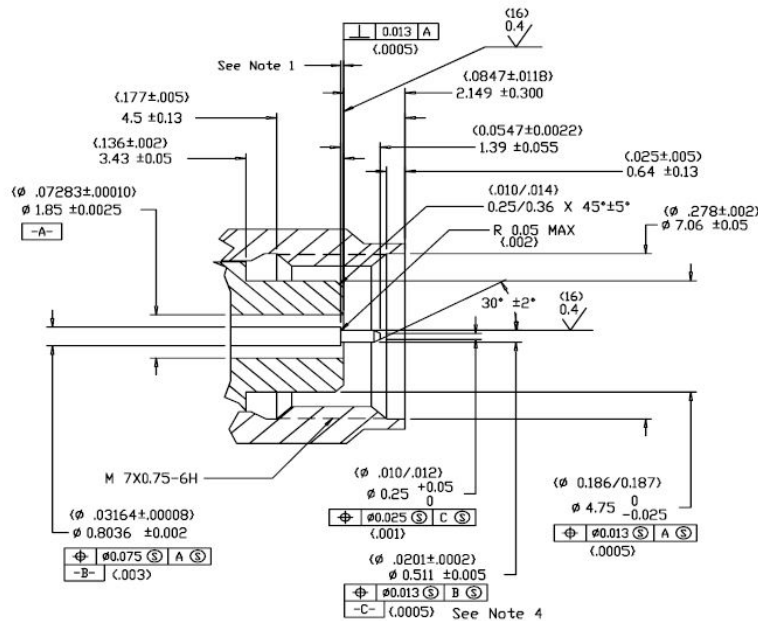


# Appendix A

## IEEE 287 Standard 1.85 mm Connector Drawings

This appendix represent a drawing for the 1.85 mm male connector defined by IEEE 287 Standard.

IEEE STANDARD FOR PRECISION COAXIAL CONNECTORS IEEE  
Std 287-2007



NOTE 1—Original design is in millimeters.

NOTE 2—All dimensions are shown in millimeters over inches shown in brackets.

NOTE 3—The pin depth specification is to be consistent with the electrical requirements of the device where the connector is to be used. The maximum allowable pin depth for the 1.85 mm LPC is 0.013 [0.0005].

NOTE 4—The wrench flat size for the 1.85 mm LPC is 8 mm with a maximum outer diameter of 9.24 [0.364].

NOTE 5—The recess length and diameter of the pin are critical to assure proper functioning and nondestructive mating with a 1.85 mm constant impedance contact.

NOTE 6—Provisions shall be permitted in the LPC and GPC connectors, which facilitate mating of the LPC center contact, such as the sliding of the coupling nut on the plug connector, provided that all the electrical and mechanical performance requirements are met.

Figure A.1: 1.85 mm pin LPC connector drawings according IEEE P287 standard.

# Appendix B

## Connector Photos

This appendix shows pictures of the tested connectors at different points of their test process taken with an optical microscope.

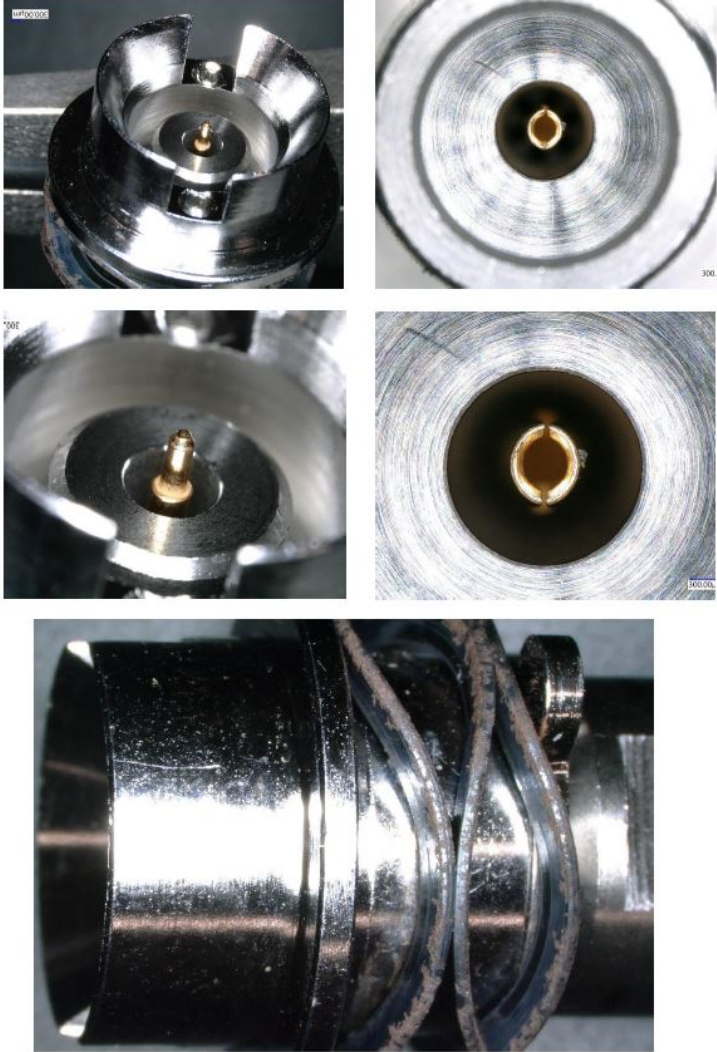


Figure B.1: Connector 12 housing appearance after an accelerated testing.

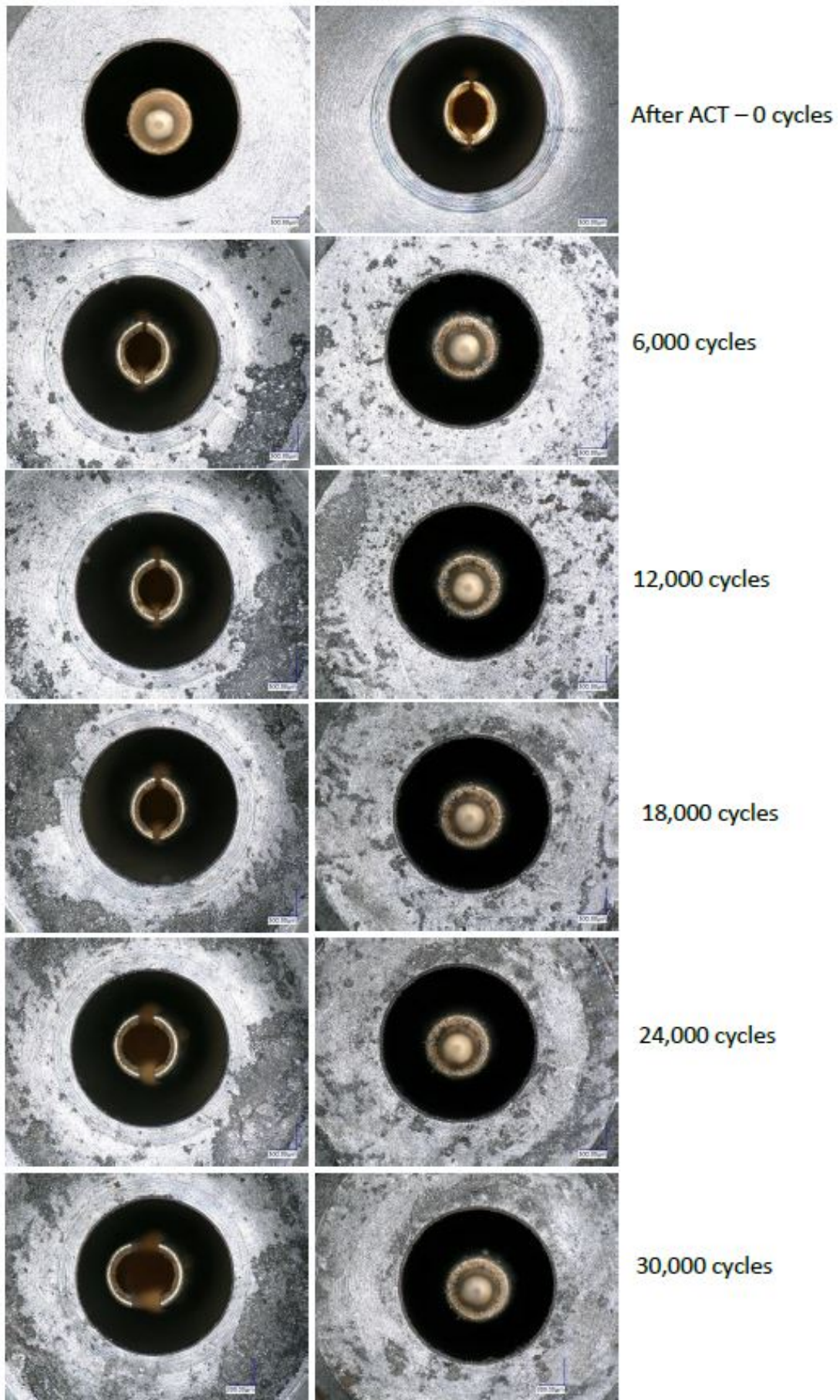


Figure B.2: Pictures of connector 12 appearance for different number of cycles.

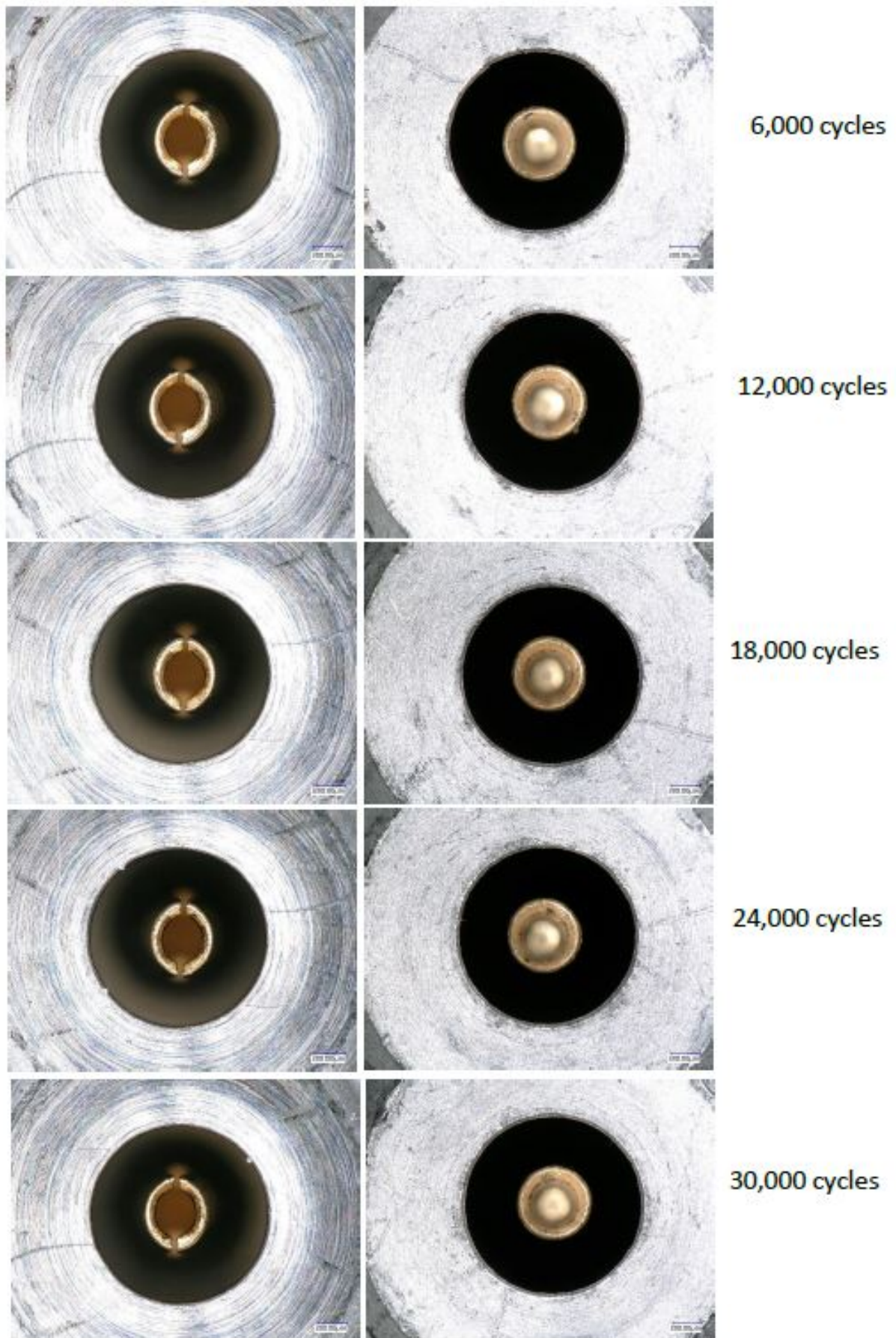


Figure B.3: Pictures of connector 13 appearance from 6,000 to 30,000 cycles.

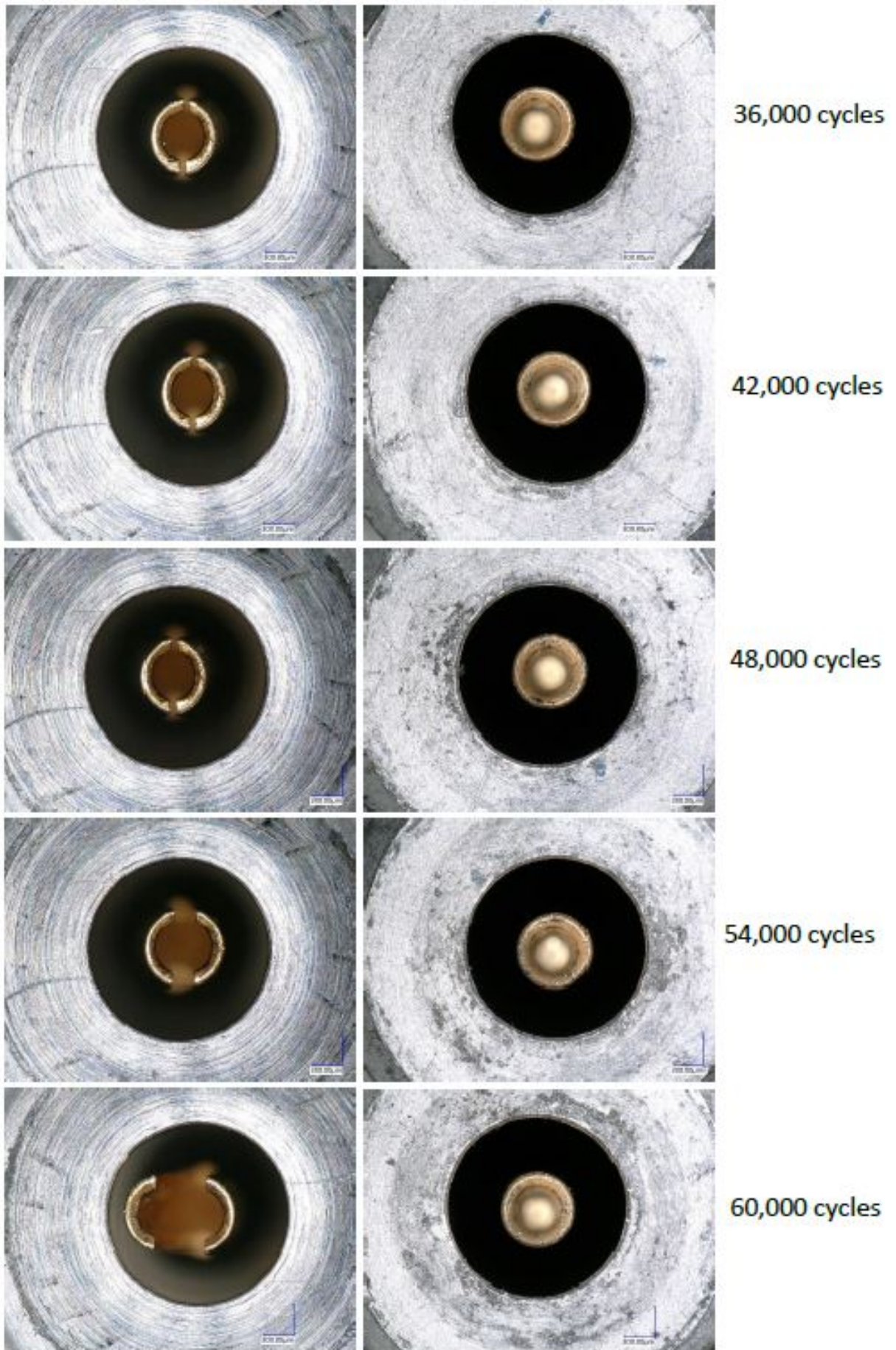


Figure B.4: Pictures of connector 13 appearance from 30,000 to 60,000 cycles.

# Appendix C

## Mechanical and Dimensional Measurements

This appendix presents the mechanical and dimensional measurements as part of the reliability test procedure for each of the 14 connectors.

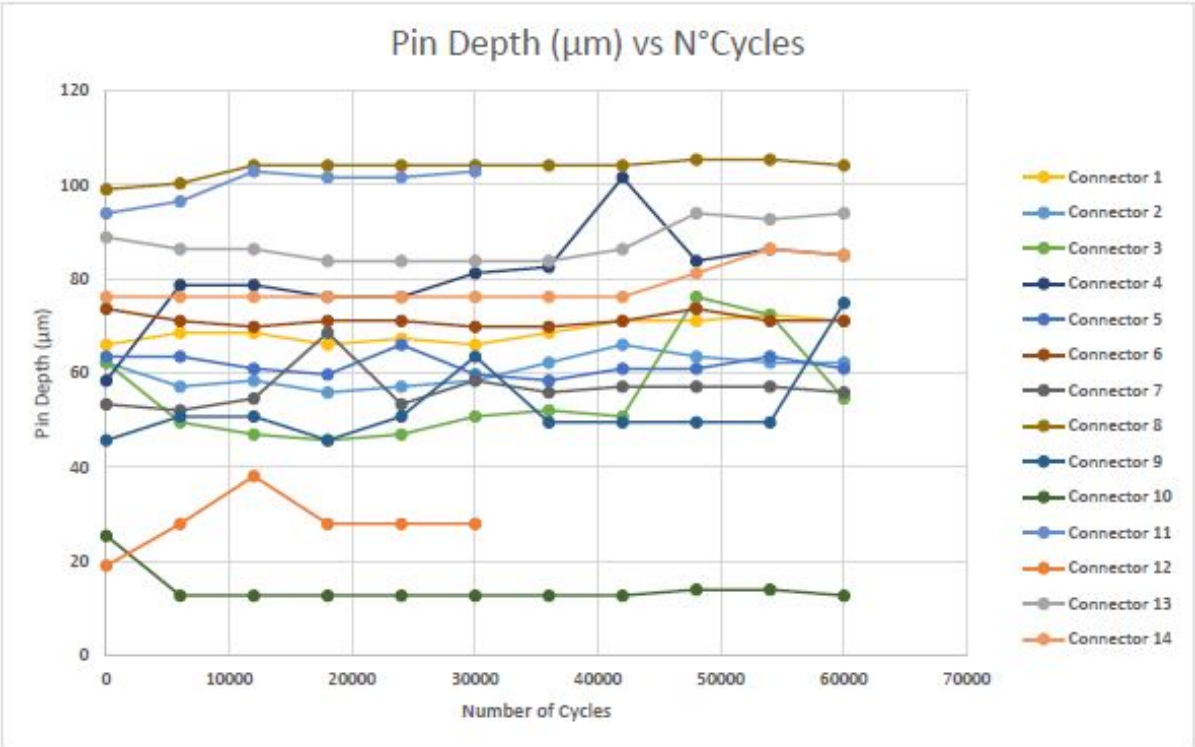


Figure C.1: Pin depth versus number of cycles for the 14 tested connectors.

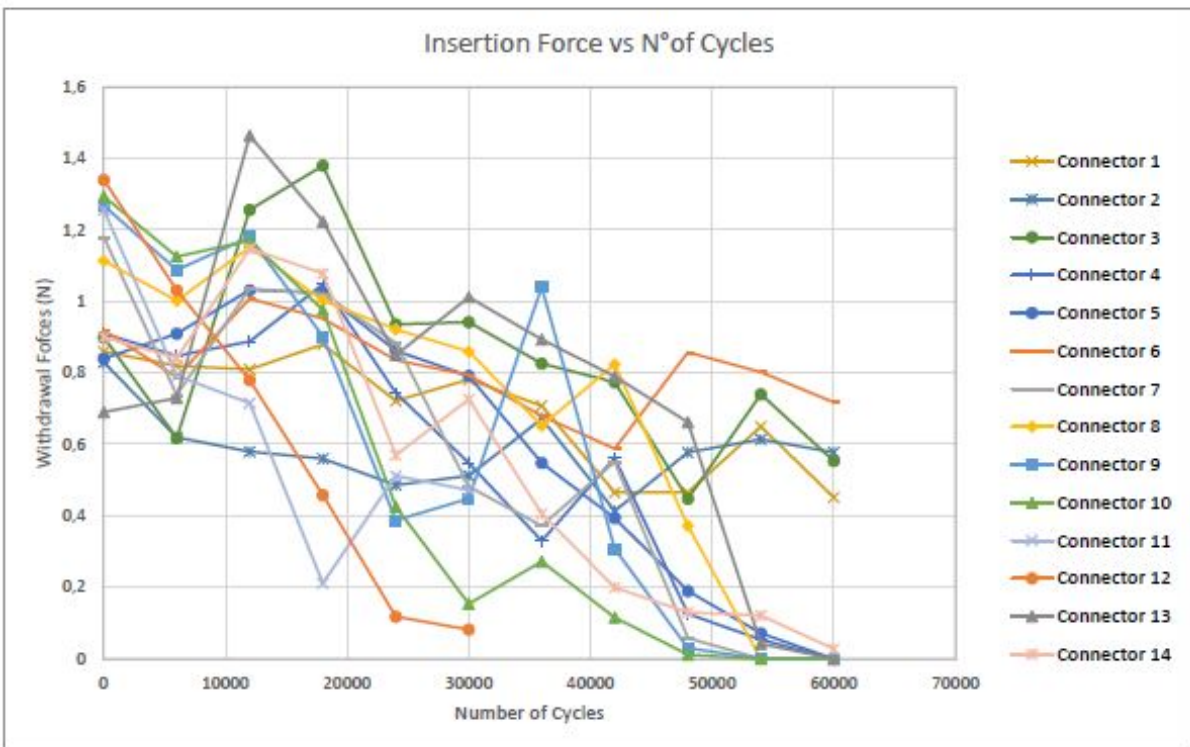
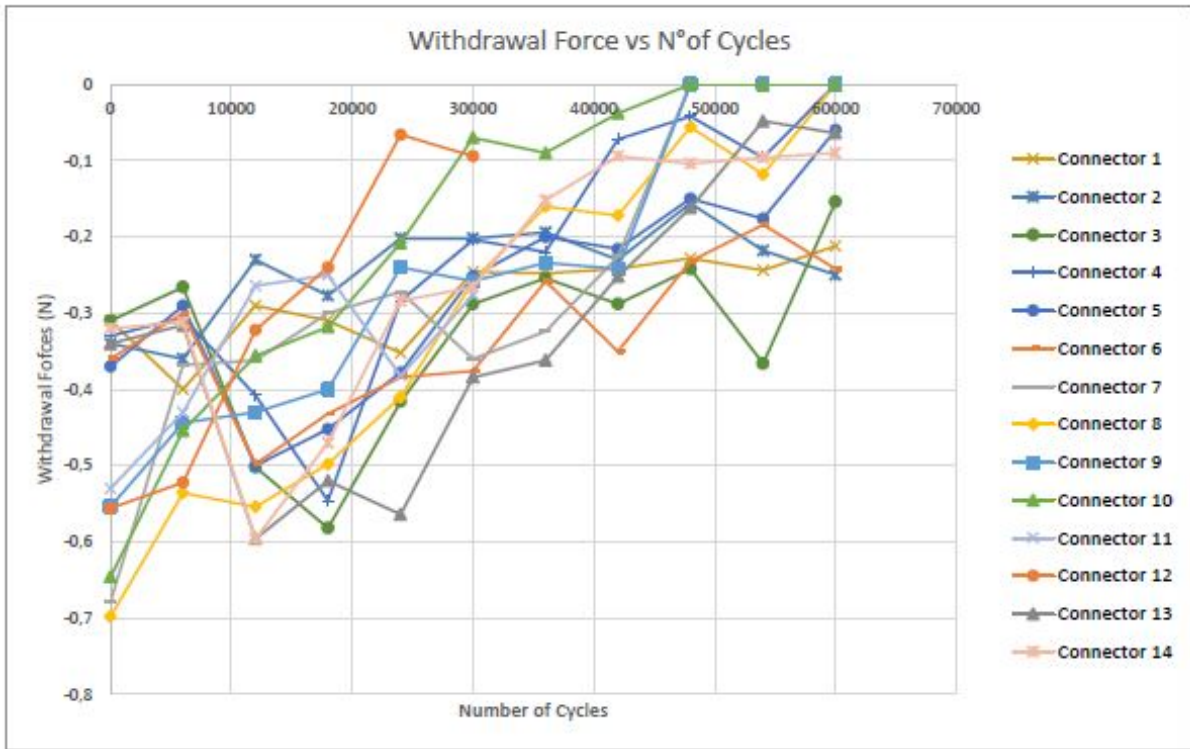


Figure C.2: Insertion and withdrawal forces versus number of cycles for the 14 tested connectors.

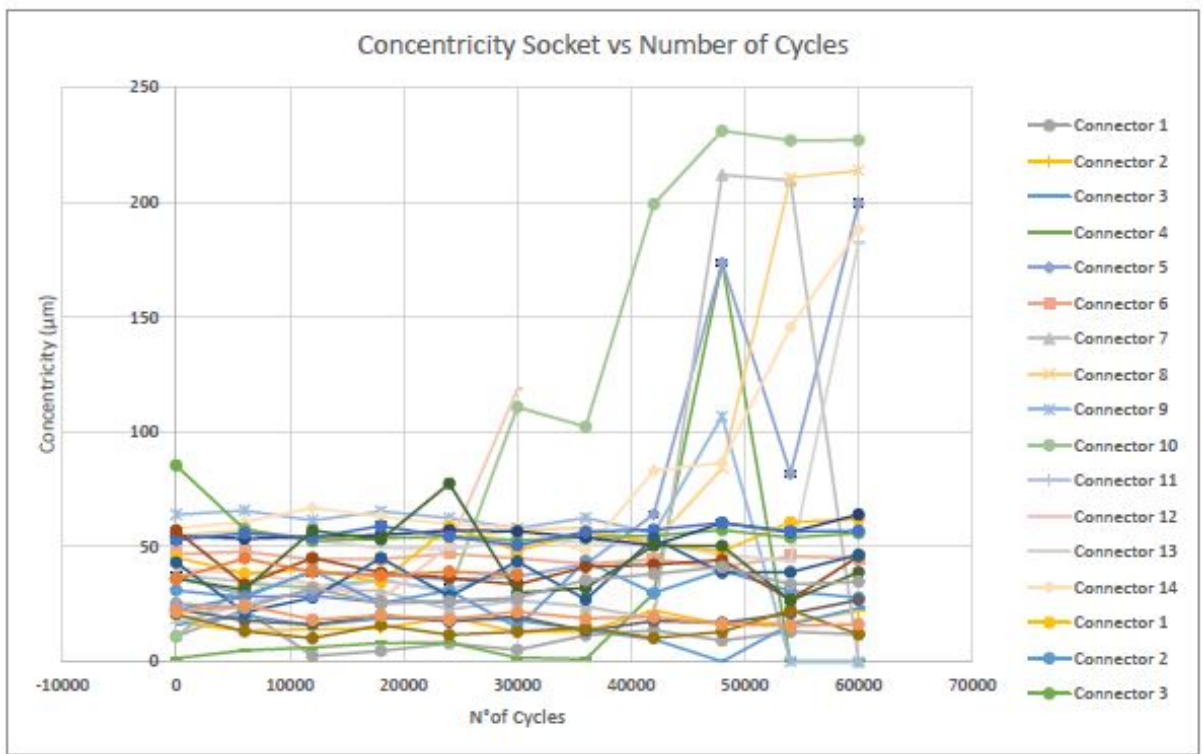
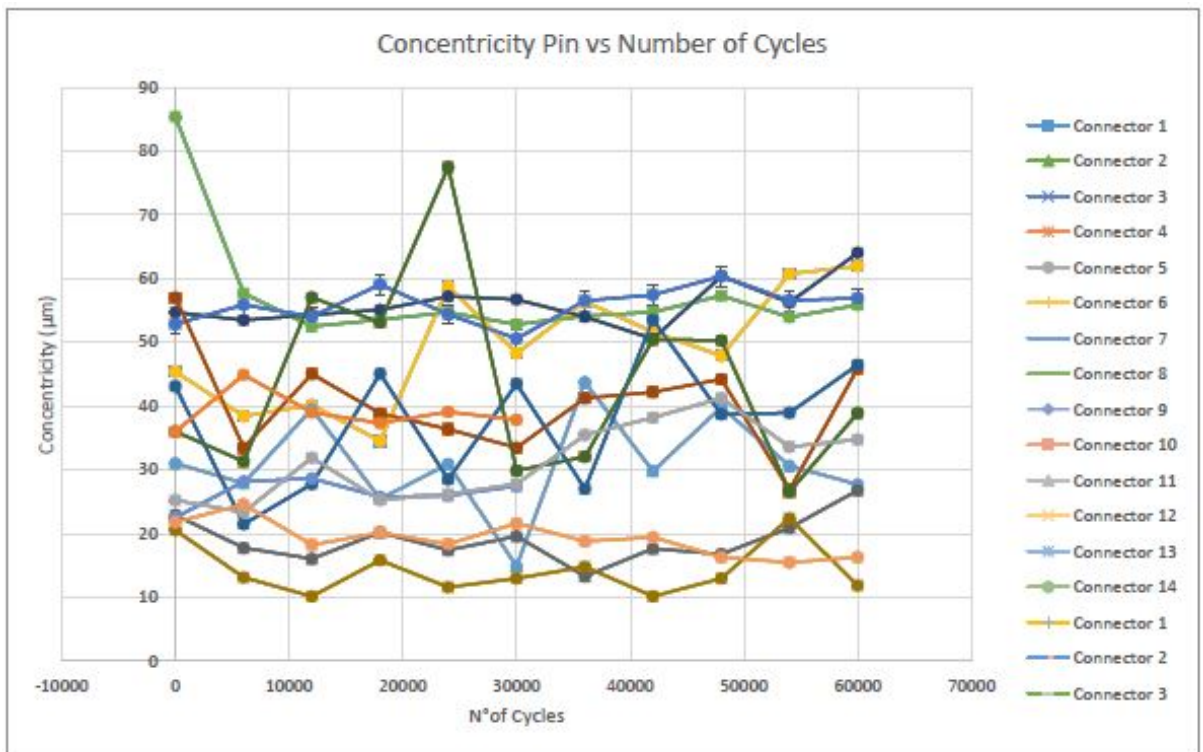


Figure C.3: Concentricity of the centre contacts versus number of cycles for the 14 tested connectors.



# Appendix D

## Measured S-Parameters

This section is divided in measured S-parameters during the 60,000 cycles testing (without calibration) and in measured S-parameters before and after the test to account for the performance. The performed S-parameters measurements are for the 12 first connectors.

### Performed Measurements During Testing - Reliability:

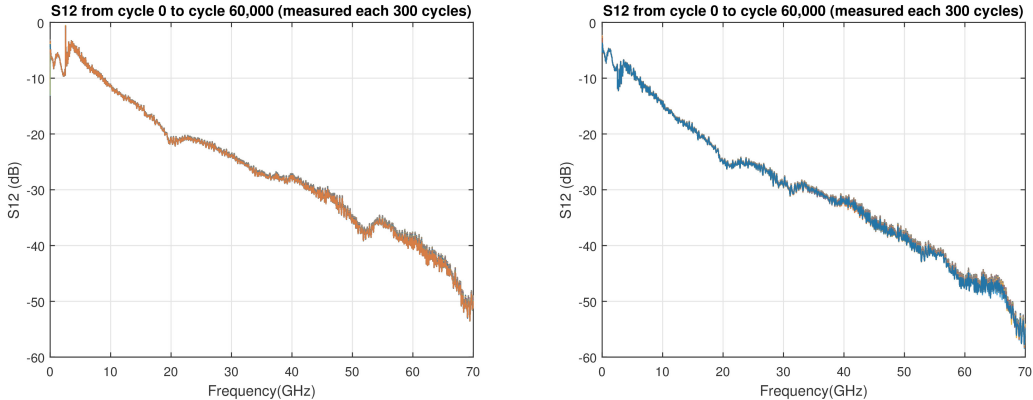


Figure D.1: Measured S12 of connector 1 on the left and measured S12 of connector 2 on the right.

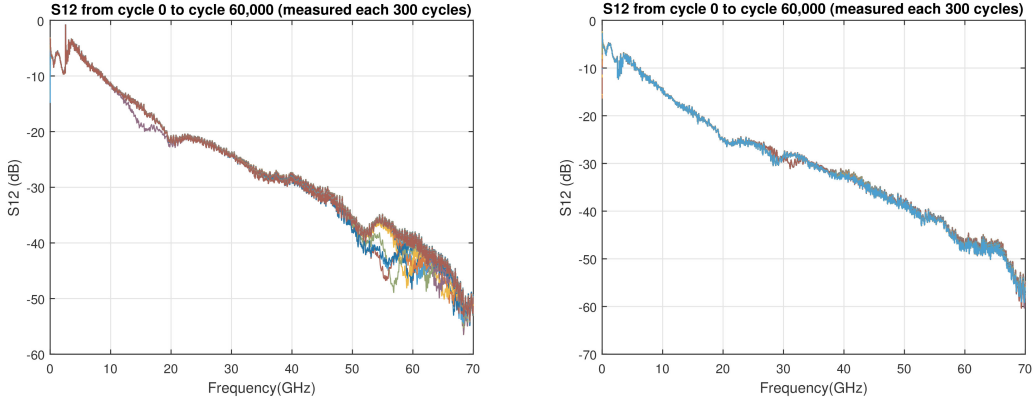


Figure D.2: Measured S12 of connector 3 on the left and measured S12 of connector 4 on the right.

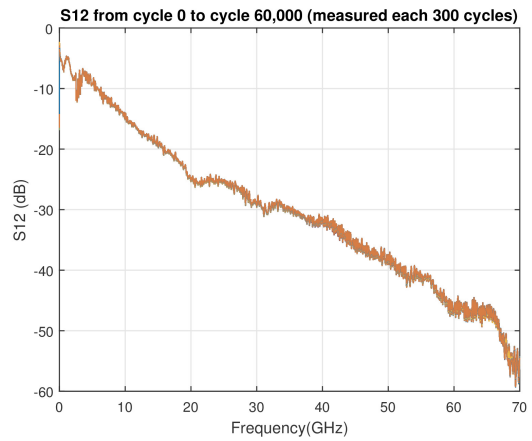
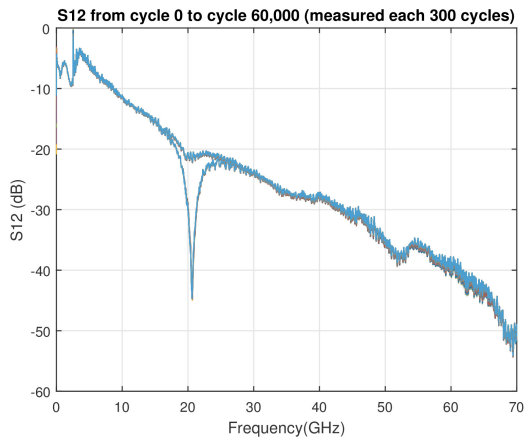


Figure D.3: Measured S12 of connector 5 on the left and measured S12 of connector 6 on the right.

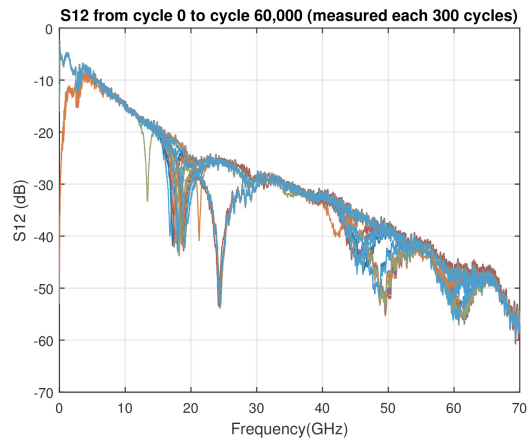
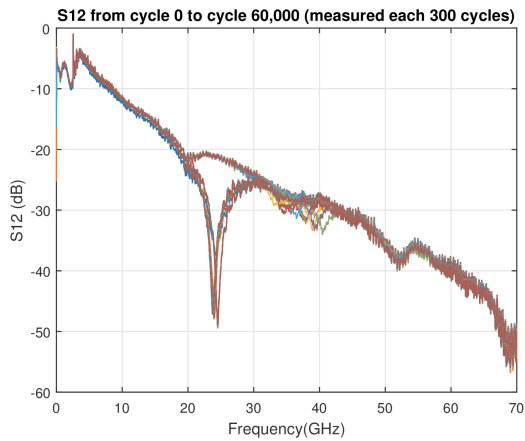


Figure D.4: Measured S12 of connector 7 on the left and measured S12 of connector 8 on the right.

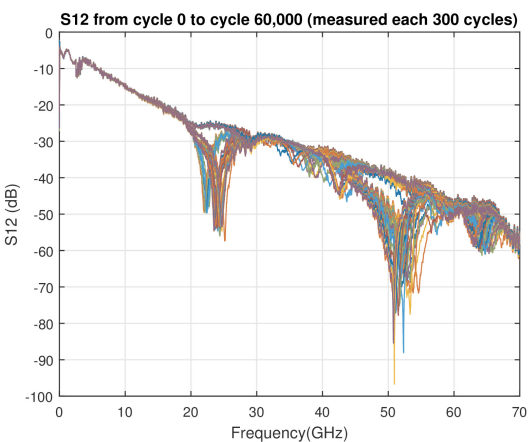
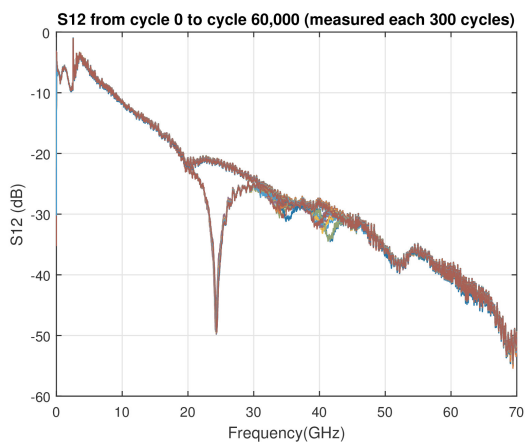


Figure D.5: Measured S12 of connector 9 on the left and measured S12 of connector 10 on the right.

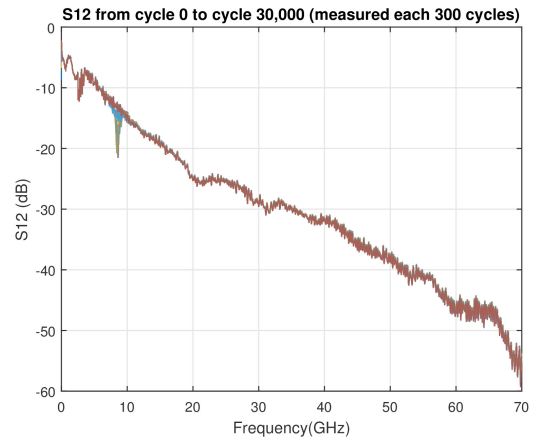
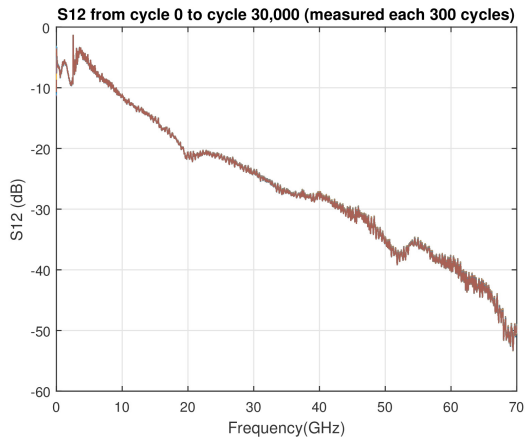


Figure D.6: Measured S12 of connector 11 on the left and measured S12 of connector 12 on the right.

**Performed Measurements before and after testing - Performance:**

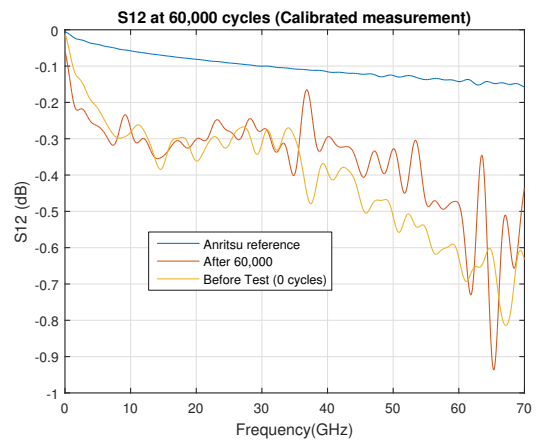
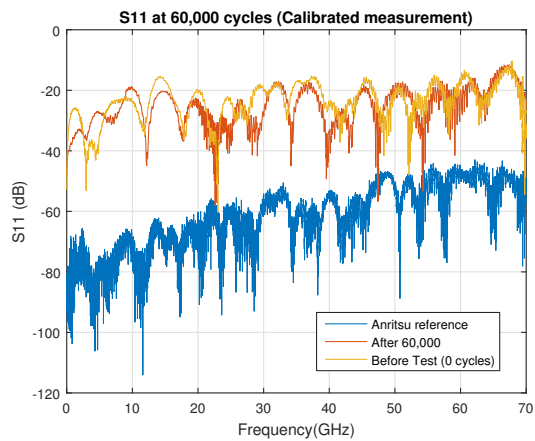


Figure D.7: Measured S11 (left) and S12 (right) after 60,000 cycles for connector 1.

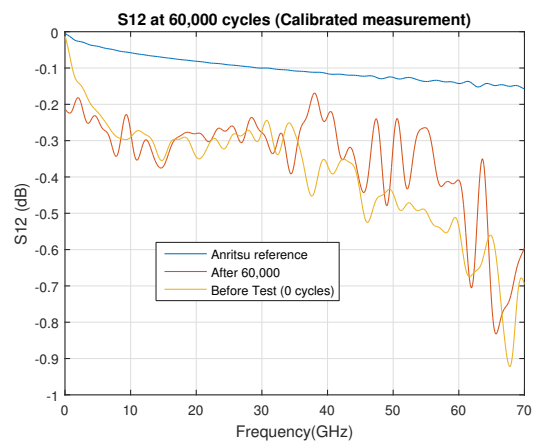
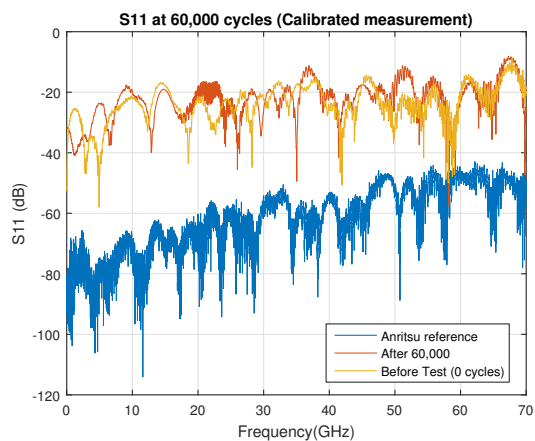


Figure D.8: Measured S11 (left) and S12 (right) after 60,000 cycles for connector 2.

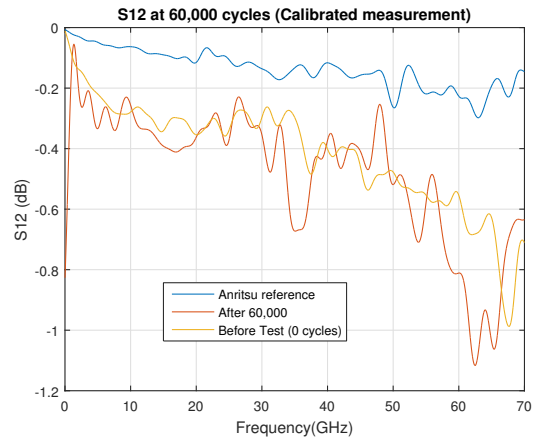
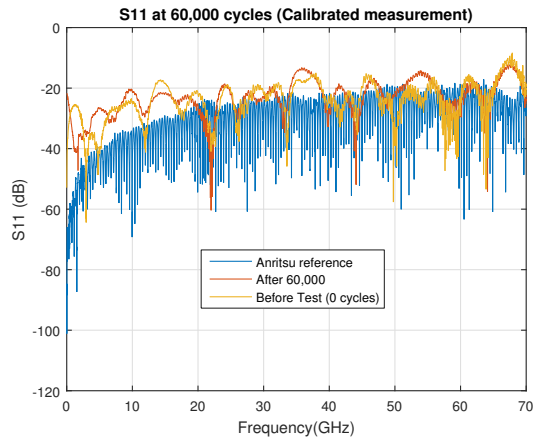


Figure D.9: Measured S11 (left) and S12 (right) after 60,000 cycles for connector 3.

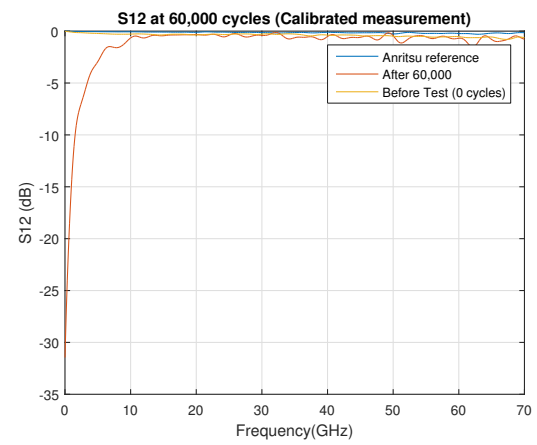
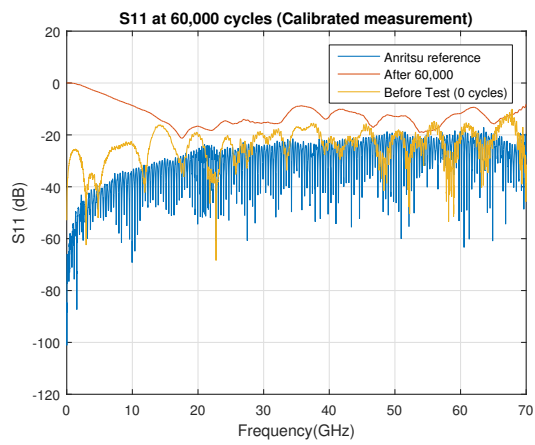


Figure D.10: Measured S11 (left) and S12 (right) after 60,000 cycles for connector 4.

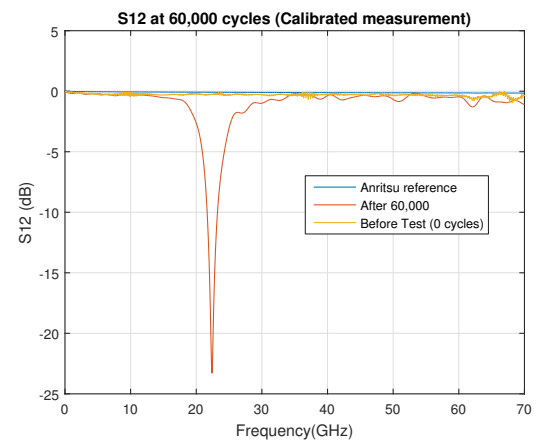
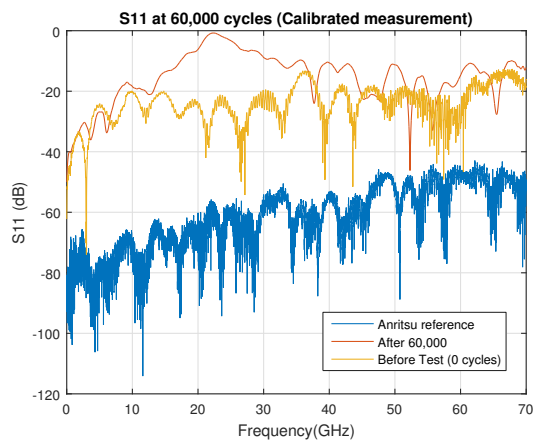


Figure D.11: Measured S11 (left) and S12 (right) after 60,000 cycles for connector 5.

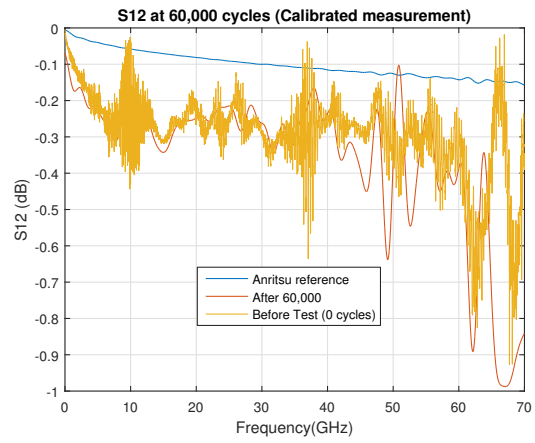
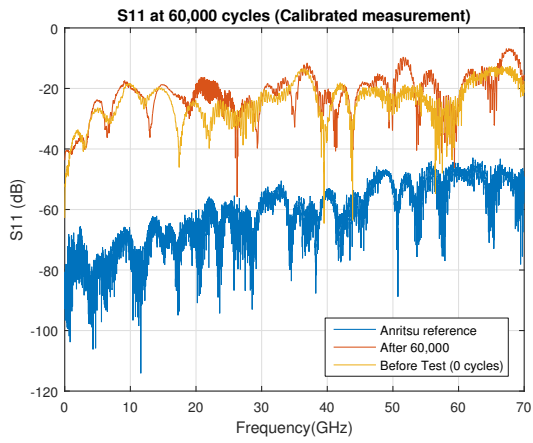


Figure D.12: Measured S11 (left) and S12 (right) after 60,000 cycles for connector 6.

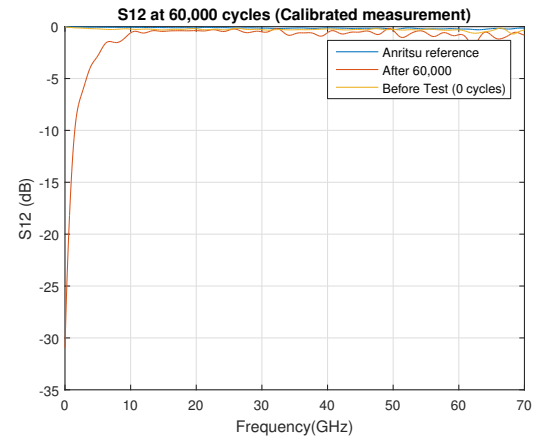
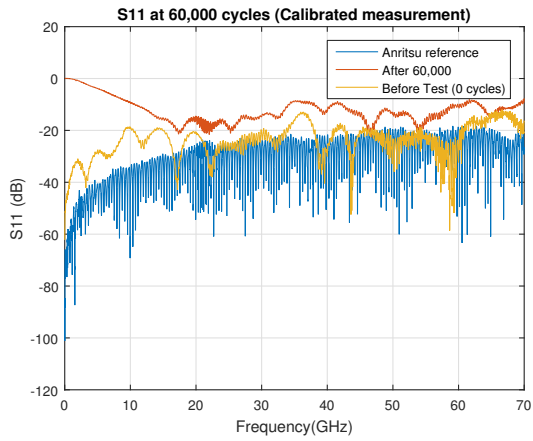


Figure D.13: Measured S11 (left) and S12 (right) after 60,000 cycles for connector 7.

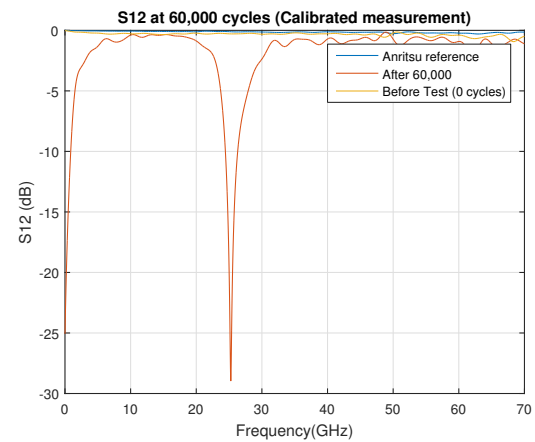
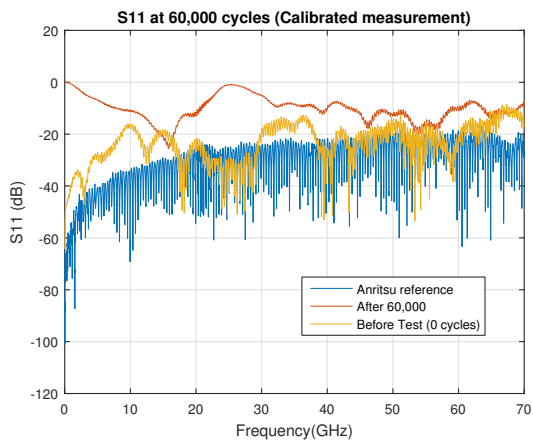


Figure D.14: Measured S11 (left) and S12 (right) after 60,000 cycles for connector 8.

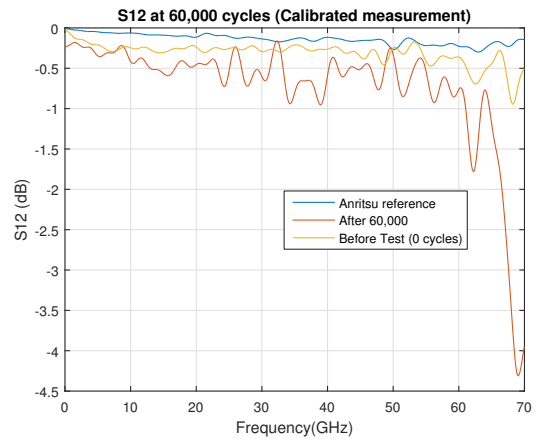
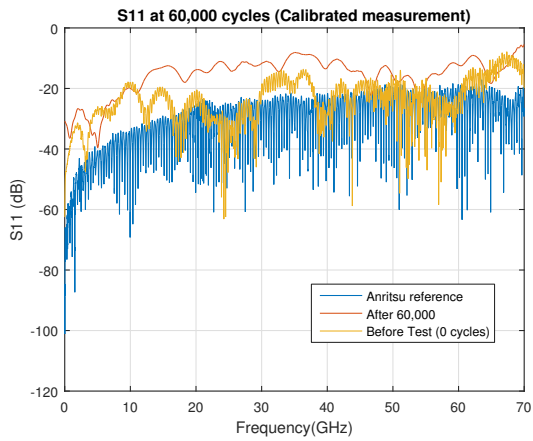


Figure D.15: Measured S11 (left) and S12 (right) after 60,000 cycles for connector 9.

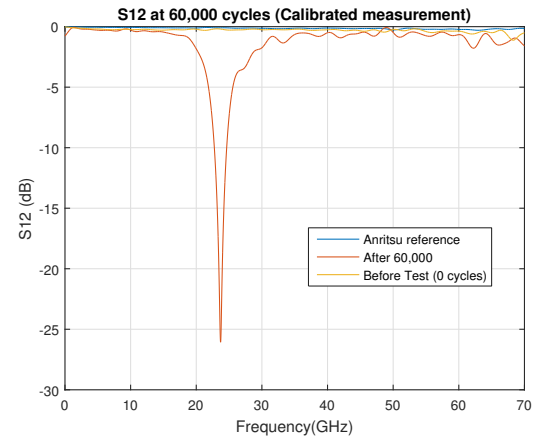
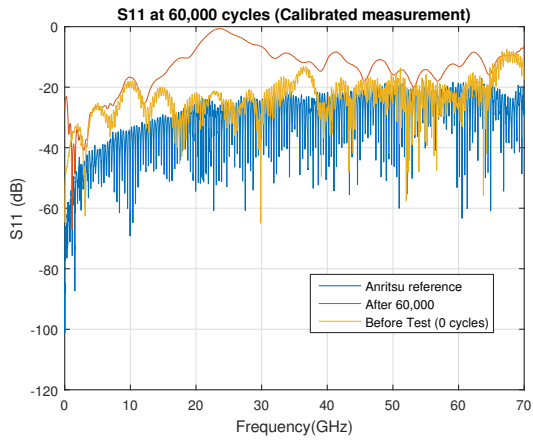


Figure D.16: Measured S11 (left) and S12 (right) after 60,000 cycles for connector 10.

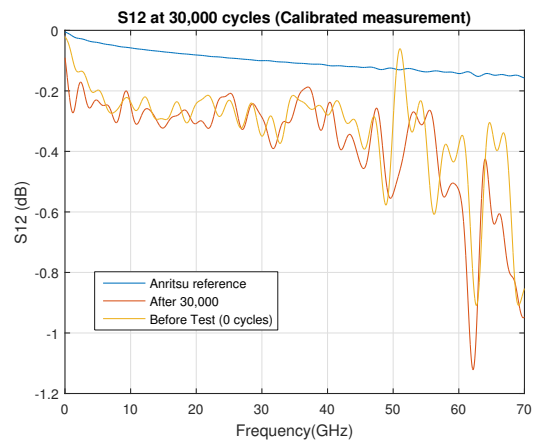
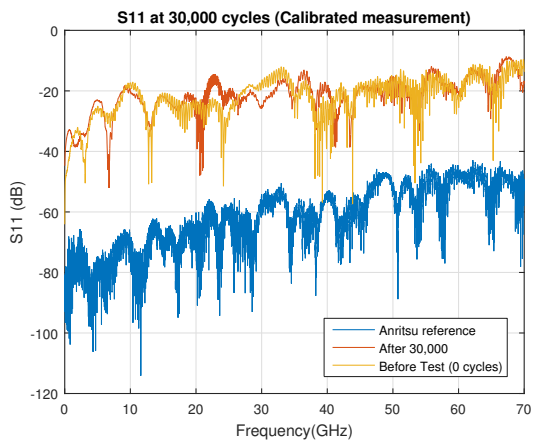


Figure D.17: Measured S11 (left) and S12 (right) after 30,000 cycles for connector 11.

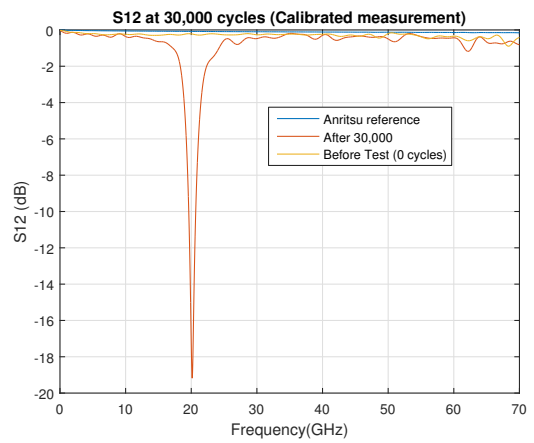
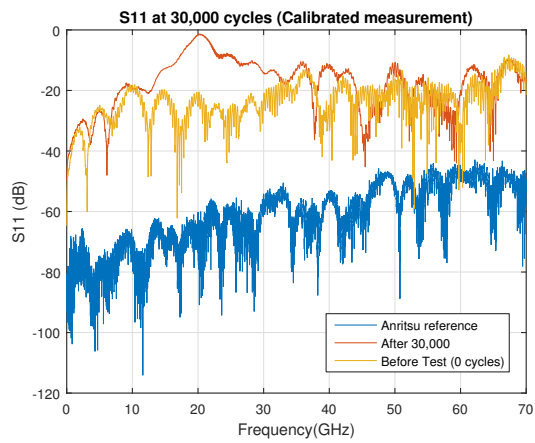


Figure D.18: Measured S11 (left) and S12 (right) after 30,000 cycles for connector 12.

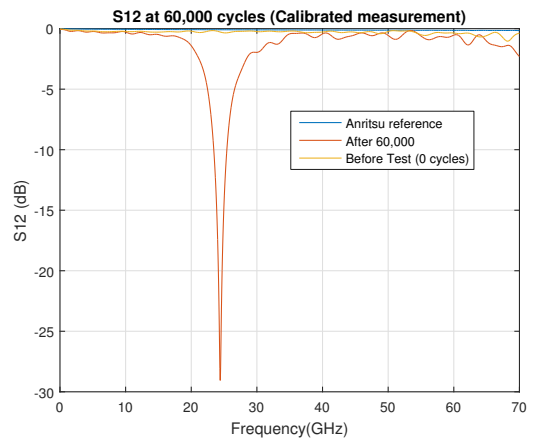
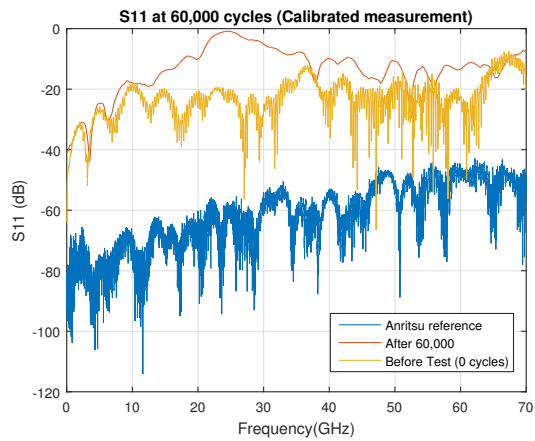


Figure D.19: Measured S11 (left) and S12 (right) after 60,000 cycles for connector 13.

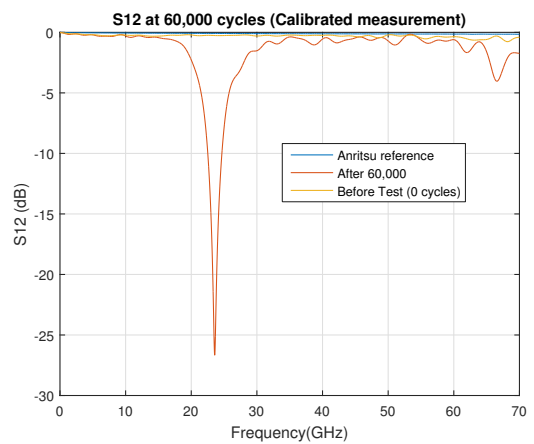
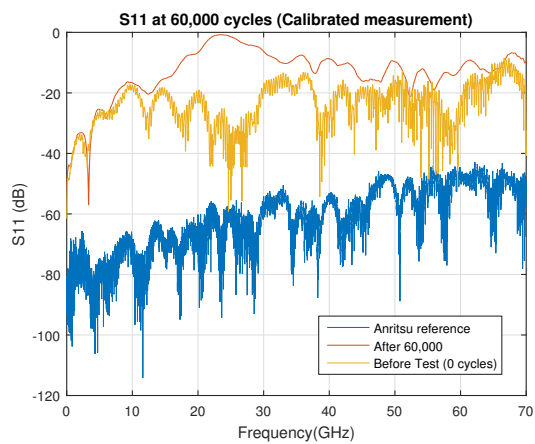


Figure D.20: Measured S11 (left) and S12 (right) after 60,000 cycles for connector 14.

Connector	Cycles to Failure	Resonance Frequency (GHz)	Notes
1	-	-	No failure, although: Insertion & withdrawal forces performed with non-valid insertion pins
2	-	-	No failure, although: Insertion & withdrawal forces performed with non-valid insertion pins
3	42,000	[13.5;16.5]	Failed while measuring insertion and withdrawal forces. No setup problems <sup>1</sup> .
4	30,000	[69;70]	Failed while measuring insertion and withdrawal forces. No setup problems.
5	48,000	[18.7;23]	Failed while measuring insertion and withdrawal forces. No setup problems.
6	54,000	[69.3;69.4]	Failed while measuring insertion and withdrawal forces. No setup problems.
7	45,900	[19;30]	Failed while measuring insertion and withdrawal forces. Setup problems between cycle 6,000 and cycle 18,000.
8	45,000	[0;2.5] & [20.5;30]	Failed while measuring insertion and withdrawal forces. Setup problems between cycle 6,000 and cycle 18,000.
9	36,000	[21;29.5]	Failed while measuring insertion and withdrawal forces. Setup problems between cycle 12,000 and cycle 42,000.
10	30,000	-	Failed while measuring insertion and withdrawal forces. Setup problems between cycle 12,000 and cycle 42,000.
11	-	-	No failure registered during the 30,000 cycles.
12	24,900	[8;9]	Only connector that failed in middle of cycle testing and not during insertion/withdrawal force measurements.
13	48,000	[20;30]	S-parameters were not measured during the cycle testing. Cycles to failure defined by concentricity and forces measurements. Failure resonance frequency obtained from the performance measurements.
14	36,000	[20;28.4]	S-parameters were not measured during the cycle testing. Cycles to failure defined by concentricity and forces measurements. Failure resonance frequency obtained from the performance measurements.

Table D.1: Summary of Connector Reliability testing results.

<sup>1</sup>Setup problems account for damaged cables (due to cable movement during each insertion), ATE system (problems with docking for high number of insertions) and other parts of the ATE system setup that get degraded or damaged with the increasing number of cycles.



# Appendix E

## Simulation Results

This appendix presents the stress and strain tensors obtained by the mechanical simulation. The figures shown are for the simulation under plastic conditions.

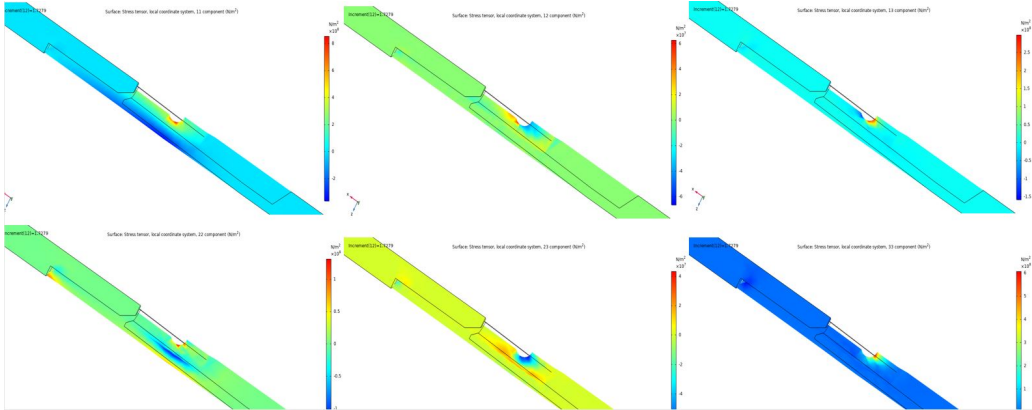


Figure E.1: Components of stress tensor obtained for a plastic simulation.

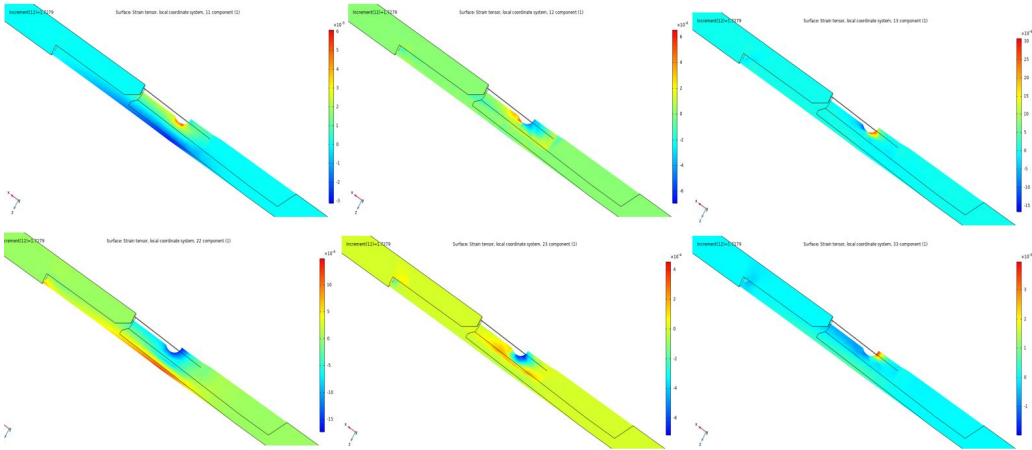


Figure E.2: Components of strain tensor obtained for a plastic simulation.

# Appendix F

## Characterization - Scanning Electron Microscope

In this appendix a characterization of other connectors are shown after the insertion test using the high resolution microscope (SEM). The different samples show an EDS analysis performed to pin and socket and an analysis of the fractured surface.

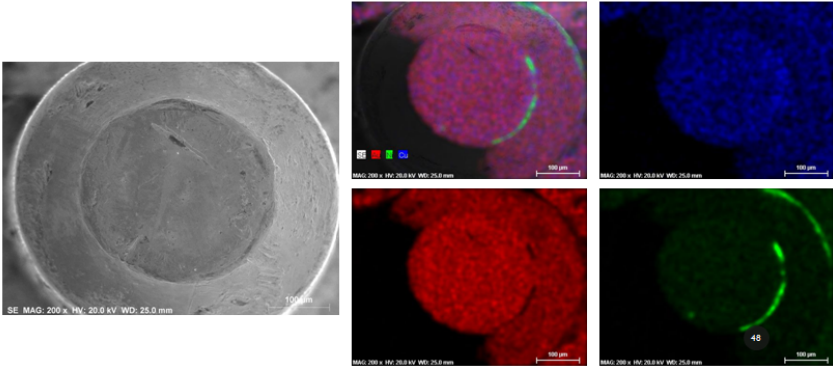


Figure F.1: Surface mapping analysis performed from a top view of connector 12.

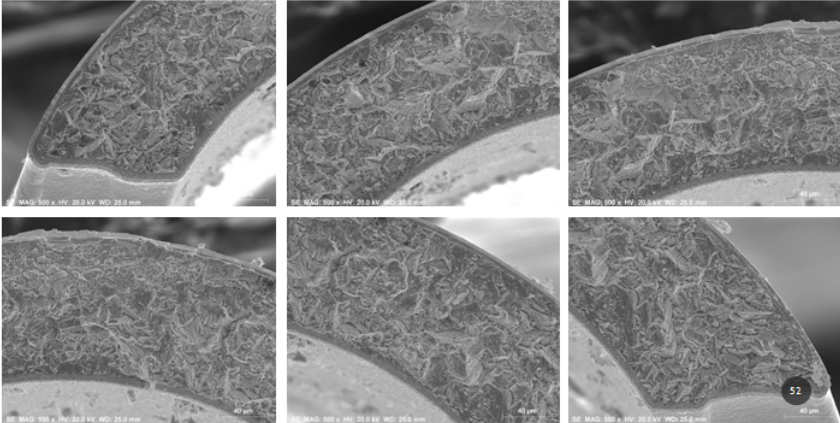


Figure F.2: Pictures of different areas of the socket fractured surface.